UNIVERSITÉ DE REIMS CHAMPAGNE-ARDENNE

THÈSE

présentée à l'U.F.R. des Sciences Exactes et Naturelles pour obtenir le titre de

Doctor
Europeus

DOCTEUR DE L' UNIVERSITÉ DE REIMS CHAMPAGNE-ARDENNE EN SCIENCES: SPÉCIALITÉ MÉCANIQUE ET MATÉRIAUX

par

Adele CARRADÓ

Sujet:

Contribution à la caractérisation des propriétés mécaniques et microstructurales des liaisons céramique-métal utilisées pour les applications des matériaux dentaires

Soutenue le 5 novembre 2001 devant le jury:

MM.	L. Barrallier	Maître de Conférences, ENSAM, Aix en Provence	
	Y. Delmas	Professeur, Université de Reims	
	C-H. de Novion	Professeur, LLB, CEA Saclay	
	J-L. Lataillade	Professeur, ENSAM, Bordeaux	
	A. Lodini	Professeur, Université de Reims	Codirecteur de thèse
	W. Reimers	Professeur, Université Berlin	Rapporteur
	F. Sacchetti	Professeur, Université Perugia, Italie	Rapporteur
	J-M. Sprauel	Professeur, Université Aix - Marseille II	Codirecteur de thèse

UNIVERSITÉ DE REIMS CHAMPAGNE-ARDENNE

THÈSE

présentée à l'U.F.R. des Sciences Exactes et Naturelles pour obtenir le titre de

Doctor
Europeus

DOCTEUR DE L' UNIVERSITÉ DE REIMS CHAMPAGNE-ARDENNE EN
SCIENCES: SPÉCIALITÉ MÉCANIQUE ET MATÉRIAUX

par

Adele CARRADÓ

Sujet:

Contribution to the characterisation of the mechanical and microstructural properties of metal-ceramic bounds used in dental applications

Soutenue le 5 novembre 2001 devant le jury:

MM.	L. Barrallier	Maître de Conférences, ENSAM, Aix en Provence	
	Y. Delmas	Professeur, Université de Reims	
	C-H. de Novion	Professeur, LLB, CEA Saclay	
	J-L. Lataillade	Professeur, ENSAM, Bordeaux	
	A. Lodini	Professeur, Université de Reims	Codirecteur de thèse
	W. Reimers	Professeur, Université Berlin	Rapporteur
	F. Sacchetti	Professeur, Université Perugia, Italie	Rapporteur
	J-M. Sprauel	Professeur, Université Aix - Marseille II	Codirecteur de thèse

Index

Sommaire

Remerciements

Le travail présenté dans ce mémoire a été effectué au laboratoire MécaSurf (E.N.S.A.M.) d'Aix en Provence et au laboratoire Léon Brillouin du CEA Saclay.

Je remercie chaleureusement Monsieur le Professeur Alain Lodini codirecteur de ma thèse pour l'autonomie qu'il m'a accordée et la confiance qu'il m'a témoignée.

Je tiens à exprimer ma reconnaissance particulière à Monsieur le Professeur Jean-Michel Sprauel qui a codirigé mes travaux de thèse et qui m'a constamment suivie au cours de ces trois années. Son expérience, ses conseils et sa compétence m'ont été précieux.

Je remercie sincèrement Monsieur le Professeur Francesco Sacchetti du Département de Physique de Université de Perugia (Italie) et Monsieur le Professeur Walter Reimers de la Technische Universität de Berlin (Allemagne) d'avoir accepté d'être rapporteurs du présent mémoire en un temps si court, malgré leur notoriété et leurs emplois du temps chargés.

Monsieur le Professeur Jean-Luc Lataillade, directeur du Laboratoire Matériaux Endommagement Fiabilité Ingénierie des Procédés de l'E.N.S.A.M. de Bordeaux, m'a honoré de sa présence en acceptant de présider au jury de cette thèse.

A Monsieur le Professeur Charles Henri de Novion, merci de m'avoir accueillie dans le laboratoire Léon Brillouin du CEA Saclay pour ma troisième année de thèse et d'avoir accepté de faire partie du jury.

Merci à Monsieur le Professeur Yves Delmas Directeur du Groupe de Mécanique, Matériaux et Structures de l'Université de Reims Champagne Ardenne pour sa présence au sein du jury.

Quelques petits mots de gratitude aux gens du laboratoire MécaSurf:

Je remercie tout particulièrement le Dr Laurent Barrallier, qui a fait parti du jury. Je tiens à lui exprimer toute ma reconnaissance et mon amitié pour son soutien, les précieux conseils qu'il m'a apportés et pour l'aide qu'il m'a fournie pendant la réalisation de mes expériences.

Au Dr Agnès Fabre pour son aide apportée pendant les mesures à l'ESRF, pour son soutien moral et sa grande disponibilité.

Mes remerciements vont aussi à Philippe Malard pour l'aide technique qu'il m'a fournie pour la réalisation de mes expériences au laboratoire MécaSurf et pour sa cordialité. Egalement merci à Monsieur le Professeur Gérard Barreau de m'avoir accueillie dans le laboratoire MécaSurf pour mes premières années de thèse, ainsi qu'à l'ensemble du personnel et thésards du laboratoire MécaSurf.

Je tiens aussi à adresser mes vifs remerciement à Monsieur le Professeur Marcello Colapietro (du Département de Chimie de l'Université “La Sapienza”, Rome), au Dr Marco Vittori, au Dr Amelia

Montone, à Monsieur Renzo Marazzi (INN-NUMA laboratoire, ENEA Casaccia, Rome) et Monsieur Carlo Veroli (ICMAT laboratoire CNR de Montelibretti, Rome) et le staff du laboratoire CIGA (Université de Camerino, Macerata), que j'ai rencontre lors de mon stage en la Magnifique et Eternelle Rome, pour leur gentillesse, leur disponibilité et l'accueil chaleureux qu'ils m'ont témoigné lors de mon stage.

J'adresse un grand merci à mes amies de "nouvelle et longue date" qui m'ont amicalement écoutée, soutenue et encouragée. Merci à mes conseillers et amis fidèles (l'ordre alphabétique par prénom est obligatoire!) : Alessandra Spettoli, Michele Marcantoni, Nathalie Ferrer, Polina Volovitch, Rita Cesari, Veronique Thiebaut et Vesna Stanic.

Merci à Eglantine Courtois et Laurence Durivault, pour l'aide qu'elles m'ont apportée pendant la thèse.

Merci aussi à tous les thésards et à l'ensemble du personnel du laboratoire Léon Brillouin, et tout particulièrement à Mademoiselle Christelle Abraham et à Mesdames Chantal Marais, Chantal Pomeau et Claude Rousse et à Monsieur Bernard Mailleret. J'adresse aussi un grand merci au Dr Robert Papoular pour ses précieux conseils et son soutien.

A mes collèges du LACM: Bruno Coffino et Renault Mignolet pour leur précieuse aide et grande gentillesse lors de mes cours à l'Université de Reims.

Au Dr Pierre Millet du LACM pour m'avoir fourni les échantillons et la documentation sur les prothèses dentaires.

Cette thèse est dédiée à mes parents "Mamma Gabriella e Babbo Quirico" avec leur extraordinaire amour et leur incroyable patience m'ont permis d'obtenir tout ce que j'ai ...et à Emmanuel ...

Adele Carradò

INTRODUCTION

Glassy-ceramic coatings are used on metallic substrates in a variety of dental applications. One form of crystal found in dental ceramic is leucite ($KAlSi_2O_6$), Potassium Aluminium Silicate. A bulk of leucite is relatively weak and brittle compared to common implant metals (e.g. palladium, platinum, and silver alloys). In the coating, the mechanical properties of the ceramic are however greatly improved by coupling them with the ductile base metals. Nevertheless, these require a strong bounding of the leucite to the implant metal and they are a good way to link the mechanical properties of the metal with the good biological ones of the leucite.

The utility of dental porcelain, as a restorative, can be extended in the Porcelain-Fused to Metal (PFM) technique, as a strengthening mechanism for porcelain**.** Several layers of dental porcelain are fused to a metal casting. The coefficient of thermal expansion of these porcelains must be suitably matched with that of the alloy. The melting range of the alloy must be raised sufficiently above the fusion temperature of the porcelain for a successful operation. However the residual stresses can be present in both materials as they depend principally on the thermal treatments imposed to the materials and they may have a very strong influence on the mechanical behaviour in the sample and in particularly at the metal/ceramic interface.

For this reason, we performed classical X-ray, neutron diffraction and high-energy synchrotron measurements on the sample to evaluate the state of residual stress. These techniques are widely used and they are very powerful tools to this end, allowing the precise evaluation of residual stresses in the bulk and at interface of the materials in a non-destructive way. By this technique, the strain in the crystal lattice was measured, and the residual stress was calculated, assuming a linear elastic distortion of the crystal lattice.

Each one of these has been performed in different zones in the sample. For instance, we have used neutron diffraction to analyse both the glassy ceramic surface and the bulk of the leucite and of the palladium alloy, high-energy synchrotron radiation for the metal/ceramic interfaces. In this way, they have allowed to obtain the best information in different regions of the analysed sample.

The principal aim of this work consist in the evaluation of residual stress in a Porcelain-Fused to Metal (PFM) casted onto a palladium alloy substrate by different techniques which offer great interest in dental applications. It is also to improve the experimental techniques that normally are applied for the determination of residual stresses. This leads careful evaluation of experimental data obtained in zones which are very difficult to analyse owing to physical phenomena (absorption for high-energy synchrotron measurements and dispersion of wavelength for neutron diffraction) and geometrical problems.

We have introduced an innovative approach to solve these problems. A new Monte Carlo simulation program has been developed for that purpose to modelise any synchrotron radiation spectrometer. In addition, we have used an existing neutron spectrometer program [i].

In parallel to methodological problems, we have realised some measures to characterise the microscopic state of the sample. This study has allowed obtaining some structural information, which were useful for the mechanical approach.

More in detail, we present the thesis structure:

Chapter 1: A general view of material for dentistry application will be presented. To know chemical, physical and mechanical proprieties of constituents allow giving a great help for the evaluation of the residual stresses. Normally ceramic materials exhibit lower thermal expansion that metals. If ceramics on metallic substrates are produced at high temperatures, stresses could be generated by the thermal expansion difference between the two components, resulting in a deflection or fracture. A brief review of the chemical and physical characteristics of glassy ceramic and of noble casting used in odonthoiatric industry is presented.

Chapter 2: In dental applications, the stresses applied to the interface between the coating and the substrate could be high. This leads to the unbinding of the ceramic, due to the fracture of the first layers of the base metal. The mechanical properties of these metallic layers greatly depend on the residual stresses induced by the manufacturing of the coating. It is therefore very important to characterise these stresses. Some general aspects of evaluation of residual stresses and mechanical applied model during this study and a quick theoretical calculus will be reported.

---

[i] Thesis of Eric Pluyette, contribution de la diffraction neutronique a l'evaluation des contraintes residuelles au voisinage d'interface, Univ. Reims Champagne Ardenne, N°D'ORDRE: 97-Reims-011.

Chapter 3: It is well known that the results obtained by neutron diffraction show that to analyse near surface measurements (or data obtained at the metal/ceramic interface) it has to be accounted for some optical aberrations related to the instrumentation. In fact, reliable results cannot be obtained by usual experimental procedures, because the neutron probe is not completely immersed in the analysed sample. Therefore, it is important to correct the parasitic peak shifts which appear in these cases and which are not linked to the stress state of the scanned volume. This effect can be much greater than the peak shifts induced by the stresses. To solve this problem a complete modelling of 2-axis spectrometers, based on Monte Carlo calculations, has been developed either for neutrons or for synchrotron radiation. It accounts for the whole elements of the neutron or synchrotron instrument: the guide, the monochromator (if necessary), the primary and secondary slits and the sample. It allows also to optimise the experimental conditions and to define precisely the true volume of the neutron gauge.

Chapter 4: During three months of the stage in “La Sapienza” University of Rome (Italy), the composition and the structure of leucite dental glassy ceramic and palladium substrate have been determined. It has required the use of several "surface and in core" techniques. Glassy ceramic coating and metallic substrate microstructure were investigated using X-ray diffraction, Scanning Electron Microscopy and Energy Dispersive Spectroscopy. Transmission Electron Microscope technique was employed in order to study the structural properties of the Palladium alloy and the interface metal/ceramic by plane and cross section techniques respectively.

Chapter 5: To evaluate the mechanical behaviour of the sample at the metal/ceramic interface different non-destructive analysis of the residual stresses in leucite coating and palladium alloy substrate have been performed.

Classical X-ray diffraction and chemical etching X-ray diffraction measurements were carried out to evaluate respectively the stress state at the surface of the Palladium substrate just before the manufacturing of the coating and ceramic coating and in-depth profile stress defining a reference for synchrotron radiation measurements. Neutron diffraction measurements were carried out to obtain internal (in the bulk) and through-surface residual strain data from which the in-depth residual stress profiles have been derived for both the palladium substrate and the glass-ceramic coating. High-energy synchrotron measurements have been necessary for the analysis of the superficial layers of the substrate (the first 80 µm) and of course, the bulk of the coating and at the metal/ceramic interfaces zone.

Neutron and synchrotron diffraction results have shown that, to analyse near surface measurements and data at the metal/ceramic interface, it is necessary to account for some optical aberrations bound to the instrumentation for the neutron measurements and the very strong absorption phenomena for the synchrotron radiation experiments.

INTRODUCTION

Les revêtements vitrocéramique sont utilisés sur les substrats métalliques dans nombre d’applications dentaires. Une forme de cristal constituant les céramiques dentaires est la leucite ($KAlSi_2O_6$), un aluminosilicate de potassium.

Un massif de leucite est relativement faible et fragile comparé aux communs implants métalliques (e. g. les alliages de palladium, platine et argent). Dans le dépôt, les propriétés mécaniques de la céramique sont faites pour améliorer le couplage avec la base ductile des métaux. Cependant, une très forte liaison entre la leucite et l’implant métallique est requise et cela permet une bonne adaptation pour lier les propriétés mécaniques du métal et la bio-compatibilité de la leucite.

L’utilité des porcelaines dentaires (pour les méthodes de reconstruction) peut être étendue à la technique de la Porcelaine Fondue sur le Métal (PFM), en tant que mécanisme pour améliorer la résistance de la porcelaine. Plusieurs couches de porcelaine dentaire ont été fondues sur un métal mis en œuvre par moulage. Le coefficient de dilatation thermique de ces porcelaines doit être très proche de celui de l’alliage. L’intervalle de fusion de l’alliage de palladium doit être supérieur à la température de fusion de la porcelaine pour que le procédé soit efficace. Cependant, des contraintes résiduelles peuvent être présentes dans les deux matériaux. Elles dépendent principalement des traitements thermiques imposés aux matériaux et elles peuvent avoir une très forte influence sur le comportement mécanique de l'échantillon et en particulier sur la tenue en service de l'interface céramique/métal.

Pour ces raisons, afin d’évaluer l’état des contraintes résiduelles dans l’échantillon, nous avons effectué des mesures par diffraction des neutrons et des rayons X classiques et en utilisant un rayonnement synchrotron à haute énergie. Ces techniques, largement employées, sont très performantes. Elles permettent une évaluation précise et non-destructive des contraintes résiduelles dans le massif et aux interfaces des matériaux. Elles sont fondées sur la mesure des déformations du réseau cristallin, les contraintes résiduelles étant déduites des données expérimentales en appliquant les lois de l'élasticité linéaire.

Les techniques utilisées se sont avérées complémentaires car elles permettent d'analyser différentes zones de l'échantillon. Par exemple nous avons employé la diffraction des neutrons pour étudier à la fois les couches superficielles de la vitro – céramique, et les couches internes de la leucite et du substrat de palladium. Le rayonnement synchrotron à haute énergie a permis de caractériser l'interface céramique/métal. De cette façon nous avons obtenu les meilleures informations dans les différentes régions de l'échantillon analysé.

Le principal objectif de ce travail a donc consisté à évaluer les contraintes résiduelles dans un revêtement réalisé, par la technique PFM, sur un substrat d'alliage de palladium élaboré par moulage. Nous avons ainsi dû améliorer les techniques expérimentales utilisées pour la détermination des contraintes résiduelles. Ceci a nécessité un dépouillement soigné et précis des données expérimentales. Ce dépouillement a dû prendre en compte les *phénomènes physiques* (l'absorption pour les mesures par synchrotron à haute-énergie et la dispersion de longueur d'onde par la diffraction neutronique) intervenant dans la mesure et les *aberrations géométriques* inhérentes à chacune des techniques utilisées.

Nous avons donc mis au point une approche innovatrice pour résoudre ces problèmes. Un programme de simulation de type Monte Carlo à été développé dans ce but pour modéliser les installations utilisant le rayonnement synchrotron. Pour ce qui est des spectromètres de neutrons, nous avons réutilisé un programme existant [i].

Parallèlement aux problèmes méthodologiques, nous avons caractérisé l'état micro structural de l'échantillon. Cette étude nous a permis d'obtenir des informations qui ont été très utiles pour l'approche mécanique.

Nous allons détailler la structure de la thèse :

***Chapitre 1**:* Une vue générale des matériaux pour applications dentaires sera présentée. Comprendre les propriétés chimiques, physiques et mécaniques des constituants est d'une grande aide à évaluer les contraintes résiduelles. En général, les matériaux céramiques possèdent un coefficient de dilatation inférieur à celui des métaux. Les céramiques déposées sur les substrats métalliques sont élaborées à des températures élevées. Des contraintes peuvent dont être induites par cette incompatibilité thermique qui engendre des flexions et des ruptures des prothèses. Un bref aperçu des caractéristiques chimiques et physiques des vitrocéramiques et des alliages nobles utilisés en odontologie sera également présenté.

---

[i] Thèse de Eric Pluyette, Contribution de la diffraction neutronique a l'évaluation des contraintes résiduelles au voisinage d'interface, Univ. Reims Champagne Ardenne, N°D'ORDRE: 97-Reims-011.

Chapitre 2 : Dans les applications dentaires, les contraintes appliquées aux interfaces entre le dépôt et le substrat peuvent être élevées. Cela conduit à la rupture de la céramique par manque de liaison avec les premières couches du métal de base.

Les propriétés mécaniques de ces couches métalliques dépendent fortement des contraintes résiduelles induites par la fabrication du dépôt. Il est alors très important de caractériser ces contraintes. Les principes généraux des méthodes d'évaluation des contraintes résiduelles seront donc abordés dans ce chapitre. Nous y présenterons également un modèle micro-mécanique qui nous a permis d'estimer les caractéristiques élastiques et thermiques de la céramique. Un modèle théorique simple sera également mis en œuvre pour prédire les contraintes résiduelles induites par les incompatibilités thermiques.

Chapitre 3 : Il est bien connu que les résultats obtenus par diffraction neutronique montrent que l'analyse des mesures proches de la surface (ou les données obtenues aux interfaces céramiques / métal) ne tiennent pas compte, en général, des aberrations optiques relatives à l'instrumentation. En effet, des résultats fiables ne peuvent être obtenus par les procédures classiques expérimentales, car le volume de sonde neutronique n'est pas complètement immergé dans l'échantillon analysé. Il est alors important de corriger le décalage parasite du pic qui apparaît dans ce cas et qui n'est pas lié à l'état mécanique du volume balayé. Cet effet peut être plus grand que le décalage du pic induit par les contraintes. Pour résoudre ce problème, nous avons développé une modélisation complète des spectromètres deux-axes, basée sur une simulation Monte Carlo, valable aussi bien pour les neutrons, que pour le rayonnement synchrotron. Cette simulation prend en compte l'ensemble des éléments de l'instrument (neutrons ou synchrotron): le guide, le monochromateur (si nécessaire), les fentes primaires et secondaires et l'échantillon. Elle permet ainsi d'optimiser les conditions expérimentales et de définir précisément la taille et la position du volume sonde.

Chapitre 4 : Au cours des trois mois de stage effectués à l'Université "La Sapienza" de Rome (Italie), nous avons déterminé la composition et la structure de la vitro céramique dentaire à base de leucite et du substrat d'alliage de palladium. Nous avons ainsi utilisé plusieurs techniques de surface et de volume. Les microstructures du dépôt céramique vitreux et du substrat métallique ont été examinées par diffraction des rayons X, par Microscopie Electronique à Balayage et Spectroscopie à Dispersion d'Energie. Pour étudier les propriétés structurales de l'alliage de palladium et l'interface métal /céramique, nous avons également employé la Microscopie Electronique à Transmission.

Chapitre 5 : Afin de caractériser le comportement mécanique de l'échantillon aux interfaces céramique-métal nous avons réalisé différentes analyses non-destructive des contraintes résiduelles dans le dépôt de leucite et dans le substrat de l'alliage de palladium.

Pour tester la méthode développée pour évaluer les contraintes résiduelles par rayonnement synchrotron, des mesures ont également été effectuées à la surface du substrat métallique, avant la réalisation du revêtement. Les résultats ont alors été comparés à des valeurs de référence obtenues par diffraction de rayons X classiques après un polissage chimique.

Des expérimentations ont d'abord été menées par diffraction des neutrons pour obtenir le profil des contraintes à la surface et dans l'épaisseur de la céramique et dans le cœur du substrat de palladium.

Des mesures par synchrotron à haute énergie ont également été nécessaires pour analyser les couches superficielles du substrat (les premiers 80 µm), les zones les plus proches de l'interface céramique/métal et naturellement le cœur du dépôt qui a déjà été caractérisé par neutrons.

Les résultats obtenus par diffraction neutronique et par rayonnement synchrotron ont montré que pour analyser les données des mesures proches de la surface ou de l'interface céramique/métal, il faut considérer, à la fois les aberrations optiques liées à l'instrumentation pour les mesures avec les neutrons, et la très forte absorption du rayonnement pour les expérimentations réalisées au synchrotron.

CHAPTER 1

MATERIALS FOR DENTISTRY APPLICATION

1.1 Dental ceramics: general

Ceramics are one of three basic materials found in nature. The others are metals and polymers. Mixtures of any of these produce composites. Ceramics are produced when metals combine with non-metals. They are non-metallic, inorganic materials that contain metal oxides whose structure is crystalline, displaying a regular periodic arrangement of the component atoms and may exhibit ionic or covalent bonding. Ceramics possess both ionic and covalent bonds. The ionic bonding holds the structure together and the covalent bonding provides chemical resistance. This combination produces materials which have great chemical stability, have high melting points, great rigidity and hardness [1.1].

Ceramic materials have been used in dentistry for well over 200 years. They are biocompatible because they are chemically very stable. Essentially, they are metallic oxides which are in the lowest energy state.

1.2 Dental porcelains

Dental ceramics include porcelains and glass-ceramics[I]. It is important to note that: all porcelains and glass-ceramics are ceramics, but not all ceramics are porcelains or glass-ceramics. Dental ceramics are used to create crowns, veneers, inlays, onlays and denture teeth A desirable feature of ceramics is that their appearance can be customised to simulate the colour, translucency and fluorescence of natural teeth. They are biologically and chemically inert, inherently brittle with a good resistance to abrasion [1.2].

Conventional dental porcelain is a vitreous ceramic based on silica (SiO_2) network and potassium feldspar ($K_2O\ Al_2O_3 \cdot 6SiO_2$) or sodium feldspar ($Na_2O\ Al_2O_3 \cdot 6SiO_2$) or both[II]. Silica can exist in four different forms[III].

Dental porcelains are essentially mixtures of fine particles of feldspar and quartz. The feldspar melts first to provide a glassy matrix for the quartz, which is held in suspension within the matrix. Its fusion temperature is very high [1.3].

The structural basis of dental porcelain can be chemically and physically modified by agents (generally in the form of oxides). They can be broadly categorised as follows:

- network-modifying oxides (e.g. K_2O, Na_2O, CaO and Li_2O)
- network-forming oxides (e.g. Al_2O_3 and B_2O_3)
- opacifent oxides (e.g. ZrO_2, SnO_2)
- fluorescent oxides (e.g. CeO_2)

More in detail:

- **Network-modifying oxides**

While chemically very inert, vitreous silica is not suitable as a fusible ceramic medium in dentistry due to the relatively high fusion (glass transition) temperature involved (ca 1300°C).

[I] *Glass-ceramic: a solid consisting of a glassy matrix and one or more crystal phases produced by the controlled nucleation and growth of crystals in the glass.*

[II] *Feldspar: a range of natural crystalline minerals (principally in igneous rocks) consisting of silicates of aluminium with potassium, sodium, calcium and rarely barium;* $X_2O \cdot Al_2O_3 \cdot 6SiO_2$ *where X is either Na or K.*

- *potassium feldspar or potash feldspar –* $K_2O \cdot Al_2O_3 \cdot 6SiO_2$
- *sodium feldspar or soda feldspar -* $Na_2O \cdot Al_2O_3 \cdot 6SiO_2$
- *calcium aluminium feldspar or lime feldspar –*$CaO \cdot Al_2O_3 \cdot 2SiO_2$.

Structurally, vitreous silica involves the network connection of tetrahedral silicate moieties, but without the long-term repeat pattern of the corresponding crystalline systems (quartz and cristobalite). The function of network-modifying oxides is to partly disrupt this network structure, through the introduction of ionic bonds, so that the fusion temperature is reduced. However, excessive modification via network-modifying oxides can increase the chemical reactivity of the glass, with increased tendencies towards dissolution and devitrification. Potassium oxide (K_2O), in suitable concentration, also has the effect of increasing the thermal expansion of the porcelain through the formation of crystals of leucite ($KAlSi_2O_6$, coefficient of thermal expansion - CTE = $20 - 25{\cdot}10^{-6}$ /°K) in the material. Such porcelain compositions are suitable for chemical bonding to metal.

- **Network-forming oxides**

From the formal ionic viewpoint, metal cations, such as Al^{3+}, B^{3+} and P^{5+}, can be accommodated by substitution for Si^{4+} in the structural network of vitreous silica. The effect of such substitutions is to modify the physical properties of the resultant ceramic.

- **Opacifent oxides**

If opaque dental porcelain is required, opacifents such as ZrO_2 and SnO_2 can be incorporated in the production of the material. For example, the aluminous porcelain serves as an opaque material.

- **Fluorescent oxides**

Human dental enamel is fluorescent. This implies that photons of a particular ultraviolet (UV) wavelength range can be absorbed. The electronically excited species produced within the enamel return to the electronic ground state with the emission of photons of visible light. Thus, in daylight, the visible light obtaining from the surface of enamel is partly by reflection and partly by emission due to fluorescence. It is desirable that such an effect should be present in dental porcelain. Formerly a system based on light emission from certain compounds activated by the radioactive decay of UO_2 was used; more recently, CeO_2 has been employed.

The glass-ceramic is at least 50% crystalline. Glassy ceramics have properties that are equivalent to those of enamel.

Its principal characteristics are:

[III] *Quartz or Silica: chemically resistant dioxide, SiO_2, occurs naturally in the 3 crystalline modifications of quartz, tridymite and cristobalite, in amorphous and hydrated forms and in less pure forms (sand, etc…).*

- Natural appearance similar to enamel
- Easy to finish and polish
- High chemical resistance
- Compatible thermal coefficient
- Low electrical conductivity
- High abrasion resistance

Three different types of porcelains are used in dentistry (Table 1.1):

- Denture tooth porcelain which is a high-fusing porcelain;
- Feldspathic dental porcelain which begins as a mixture of potassium feldspar and glass;
- Aluminous porcelain composed of mixtures similar to that of feldspathic porcelain[IV] but with increased amounts of aluminum oxide [1.4].

	Fusion temperatures of dental ceramics
Low fusing	850 - 1100° C
Medium fusing	1100 - 1300° C
High fusing	1300 - 1400° C

Table 1.1: Dental porcelains.

After firing, all three types of porcelains contain similar components: small crystals (leucite and/or other alumino-silicate crystals) embedded in a silicate glass (a non-crystalline, amorphous matrix).

Leucite ($KAlSi_2O_6$), a reaction product of potassium feldspar and glass, is a particularly important component in dental porcelain because it affects the optical properties, thermal expansion, strength and hardness of the porcelain.

[IV] *Feldspathic porcelain: a ceramic composed of a glassy matrix phase and one or more crystalline phases one of which is leucite ($K_2O \cdot Al_2O_3 \cdot 4SiO_2$) which is used to create high-expansion porcelain that is thermally compatible with metal alloy core substructures; a more technically correct name for this is leucite porcelain because feldspar is not present in the final processed porcelain nor is it necessary as a raw material to produce leucite crystals.*

Glass is described as supercooled liquids, structureless or truly amorphous[V]. In liquids, structural units or arrangements of atoms exist as they do in crystalline solids, but these units are not arranged in a regular manner. Glass is an inorganic product of fusion, which has cooled to a rigid condition without crystallisation [1.6].

Glass mainly consists of a three-dimensional network structure of silica in which each silicon atom is bonded to four oxygen atoms in the form of a tetrahedron. These tetrahedra are linked together by sharing common oxygen atoms to form a continuous three-dimensional network.

The introduction of oxides of alkali metals (e.g. *network forming oxides*) into silica glass composition results in disruption of the three-dimensional structure formed by the oxygen-silica bonds. They cause a lowering of the fusion temperature[VI], together with a reduction in strength and chemical inertness. Thus, fusion temperature, strength and chemical inertness depend on the amount of alkali presents in the glass.

1.3 Leucite

Feldspars are essentially aluminum silicates combined with varying percentages of potassium, sodium, and calcium. Feldspathic porcelains are ceramics composed of glassy matrix phase and one or more crystalline phases. One of these is leucite which is used to create high expansion porcelain that is thermally compatible with the metal alloy core substructures.

An important property of feldspar is its tendency to form the crystalline mineral leucite when it is melted, which has a high CTE ($20 - 25 \cdot 10^{-6}$/°K) compared to feldspar glasses (about $10 \cdot 10^{-6}$ /°K) [1.6].

Leucite is one of the most important feldspathoid mineral. The crystal form of leucite indicates the conditions under which it was crystallised, and the tetragonal structure. More details are shown in Table 1.2:

[V] Amorphous: *without definite form or shape; formless; without real or apparent crystalline form; uncrystallised.*

[VI] *While pure (100%) silica glass fuses at about 1700°C.*

General information	
Chemical Formula	$KAlSi_2O_6$
Composition (%)	Molecular Weight = 218.25 g
	Potassium: 17.91
	Aluminum: 12.36
	Silicon: 25.74
	Oxygen: 43.99
Empirical Formula	$KAl(Si_2O_6)$
Environment	Acid volcanic rocks
Crystallography	
Axial Ratios	c : a = 1.0528
Cell Dimensions (nm)	a = 1.30654, c = 1.37554, Z = 16; V =235.604
Crystal System	Tetragonal - Dipyramidal H-M Symbol (4/m) Space Group: $I4_1/a$
Physical properties	
Cleavage	[110] Indistinct
Colour	Colourless, grey, yellow grey, or white
Density	2.47
Luster	Vitreous (Glassy)

Table 1.2: Leucite properties [1.7].

1.4 Mechanical properties of brittle materials

Mechanical properties are the source of the greatest benefits as well as the most severe limitations of ceramic materials. The characteristic properties of porcelain are hardness, strength, aesthetic, opacity, translucency, insolubility in oral environment, extreme biocompatibility, and resistance to thermal and chemical attack. Due to their relatively inert behaviour in aggressive environments, their high hardness and wear resistance, and their ability to resist significantly higher temperatures than metals or polymers, ceramic materials offer the potential for major improvements in component design for a wide range of applications [1.1]. On the debit side, however, ceramics typically exhibit statistically variable brittle fracture, environmentally enhanced sub-critical crack growth, sensitivity to machining damage, and creep-deformation behaviour at elevated temperatures.

The major weakness of ceramics is their inability to flex and their relative tendency to fracture at a minimum deformation of 0.1%. Microscopic surface defects, under load lead to crack propagation and eventually to catastrophic failure. Porcelain has high compressive strength but low tensile strength.

A major problem with the use of ceramics as tooth replacement materials is their very low fracture toughness (the energy required to propagate a crack). In other words, the ceramic structure only exhibits a very low flexibility before fracture [1.8].

Currently, the ceramic material used in dentistry utilises molten glass containing alumina Al_2O_3 or leucite $KAlSi_2O_6$ to stop crack propagation.

Alumina is an opaque, white solid used as a reinforcing agent limited by its influence on the translucency of dental porcelain to cores. However, the greatest strength comes from combining a metal substrate with an aesthetic veneer of porcelain.

Cracks can propagate from surfaces placed under tension. Such forces can be generated in bending. Alumina particles opposes the propagation of the crack by blocking its movement, generating a compressive stress, filling in the cracks (as with glass infiltration), or preventing opening of the crack (as in bonding the porcelain to a metal substrate). Alumina increases the resistance of the porcelain to fracture; i.e. it will be strengthened. Another problem is that if the ceramic structure is formed by the condensation and sintering of fine frit particles (See § 1.4), fusion is accompanied by a relatively large firing shrinkage.

1.5 Porcelain technology in brief

In the dental production laboratory, objects are manufactured in dental porcelain through heating a suitably - shaped agglomerate of porcelain particles to the fusion temperature (ca 950 - 980 °C).

A briefly approaches to the manufacturing of dental restorations in a ceramic may broadly be classified in terms of three general procedures [1.1], [1.9]:

- Sintering [VII]
- Casting (and ceramming, i.e. glass-ceramics)
- Mechanical preparation

The general appeal of dental ceramics is with respect to corrosion and surface hardness. In addition, the appeal of dental porcelain is with respect to aesthetics.

The constituents of dental porcelain are mixed together, fired[VIII] and poured into water to produce a frit[IX]. The porcelain thus produced is then ground, sieved and packed. In the dental laboratory, the powder is used as slurry.

Firing in a vacuum cause the particles to sinter together and the porosity to decrease. A considerable degree of shrinkage occurs on firing.

The pure powder are fired together (calcined[X]) by the manufacturer to form a fused mass, a frit, which is then ground again to a fine powder. Firing shrinkage must be equivalent to the decrease porosity which is 30 – 44 vol. %. During firing, the water evaporates which causes shrinkage. Therefore, the less water present when firing is started, the less shrinkage. Water and air lead to voids.

[VII] *Sintering: the process of by partial fusion by point contact of particles. Although there is not a fusion of the porcelain powder particles, they join together by flow on contact as a result of surface energy resulting in densification by viscous flow of a ceramic or glass powder, produced by heating or heat and pressure.*

[VIII] *Firing is different than melting; solids melts, porcelains are fired. The feldspar is used to begin the vitrification process when the materials are subjected to firing for ceramic use.*

[IX] *Frit: materials of which glass is made after having been calcined or partly fused in a furnace but before vitrification.*

[X] *Calcined: to heat without fusing to a high temperature in order to effect useful physical and chemical properties: drives off impurities)*

1.6 Dental casting alloys: general

Since the introduction of casting alloy to dentistry in 1907, precious metal alloys have traditionally been used for several types of restorations. Alloys for Porcelain Fused to Metal (PFM) have revolutionised this field and include palladium alloys.

Metals are usually crystalline materials with an ordered structure. The atoms are arranged on lattices. However, there are defects in the crystal structure that may take the form of missing atoms (vacancies), larger atoms occupying sites normally occupied by atoms smaller in size (substitutions), extra half planes of atoms seemingly inserted into the crystal (dislocations), etc. The *dislocations* are responsible for the plastic deformation. The degree of plastic deformation depends on the metal or alloy and is called the ductility of the metal. The *ductility* is usually given as a percentage change of one or more of the dimensions of the component.

The fact that metals and alloys are ductile allows them to be shaped without the need for melting and pouring into moulds (*casting metals*). The amount of energy required to move dislocations through the crystal structure is related to the strength of the material.

Pure metals have a fairly low strength (it is relatively easy to move the dislocations), whereas alloys generally have high strength. So pure metals are too soft to be of use in structural applications and need to be hardened, usually by forming an alloy. By altering the structure of metals and alloys these materials can be hardened and softened which is particularly useful for dental applications.

Hardness is related to strength so that materials with high hardness have high strength.

A common method of forming alloys is to melt together the appropriate quantities of the components and to allow the combination to cool. A number of effects may be observed based on the attempted formation of alloys through this approach. These effects depend on the following:

- Relative atomic sizes of the components
- Type of lattice of each component
- Electronic properties of each component

At the atomic scale metals and alloys consist of ordered arrangements of atoms. Defects may however exist within the structure.

When metals and alloys are melted and cast into a shape that is useful for dental prostheses, the liquid metal cools and solidifies. Solidification takes place through the *nucleation* and *growth* of solid particles in the liquid metal. Each solid particle is a crystal made up of arranged atoms, known as *grains*. As the liquid solidifies the grains are growing at the expense of the liquid until each grain impinges on the next at a foreign solid particle. The whole grains may have the same crystal structure but their orientation will be different.

Grain boundaries are important regions in metals and alloys because they often have a significant influence on the mechanical properties of the material. For example, metals with large round grains have low strength and high ductility whereas those with small elongated grains can have high strength and low ductility. Grain boundaries can also prove to be a critical feature during breakdown of metal structures through corrosion [1.10].

Cooling a molten metal to room temperature usually results in solidification (an exception is mercury). The transformation from liquid to solid involves a *phase change*, the conditions for which are summarised in the relevant single-component phase diagram. As most procedures are carried out at atmospheric pressure, the temperature is, effectively, the sole variable for a given metal. Thus, at a particular temperature, both the solid and liquid phases can exist in equilibrium - the *melting point*.

1.7 High-content palladium casting alloys

Casting[XI] metals are those which are heated to form a liquid. The molten metal is poured into a mould where it solidifies. Different shapes can be fashioned in this way. A generalised casting is called an ***ingot.***

An alloy is a specific combination of two, or more, metals (or metals and non-metals) in the solid state. It may be a solid solution or a multiphase structure. An alloy consisting of two elements is termed a binary alloy, three elements, a ternary alloy, etc.

[XI] *A casting is produced when molten metal is allowed to cool in a mould.*

In the 80's, alloys featuring a high palladium content have been developed for the porcelain fused to metal technique. Palladium content is usually in the range 75-78 % wt. and the alloys are based on one of the ternary systems; *Pd-Ag-S*n (or *Pd-Cu-G*a or *Pd-Co-Ga)*. The material investigated in our study is based on the Pd-Ag-Sn system and contains also small quantities of Ga (3%), Ru and In (<1 %).

The *atomic diameter* of the metal elements is important because it influences the way at which the elements mix. Elements of similar diameter mix well and can replace each other on the *metal lattice (*a regular geometrical arrangement of points in crystal space). They are said to form a *solid solution* and exhibit *complete solid solubility* (e.g. Palladium and Silver) (Table 1.3). Elements, which do not have similar diameters, do not mix well because they tend to distort the metal lattice. This limits the degree of solubility of one element in the other and the metals are said to exhibit *limited solid solubility (*Tin into Palladium*)*.

Silver and palladium feature full solid solubility. Palladium features a strong affinity for hydrogen gas, it is one of the platinum group metals and is relatively high melting (MP = 1552 °C). Silver (Ag) is lower melting (MP = 962 °C), making it more suitable as the basis of a dental casting alloy, but tarnishes easily in the presence of hydrogen sulphide. Silver can be protected from tarnishing through the addition of palladium. The degree of protection is determined by the quantity of palladium present.

diameters (nm)	**element**	**structure**
0.2889	Silver (Ag)	CFC
0.3016	Tin (Sn)	CFC
0.2751	Palladium (Pd)	CFC

Table 1.3: Diameters of metal atoms.

1.7.1 Platinum group

The mechanical properties of the six platinum metals differ greatly. Platinum and palladium are rather soft and very ductile; these metals and most of their alloys can be worked hot or cold. Rhodium is initially worked hot, but cold working can be done later with rather frequent annealing. Iridium can be worked hot, as can ruthenium, but with difficulty; neither metal can be cold-worked appreciably. Osmium is the hardest of the group and has the highest melting point, but its ready oxidation is a limitation. Iridium is the most corrosion-resistant of the platinum metals, while rhodium is valued for retaining its properties at high temperatures.

1.7.2 Palladium

Palladium (Pd), chemical element, lightest and lowest melting of the platinum metals of Group VIII of the periodic table (Figure 1.1), used especially as a catalyst (a substance that speeds up chemical reactions without changing their products) and in alloys. A precious, grey - white metal, palladium is extremely ductile and easily worked. The atmosphere at ordinary temperatures does not tarnish palladium. It is therefore used in dental alloys.

Atomic number	Atomic weight	Melting point	Specific gravity	Valence	Electronic configuration
46	106.40	1552º C	11.97 (0º C)	2, 4	2-8-18-18 or (Kr)$4d^{10}$

Table 1.4: Palladium properties.

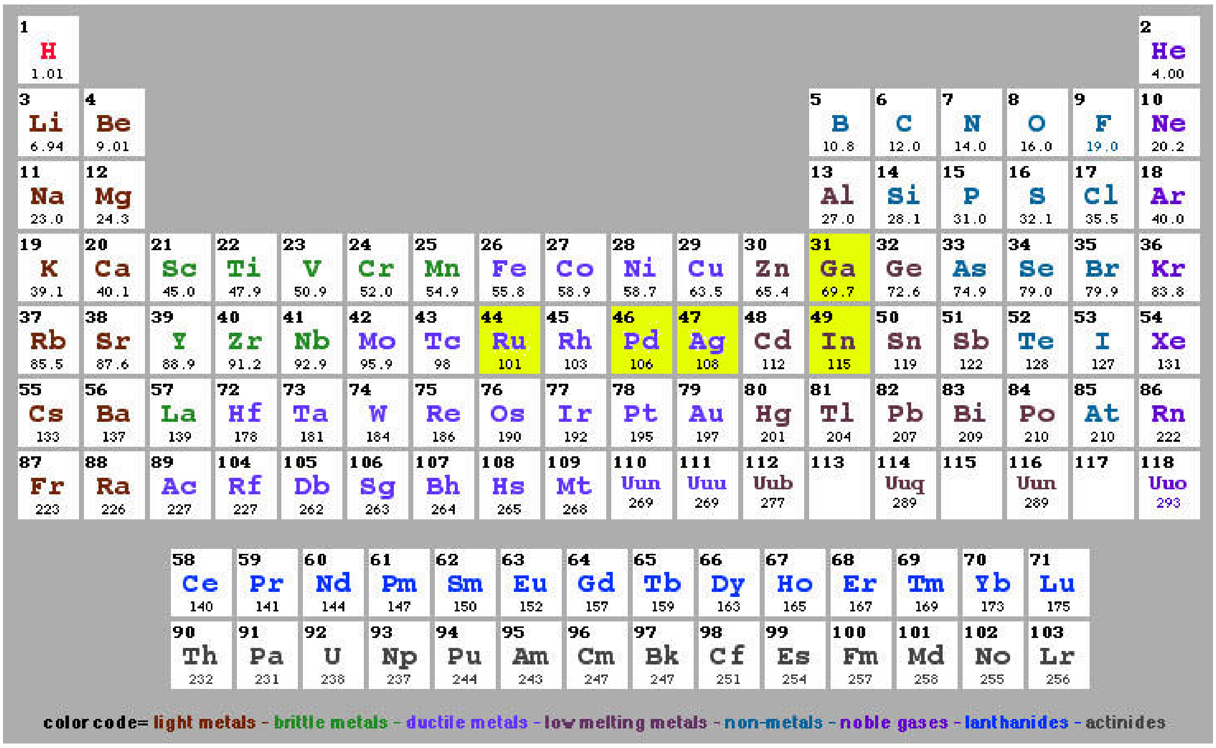

Figure 1.1: Periodic table of elements.

1.8 CerapallÒ alloy

In following some details about the elements in our Cerapall® alloy:

- **Palladium (Pd)** - White (silver-coloured) metal of the platinum group. It is highly noble in the mouth. Palladium has a higher intrinsic strength and hardness than gold, a much higher melting point, and a higher modulus of elasticity. The thermal expansion of palladium is too low to be used with most commercial porcelains; it is therefore used to lower the expansion of gold-based PFM (Porcelain Fused To Metal) alloys.

- **Silver (Ag)** - In PFM alloys, it is used primarily to raise the thermal expansion of palladium. Silver lowers the melting range of both palladium and gold. It is claimed to add fluidity to casting alloys and solders. Silver can cause discoloration of some dental porcelain, a phenomenon known as "greening." However, because of the very positive effects silver has on the thermal expansion (and cost!) of an alloy, most modern porcelains are designed to resist this discoloration.

- **Tin (Sn)** is used as a strengthener and hardener in both gold and palladium PFM alloys. Tin lowers the melting range of both gold and palladium, and raises the thermal expansion. Tin contributes to bonding oxide formation.

- **Gallium (Ga)** is used almost exclusively in palladium based PFM alloys. Gallium can be a potent strengthener, and it lowers the melting range of palladium.

- **Ruthenium (Ru)** and **Indium (In)** are used primarily as grain refiner.

1.9 Porcelain fused to metal (PFM)

Porcelain Fused to Metal (PFM) system was introduced in the 1950s. A development in 1962 greatly improved these systems; that is, the incorporation of a high proportion of leucite crystals into the feldspathic porcelain composition, which veneered the cast palladium/gold alloy substructure. The leucite crystals serve to increase the thermal expansion of the porcelain to bring it closer to that of the metal substrate. The leucite prevents stresses occurring, due to a thermal mismatch, which could lower the strength.

Metals are between 10 and 100 times tougher than ceramics; the presence of a metal substrate can contribute to a very strong restoration. The incorporation of a small trace of tin and/or silver into the palladium alloy was necessary to allow formation of the necessary oxide on the surface to permit good wetting by the porcelain and subsequent bonding to the alloy surface.

An opaque ceramic such as a titanium oxide glass frit has to be applied as the first layer of veneer, to mask the metallic substrate in the PFM systems.

Although the PFM systems have high strength, the opacity of the metal substructure has encouraged the development of all-ceramic core materials containing crystalline components which are stronger than the traditional (predominantly glassy amorphous) feldspathic porcelain. This type of core material can then be veneered with a more translucent ceramic material [1.11].

In this approach, a permanent shell is cast in an appropriate alloy and is used to support the porcelain, which acts as a veneer. Appropriate choices of alloy and porcelain allow chemical bonding to occur at the interface. As with glazing, this has the effect of restricting crack propagation. For successful porcelain to metal bonding, the coefficient of thermal expansion of the porcelain has to be increased (through a suitable composition) to closely match that of the metal (about 5-10% less than that of the metal).

Dental porcelains have been discussed in this chapter. The aesthetic appeal of porcelain, coupled with relative inertness in the mouth, make for a desirable restorative material [1.12]. However, dental porcelain is brittle and will only tolerate relatively small strains (about 0.1 %) before failure. The utility of dental porcelain, as a restorative, can be extended in the "porcelain fused to metal" technique.

A thin layer of dental porcelain is fused to a metal casting which then presents an aesthetic crown, bridge, etc. The technique can also be termed "enamelling" [1.2].

The coefficient of thermal expansion **(CTE or a_t)** of the porcelain must be suitably matched with that of the alloy and the melting range of the alloy must be raised sufficiently above the fusion temperature of the porcelain for a successful enamelling operation. [1.14].

It is important that the alloy does not contain components (such as copper) which form coloured oxides, at the interface, or which give rise to colour effects within the porcelain.

Material	**a_t (µm/mk)** **@25-500 °C**	**E (n/mm^2) MPa**	n	**Melting range (°C)**
Cerapall®	14 $x10^{-6}$ [1.15]	124000 [1.15]	0.39 [1.15]	1160-1300 [1.15]
Leucite crystal	20-25 $x10^{-6}$ [1.16], [1.17]	--------	--------	--------
Will- Ceram® opaquer	13.95 $x10^{-6}$ [1.18], [1.19]	63000 [1.20]	0.19 [1.21]	680
Will- Ceram body® (dentine)	13.65 $x10^{-6}$ [1.18], [1.19]	63000 [1.20]	0.19 [1.21]	650
Feldspar glass	10 $x10^{-6}$ [1.16], [1.17]	70000 [1.22]	0.23 [1.22]	--------

Table 1.5: Mechanical properties of constituent samples.

An important property of feldspar is its tendency to form the crystalline mineral leucite when it is melted which has a high CTE ($20 - 25 \cdot 10^{-6}$/°K) compared to feldspar glasses ($10 \cdot 10^{-6}$/°K).

The bond between metal and porcelain is a combination of the results of [1.18]:

- Wetting by the molten glass (Van der Waals' forces - physical)
- Retention by surface roughness of the cooled glass (mechanical)
- Diffusion of metal oxides into the porcelain (chemical)
- Differences in thermal expansion on cooling (compressive) [1.23].

- If the <u>metal shrinks</u> much more than the porcelain, the porcelain fractures and drops off
- If the <u>porcelain shrinks</u> much more than the metal, the porcelain crazes
- If the <u>metal/porcelain sandwich bends under load</u> the brittle ceramic may fracture and de-bond

There are two bonding mechanisms possible whereby dental porcelain may be retained to the structure of a metal casting:

- Mechanical interaction
- Adhesion (chemical bonding)

The mechanical bonding of porcelain with metal results from fusion of the porcelain into undercuts in the metal surface. Before fusion of the porcelain, this metal surface must be clean and degreased.

The direct chemical bonding of porcelain to metal seems to be unlikely. However, certain metal ions can be incorporated into dental porcelain, outside of the chain network, in the form of "network-modifying oxides" (see § 1.1). If these metal ions are obtained from the surface of the metal casting, a gradual structural transition between pure oxide and pure metal may be achieved. Such circumstances would make chemical bonding possible. In effect, chemical bonding of porcelain to metal is obtained by fusion of the porcelain to a metal oxide layer on the surface of the casting. Ideally, this surface oxide layer should be extremely thin and continuous with the underlying metal structure. In practice, the oxide layer may be a "passive layer".

This oxide surface is then chemically compatible with the porcelain (some metal ion migration will also occur) to allow chemical bonding.

Resuming: Dental alloys must be: inert, rigid and strong. They must:

- be rigid in thin section to resist bending (which would fracture or dislodge the porcelain)
- Assist in the formation of a chemical bond with the porcelain
- Have a similar coefficient of thermal expansion to the porcelain, so that when the metal/porcelain combination cools high interfacial stresses (which could dislodge the porcelain) are not created.
- Not melt at the temperature at which the porcelain is fired

The several types of failure possible are shown in Figure 1.2.

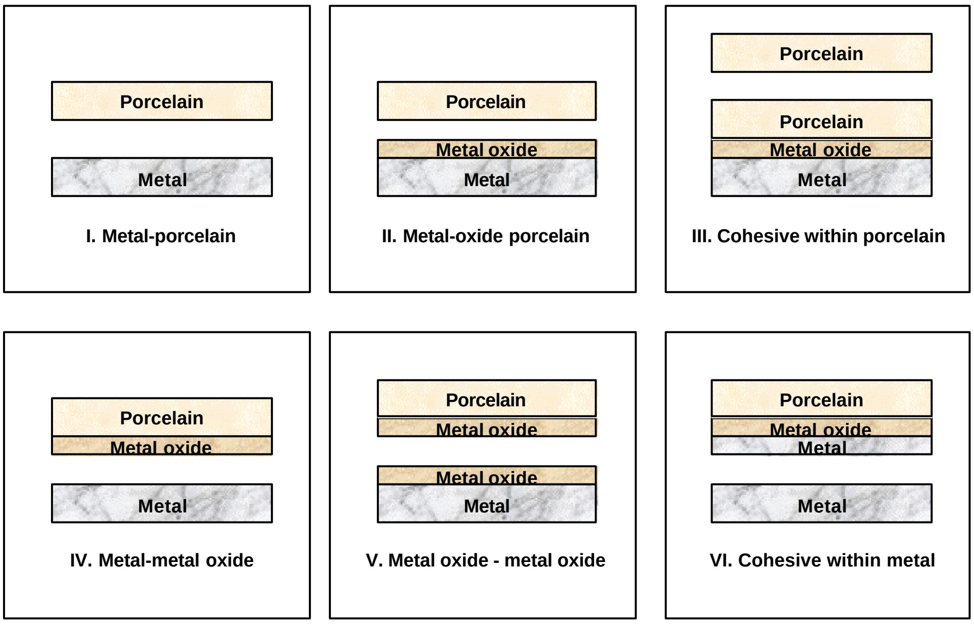

Figure 1.2: Classification of porcelain enamel failures according formed. Type III represents cohesive failure indicative of proper bond [1.3].

The main modes of failure in porcelain to metal restoration may be classified as follow:

- Failure within the porcelain
- Failure at the metal-porcelain interface
- Failure within the metal oxide layer

Tendency towards failure at the metal-porcelain interface can be reduced by so-called "compression bonding". This arises from the presence of chemical bonding and a slight mismatch in the respective coefficients of thermal expansion of the porcelain and alloy. The composition of the porcelain is such that the thermal expansion of the material is about 5-10% less than that of the alloy (the latter being $15\cdot10^{-6}$ /°K, approximately). Cooling the fused porcelain-metal combination results in the metal contracting somewhat more than the ceramic (too great a mismatch would result in shearing in the chemical bonding). Due to the presence of chemical bonding, the porcelain is subjected to a compressive strain at the interface.

This restricts the developments of cracks and strengthens the combination. For example, potassium oxide (K_2O) has the effect of increasing the thermal expansion of porcelain to the required extent (with about 12% wt).

1.10 Preparation and treatments on analysed samples

The analysed samples S and S1 are shown in Figure 1.3 and Figure 1.4.

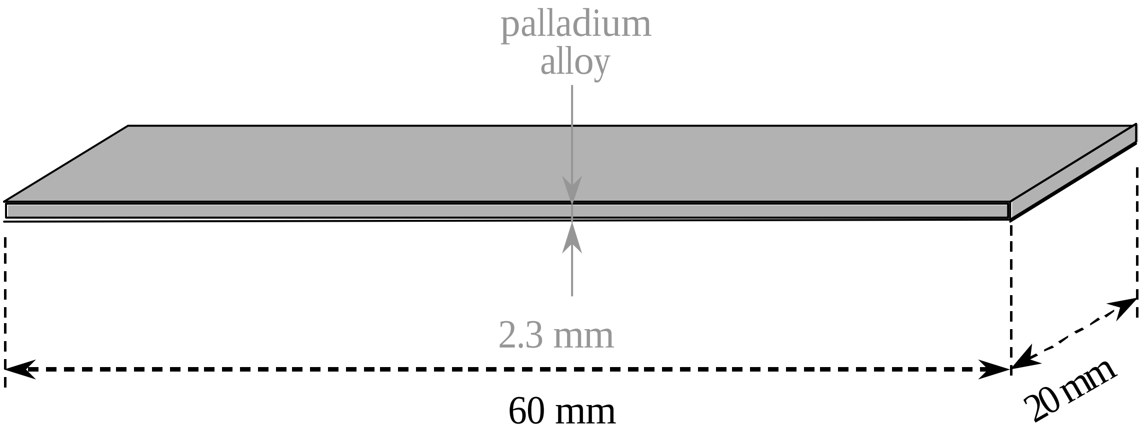

Figure 1.3: Design of analysed sample S. It represents the Pd alloy substrate *__before thermal processing__*.

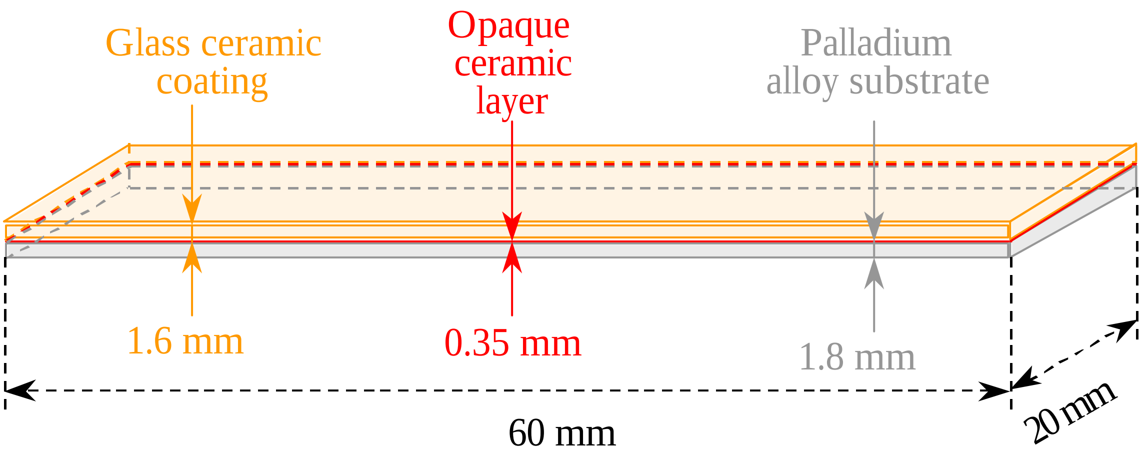

Figure 1.4: Design of analysed sample S1. Glass-ceramic coating moulded on a metal casting alloy substrate: Glassy ceramic coating (A), Ceramic interface (B) and Palladium alloy substrate (C).

Porcelain/palladium alloy was prepared following standard routines practiced by dental technicians in construction of PFM crowns. This particular metal/ceramic combination has low thermal mismatch, avoiding the generation of significant residual stresses in the coating.

Sample	Definition	Composition (wt %)
S	Pd alloy substrate before thermal processing	Pd = 75.5%, Ag = 8.1%, Sn = 11.6%, Ga = 3.0%, (Ru, In Zn) <1%
S1	A Glassy ceramic coating B Ceramic interface C Pd alloy substrate	Will - Ceram® body Will - Ceram® opaque S

Table 1.6: Description of the samples and performed analyses.

For Palladium alloy casting ingots of Cerapall® 4CF (Table 1.6 - Metalor® Ch), only new alloys were used. They were casted at 1450°C into substrate blocks 20 x 60 x 2.3 mm for sample S and 20 x 60 x 1.8 for sample S1. For each sample, a high-heat phosphate investment was used. The size of these samples does not be normally reached by common dental laboratories.

These blocks were then ground flat on opposite faces. Only the metallic substrate (C see Figure 1.4) of sample S1 was sandblasted with alumina Al_2O_3 (50 µm to 125 µm*)* to provide good bounding for the ensuing coating. Finally it was oxidised 10 minutes at 980°C /atmosphere.

The porcelains selected for the experiment were:

- Will - Ceram® opaque for the inner layer (B see Figure 1.4)
- Will - Ceram® body for the exterior layer (A see Figure 1.4)

A first coating was prepared by opaque powder (Williams Will - Ceram opaque). It was mixed in slurry and applied to the whole surface of substrate with a paintbrush. It gives a regular layer of opaque (approximately 100 µm after heating). Layer was sintered according to the following firing cycle:

Heat to 980°C in vacuum and hold for 1 minute, it produces the real first layer of opaque that will hide the alloy. The top surface of porcelain coatings was then sandblasted (alumina, 50 µm).

A second opaque layer is normally optional. It has been used for this sample and its role is to complete to hide the metallic effect of the substrate, as the size of the samples was particularly important. The second opaque layer was heat to 980°C for 1 minute under vacuum.

Concerning the dentin layer (glassy ceramic coating, William body powders) only was heat to 950°C for 1 minute.

Their physical-mechanical properties such as modulus of elasticity, hardness, and coefficient of thermal expansion are very close to natural enamel.

Glass may be defined as a rapidly undercooled liquid with an amorphous, non-crystalline structure. When glass melt is cooled slowly, crystals develop. Glassy ceramics are produced from raw glass by controlled crystallisation. One or more types of crystals embedded in one or more vitreous phases result from this "ceramming" process.

Empress glassy ceramics consist of crystals and a vitreous phase. The glassy matrix merely forms a putty between abundant leucite crystals.

Different factors account for the improved mechanical properties of these materials. One factor is the stress which is set up in the vitreous phase as a result of the high shrinkage of the leucite crystals. Secondly, the leucite crystals with a mean diameter of 3 micrometer are believed to stop the propagation of micro-cracks within the glassy matrix. The wear of Empress glassy ceramics is in range of enamel. As a result of its fine-grain structure, the glassy ceramic abrades the antagonist (opposing dentition) enamel not more than natural enamel.

For more information about porcelains, see also the page explaining porcelains in more detail.

References

[1.1] Van Vlack L. H., Materials for Engineering, Addison - Welsley (1982) AB 92 - chapter 11, 12, 13 and 15.

[1.2] Biomatériaux de prothèse, pg 202-213.

[1.3] O'Brien WJ; Dental Materials Properties and Selection, 1989.

[1.4] Moffa JP: Porcelain Materials. Adv. Den. Res. 2(1): 3-6; Aug 1988.

[1.5] Phillips RW; Elements of Dental Materials, 1984. Fundamental of materials technology chapter 7.

[1.6] Doremus RH, Review bioceramics, Journal of Materials Science Vol.27, 285-297 (1992).

[1.7] Enc. Of Minerals, 2nd ed.,1990.

[1.8] McLaren EA: All-Ceramic Alternatives to Conventional Metal/ceramic Restorations. Compendium 307-325, March 1998.

[1.9] Craig RG; Restorative Dental Materials, 1997.

[1.10] Braithwaite N. and Weaver G., Electronic Materials, Open University, Butterworth (1990) chapter 4.

[1.11] Denry IL. Recent advantages in ceramics for dentistry. CRIT Rev. Oral Biol. Med. 7: 134-143, 1996.

[1.12] Giordano RA: Dental Ceramic Restorative Systems. Compendium 17(8): 779-793, Aug 1996.

[1.13] Leinfelder KF, Lemons JE: Clinical Restorative Materials and Techniques, 1988.

[1.14] Anusavice KJ. et al., Interactive effect of stress and temperature on creep of PMF alloys, J. Dent. Res. 64: pp1094-1099, 1985.

[1.15] Metalor® Data sheet.

[1.16] O'Brien WJ, Dental Materials and Their Selection, 2nd ed., 1997 edited by O'Brien WJ and published by Quintessence Publishing.

[1.17] Kon M et al., Effect of leucite crystals on the strength of glassy porcelain, J Dent. Mater. 13(2): 138-147, 1994.

[1.18] Whitlock RP, Tesk JA, Widera, GEO, Holmes A. and Parry EE: Consideration of some factors influencing compatibility of dental porcelains and alloys. Part I. Thermo-physical properties. pp. 273-282. In Proc. 4th Int. Precious Metals Conference, Toronto, June 1980. Willowdale, Ontario: Pergamon Press Canada, April 1981.

[1.19] Fiches de donnees Williams international.

[1.20] Seghi RR, Denry I., and Brajevic F: Effects of ion exchange on hardness and fracture toughness of dental ceramics. Int. J. Prosthodont. 5:309-314, 1992.

[1.21] Kase HR, Tesk, JA and Case ED. Elastic constants of two dental porcelains Journal of Materials Science., 20:524-531, 1985.

[1.22] Baipai PK, Billotte WG 1995, Ceramic Biomaterials in The Biomedical Engineering, Handbook, Bronzino JD, Ed. CRC Press, Boca Raton, FL chap. 41, 552-580.

[1.23] Klomp JT, Ceramic and metal surfaces in ceramic-to-metal bonding, Proceedings-of-the-British-Ceramic-Society. no.34; Aug. 1984; p.249-59.

CHAPTER 2

THEORY OF THE EVALUATION OF RESIDUAL STRESS BY DIFFRACTION METHODS

2.1 Introduction

In X-ray or neutrons diffraction residual stress evaluations, the strain in the crystal lattice is measured, and the residual stress is calculated, assuming a linear elastic distortion of the crystal lattice. Although the term stress measurement has come into common usage, stress is an extrinsic property that is not directly measurable. All methods of stress determination require measurement of some intrinsic property, such as strain or force and area, and the calculation of the associated stress.

Mechanical methods (sectioning techniques) and non-linear elastic methods (ultrasonic and magnetic techniques) are limited in their applicability to residual stress determination. Mechanical methods are limited by assumptions concerning the nature of the residual stress field and sample geometry. They cannot be directly checked by repeat measurement being necessarily destructive [2.1].

All non-linear elastic methods are subject to major error from preferred orientation, cold work, temperature, and grain size. All require stress-free reference samples, which are otherwise identical to the sample under investigation. Non-linear elastic methods are generally not suitable for routine residual stress determination at their current state of development. In addition, their spatial and depth resolutions are orders of magnitude less than those of X-ray or neutrons diffraction.

2.2 Plane stress elastic model: general approach

To determine the stress, the strain in the crystal lattice must be measured for at least two precisely known orientations relative to the sample surface. Therefore, X-ray or neutrons diffraction residual stress measurement is applicable to materials that are crystalline, relatively fine grained, and produce diffraction for any orientation of the sample surface.

Samples may be metallic or ceramic, providing diffraction peaks of suitable intensity and free of interference from neighbouring peaks. Diffraction residual stress measurement is unique in that macroscopic and microscopic residual stresses can be determined non-destructively.

Macroscopic stress (or strain), or macro-stress (macro-strain), which extends over distances that are large relative to the grain size of the material, is of general interest in design and failure analysis.

Macro-stress (or strain) is a tensor quantity which magnitude varies at different points in a body. It leads to a uniform distortion of the crystal lattice and produces a shift of the diffraction peak selected for residual stress evaluations. The macro-strain component for a given location and direction is determined by measuring the lattice spacing in that direction at a single point. The lattice spacing of the unstressed material is however required to define this strain value. When the principal directions of strain (or stress) are known, just three measurements are necessary to determine the stress tensor components. The measurements are therefore carried out in those three particular principal directions. If a condition of plane stress is also assumed, no reference, unstressed sample is needed.

Microscopic stress, or micro stress, results from imperfections in the crystal. Micro-stress arises from variations in strain between or inside the crystallites bounded by dislocation tangles within the grains, acting over distances less than the dimensions of the crystal. Micro-stress varies from point to point within the crystals, producing a range of lattice spacing. This results in a broadening of the diffraction peak.

Stress/strain analysis techniques that utilise X-ray or neutron diffraction are widely applied for non-destructive testing and evaluation. The theoretical formalism used in both of these techniques is the kinematical diffraction theory for data acquisition and the theory of continuous medium and linear elasticity (linear-elastic methods) for the data treatment.

In diffraction methods, the strain is measured in the crystal lattice, and the residual stress is calculated, assuming a linear elastic distortion of the analysed volume. Diffraction results from the coherent scattering of the X-rays or neutrons on the periodic crystal structure. Only perfect domains of each grain of crystallite, called coherently diffracting domains, are therefore visible. Now, plastic deformation is produced by the movement and/or multiplication of crystal defects (vacancies, dislocations). These defects do not belong to the coherently diffracting domain and therefore do not participate directly in the diffraction. For that reason, the diffraction methods are only sensitive to the elastic strains. Nevertheless local plastic strains (or other "stress-free strains" like thermal strains or volume changes due to phase transformations) are generally incompatible and are compensated thus by elastic strains which create local residual stresses. This last effect is finally detected by X-ray or neutron diffraction.

The mechanical linear-elasticity methods are limited by simplifying assumptions concerning the nature of the residual stress field (i.e. plane stress condition) and sample geometry (i.e. flat sample).

The lattice spacing can be determined for any orientation (ϕ, ψ), relative to the sample surface by rotating the specimen. If σ_ϕ is a tensile stress, the spacing between lattice planes parallel to the surface will be reduced due to Poisson's contraction, while the spacing of planes tilted into the direction of the tensile stress will be expanded. The strain is expressed in terms of the crystal lattice spacing,

$$\varepsilon_{\phi\psi} = \frac{d_{\phi\psi} - d_0}{d_0} \qquad \textit{Eq. 2.1}$$

where d_0 is the stress-free lattice spacing and $d_{\phi\psi}$ is the lattice spacing measured in the direction defined by ϕ and ψ.

The lattice spacing will be expanded or compressed elastically by any stress present in the specimen. The state of stress within the depth of penetration of the X-ray or neutron beam can be determined by measuring the lattice spacing at different orientations to the sample surface. The only crystals which diffract X-ray/neutrons are those which are properly oriented relatively to the beam to satisfy Laue's conditions which implies Bragg's Law to be verified,

$$n\lambda = 2d\sin\theta \qquad \textit{Eq. 2.2}$$

where λ is the known X-ray/neutron wavelength, n is the integer order of reflection (typically 1 or 2), θ is the diffraction angle, and d is the lattice spacing (Figure 2.1).

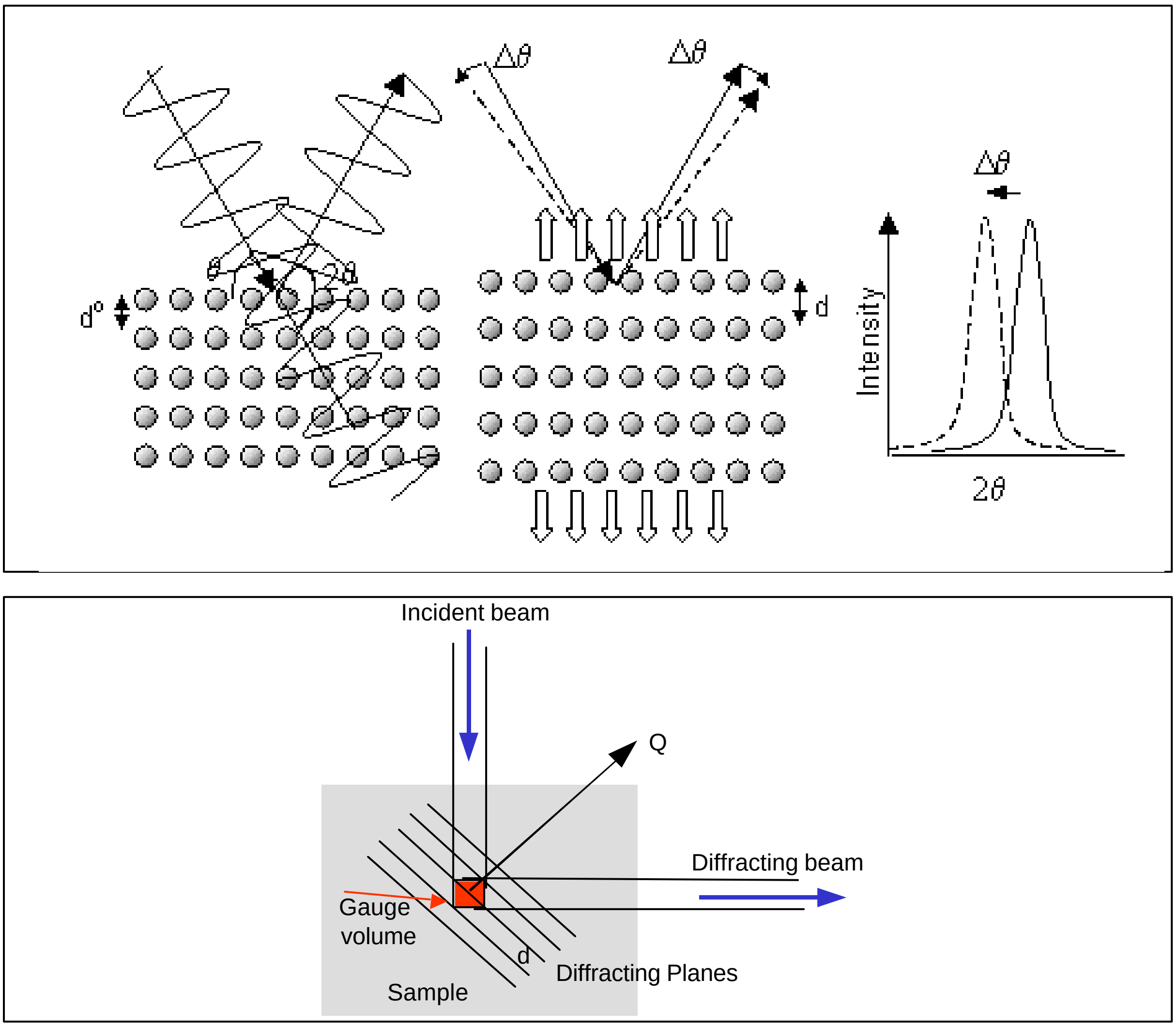

Figure 2.1: Geometrical configuration of measurement.

X-ray or neutron diffraction can be used to selectively measure the lattice spacing of only those crystals of a selected phase which have a specific orientation in relation to the sample surface by measuring θ and calculating d from Eq. 2.2.

2.3 Plane-stress elastic model: mathematical expressions [2.2], [2.3], [2.5], [2.6], [2.7], [2.8]

The condition of plane-stress is assumed to exist in diffracting plane surface layer over the following condition:

- Due to the equilibrium conditions of the surface (Eq. 2.46 - 2.47), either because of the small penetration of the radiation used (< 10 µm for classical X-rays) or because of homogeneous stresses over a large domain of a plane specimen (neutron and high energy synchrotron radiation measurements).
- The material is considered as single phase and quasi-isotropic (the diffracting crystallites must be small enough and without any preferential orientation).
- The crystallite must have a linear elastic mechanical behaviour.
- The macroscopic state of stresses and strains must be homogeneous in the whole volume irradiated (no stress gradients).

The stress distribution is then described by the stress components σ_{11}, σ_{12} and σ_{22} in the plane of the surface, with no stress acting perpendicular to the free surface, shown in Figure 2.2. The normal component σ_{33} and the shear stresses $\sigma_{13} = \sigma_{31}$ and $\sigma_{23} = \sigma_{32}$ acting out of the plane of the sample surface are zero. A strain component perpendicular to the surface, ε_{33}, exists as a result of the Poisson's ratio contractions caused by the two principal stresses.

The stress tensor is expressed in terms of following matrix:

$$\underline{\underline{\sigma}} = \begin{bmatrix} \sigma_{11} & \sigma_{12} & 0 \\ \sigma_{12} & \sigma_{22} & 0 \\ 0 & 0 & 0 \end{bmatrix} \qquad \text{Eq. 2.3}$$

and the tensor of strain will be:

$$\underline{\underline{\varepsilon}} = \begin{bmatrix} \varepsilon_{11} & \varepsilon_{12} & 0 \\ \varepsilon_{12} & \varepsilon_{22} & 0 \\ 0 & 0 & \varepsilon_{33} \end{bmatrix} \qquad \textit{Eq. 2.4}$$

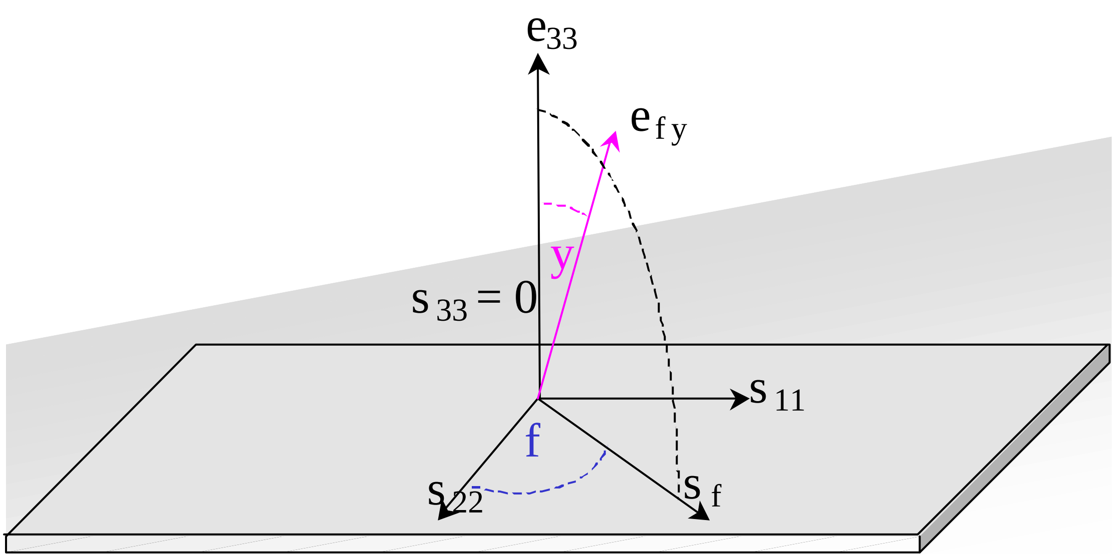

Figure 2.2: Plane-Stress.

The strain in the sample surface at an angle ϕ from the principal stress σ_{11} is then given by:

$$\varepsilon_{\phi\psi} = \left(\frac{1+\nu}{E}\right)\cdot\sigma_{\phi}\sin^{2}\psi - \left(\frac{\nu}{E}\right)\cdot\left(\sigma_{11}+\sigma_{22}\right) \qquad \textit{Eq. 2.5}$$

Substituting equation 2.1 into equation 2.5 and solving for $d_{\phi\psi}$ yields:

$$d_{\phi\psi} = \left[\left(\frac{1+\nu}{E}\right)_{(hkl)}\cdot\sigma_{\phi}\cdot d_{0}\right]\cdot\sin^{2}\psi - \left(\frac{\nu}{E}\right)_{(hkl)}\cdot d_{0}\cdot\left(\sigma_{11}+\sigma_{22}\right)+d_{0} \qquad \textit{Eq. 2.6}$$

where the appropriate elastic constants $\left(\frac{1+\nu}{E}\right)_{(hkl)}$ and $\left(\frac{\nu}{E}\right)_{(hkl)}$ are now in the crystallographic direction normal to the {hkl} lattice planes in which the strain is measured.

Because of elastic anisotropy, the elastic constants in the (hkl) direction vary.

Equation 2.6 is the fundamental relationship between lattice spacing and the biaxial stresses in the surface of the sample. The lattice spacing $d_{\phi\psi}$, is a linear function of $\sin^{2}\psi$.

The intercept of the plot at $\sin^2\psi = 0$ equals the unstressed lattice spacing, d_0, minus the Poisson's ratio contraction caused by the sum of the principal stresses:

$$d_{\phi 0} = d_0 - \left(\frac{\nu}{E}\right)_{(hkl)} \cdot d_0 \cdot (\sigma_{11} + \sigma_{22}) = d_0 \left[1 - \left(\frac{\nu}{E}\right)_{(hkl)} \cdot (\sigma_{11} + \sigma_{22})\right] \qquad \textit{Eq. 2.7}$$

The slope of the plot is:

$$\frac{\partial d_{\phi\psi}}{\partial \sin^2\psi} = \left(\frac{1+\nu}{E}\right)_{(hkl)} \sigma_\phi \cdot d_0 \qquad \textit{Eq. 2.8}$$

which can be solved for the stress σ_ϕ:

$$\sigma_\phi = \left(\frac{E}{1+\nu}\right)_{(hkl)} \frac{1}{d_0} \cdot \left(\frac{\partial d_{\phi\psi}}{\partial \sin^2\psi}\right) \qquad \textit{Eq. 2.9}$$

The elastic constants can be determined experimentally or calculated through micro-mechanical models. The unstressed lattice spacing, d_0, is generally unknown. Generally, however, the value of $d_{\phi 0}$ from equation 2.7 differs from d_0 by less than ± 0.1%, and σ_ϕ may be estimated accurately by substituting $d_{\phi 0}$ for d_0 in equation 2.9. The method then becomes thus an absolute technique, and no stress-free reference standard is required to determine d_0 for the plane-stress model.

The **$\sin^2$y technique,** assumes plane-stress at the sample surface, and is based on the fundamental relationship between lattice spacing and stress given in equation 2.6.

Lattice spacing is determined for multiple ψ tilts, a straight line is fitted by least squares and the stress is calculated from the slope of the best-fit line using equation 2.9. The primary advantage of the $\sin^2\psi$ technique, considering the additional time required for data collection, is in establishing the linearity of *d* as a function of $\sin^2\psi$.

2.4 Mechanical approach to the problem in glassy ceramic coating

The mechanical properties of glassy porcelains are known to be affected by properties of fine particles dispersed throughout the glassy matrix [2.11]. It is difficult to analyse the mechanical strength of dental porcelain, which contain leucite crystal with a large expansion coefficient because of the mismatch of thermal expansion between the leucite and the glassy matrix. For the William body and William opaque the expansion coefficient were investigated by the manufacturer [2.12], [2.13]. The values of the glassy matrix and the leucite crystal have been taken from literature [2.10], [2.11]. For this later component, they were derived from high temperature X-ray measurements. The authors have found an increase in CTE of leucite crystals above 400 °C due to the transformation of leucite from a tetragonal to a cubic form. It is known that tetragonal and cubic phases coexist at 400 °C and that only the cubic phase exists at 600 °C [2.12]. The transformation between tetragonal and cubic leucite is reversible and temperature dependent. A large mismatch of CTE occurs with the difference of expansion between the glassy matrix and the leucite particles. This mismatch causes residual stress in the glassy matrix when the glassy porcelain is cooled from the firing temperature [2.9].

The zone which shows a great interest to determine the residual stress, is the glassy ceramic coating. X-ray or neutron residual stress evaluation methods are particularly difficult to apply to such material, because it is multiphase. For that reason the stress tensor of each constituent will be triaxial ($\sigma_{33} \neq 0$), even if the macroscopic stresses remains biaxial ($\hat{\sigma}_{33} = 0$). To define the macro-stresses, the local stresses are therefore usually evaluated in all major phases of the material. However, in our case such method does no apply, because the glassy matrix does not diffract. A self-consistent micro-mechanical model will therefore be used to derive the macro-stresses from the values determined experimentally on the leucite crystal grains.

The "**self consistent micro-mechanical model"** has been used to describe the coupling between the different constituents. In a first approach, to evaluate the residual stress the following hypothesis have been introduced:

1. ***No plastic deformation of the leucite and the glassy matrix***
2. ***Isotropic behaviour of both phase***
3. ***In average, the shape of the grains is spherical***

In an isotropic medium, the tensor equations (or for $\underline{\underline{\sigma}}$ and $\underline{\underline{\varepsilon}}$) are thus greatly simplified. The stress and strain tensors can be decomposed into deviatoric and spherical parts.

$$\underline{\underline{\sigma}} = \begin{bmatrix} \sigma_{11} & \sigma_{12} & \sigma_{13} \\ \sigma_{21} & \sigma_{22} & \sigma_{23} \\ \sigma_{31} & \sigma_{32} & \sigma_{33} \end{bmatrix} = \underline{\underline{\mathrm{dev}}}\left(\underline{\underline{\sigma}}\right) + \frac{1}{3} \cdot \mathrm{tr}\left(\underline{\underline{\sigma}}\right) \cdot \underline{\underline{I}} \qquad \textit{Eq. 2.10}$$

$$\text{where } \underline{\underline{\mathrm{dev}}}\left(\underline{\underline{\sigma}}\right) = \begin{bmatrix} \sigma_{11} - \frac{1}{3}\sigma_{kk} & \sigma_{12} & \sigma_{13} \\ \sigma_{21} & \sigma_{22} - \frac{1}{3}\sigma_{kk} & \sigma_{23} \\ \sigma_{31} & \sigma_{32} & \sigma_{33} - \frac{1}{3}\sigma_{kk} \end{bmatrix} \qquad \textit{Eq. 2.11}$$

$$\underline{\underline{\varepsilon}} = \underline{\underline{\mathrm{dev}}}\left(\underline{\underline{\varepsilon}}\right) + \frac{1}{3} \cdot \mathrm{tr}\left(\underline{\underline{\varepsilon}}\right) \cdot \underline{\underline{I}} \qquad \textit{Eq. 2.12}$$

$$\mathrm{tr}\left(\underline{\underline{\sigma}}\right) = \sigma_{kk} = \sigma_{11} + \sigma_{22} + \sigma_{33} \qquad \textit{Eq. 2.13}$$

is the hydrostatic pressure which represents the mean pressure exiting at a given point of the material. In ductile materials (like metals), this pressure does not produce any plastic deformation. The deviatoric part, on the contrary, is directly related to plastic deformation.

The strain tensor can also be divided into elastic strains $\underline{\underline{e_e}}$ directly related to stress through Hooke's law and stress-free strains corresponding to the unstressed condition:

$$\underline{\underline{\varepsilon}} = \underline{\underline{\varepsilon_e}} + \underline{\underline{\varepsilon_f}} \qquad \textit{Eq. 2.14}$$

The deviatoric part of the stress-free strain tensor $\underline{\underline{\varepsilon_f}}$ fits generally the plastic deformation $\underline{\underline{\varepsilon_p}}$, while the spherical one corresponds to volume changes $\underline{\underline{\varepsilon_v}}$ induced by thermal expansions or phase transformations:

$$\underline{\underline{\varepsilon_f}} = \underline{\underline{\varepsilon_p}} + \underline{\underline{\varepsilon_v}}$$

Eq. 2.15

From a physical point of view, plastic deformation is produced by slips of a crystal submitted to shear. The shear stresses and the slip rates are relates by Smith law.

In cubic materials, a mean hydrostatic pressure does not result in crystal slips because it does not induce any shear stress. This is true even in the case of anisotropic crystals.

In our case, the volumic part is limited to the thermal expansions $\underline{\underline{\varepsilon_\theta}}$. Mathematically equations 2.14 and 2.15 come then to:

$$\underline{\underline{\varepsilon}} = \underline{\underline{\varepsilon_e}} + \underline{\underline{\varepsilon_p}} + \underline{\underline{\varepsilon_\theta}}$$

Eq. 2.16

The stress tensor components are linked to the elastic strains by Hooke's law:

$$\underline{\underline{\sigma}} = \underline{\underline{C}} \cdot \underline{\underline{\varepsilon_e}}$$

Eq. 2.17

where $\underline{\underline{C}}$ is the rank 4 compliance tensor (C_{ijkl}). In the case of isotropic materials, the components of this tensor only depend on Young's modulus E and Poisson's ratio ν: $C = f(E, \nu)$. For this kind of solids, the shear modulus μ and the compression modulus k are usually defined:

$$\mu = \frac{E}{2(1+\nu)}$$

Eq. 2.18

$$3k = \frac{E}{1-2\nu}$$

Eq. 2.19

The stress/strain relationship simplifies also to linear equations:

$$\mathrm{tr}\left(\underline{\underline{\sigma}}\right) = 3k \cdot \mathrm{tr}\left(\underline{\underline{\varepsilon}}\right)$$

$$\underline{\underline{\mathrm{dev}}}\left(\underline{\underline{\sigma}}\right) = 2\mu \cdot \underline{\underline{\mathrm{dev}}}\left(\underline{\underline{\varepsilon_e}}\right)$$

Eq. 2.20

2.5 Self consistent model

The model describes the coupling between the different constituents of the material. It is based on the solution of the inclusion problem first given by Eshelby [2.4]. Its equations become quite simple when the material is isotropic. In such approach, each grain is considered as a spherical inclusion embedded in a matrix owing the mean mechanical behaviour of the whole material.

The local mechanical properties of the elementary grain are characterised by the local stress and strain tensors:

$$\underline{\underline{s}}, \underline{\underline{e}} = \underline{\underline{e}}_e + \underline{\underline{e}}_p + \underline{\underline{e}}_q \qquad \textit{Eq. 2.21}$$

and local elastic constants: 2μ, 3k, E, ν.

The macro behaviour is characterised in the same way by:

$$\underline{\underline{\hat{\sigma}}}, \quad \underline{\underline{\hat{\varepsilon}}} = \underline{\underline{\hat{\varepsilon}}}_e + \underline{\underline{\hat{\varepsilon}}}_p + \underline{\underline{\hat{\varepsilon}}}_\theta \qquad \textit{Eq. 2.22}$$

$$2\hat{m}, \ 3\hat{k} \ \hat{E}, \hat{v}.$$

As it will be demonstrated further, the local elastic characteristics of the phases (E_{glass}, ν_{glass}, E_{leu}, ν_{leu}) and the macroscopic constants of the whole material $\hat{E}_{cer}, \ \hat{n}_{cer}$ are related. The self-consistent model will thus allow, either to evaluate the macroscopic characteristics of the material from the local ones (if the phase volume fractions are known), or to quantify the volume fractions (if all the elastic constants are defined).

The general equations, which describe the relation between the local and global mechanical properties of the material, are the following ones:

$$\mathrm{tr}\underline{\underline{\sigma}} = \mathrm{T} \cdot \mathrm{tr}\hat{\sigma} + \mathrm{T} \cdot 3\hat{k} \cdot \mathrm{T}(\hat{a} - 1) \cdot [\mathrm{tr}(\underline{\underline{\varepsilon_f}}) - \mathrm{tr}(\hat{\varepsilon}_f)] \qquad \textit{Eq. 2.23}$$

$$\underline{\underline{\mathrm{dev}}}(\underline{\sigma}) = \mathrm{D} \cdot \underline{\underline{\mathrm{dev}}}(\hat{\sigma}) + 2\hat{\mu} \cdot \mathrm{D}(\hat{b} - 1) \cdot [\underline{\underline{\mathrm{dev}}}(\underline{\underline{\varepsilon_f}}) - \underline{\underline{\mathrm{dev}}}(\hat{\varepsilon}_f)] \qquad \textit{Eq. 2.24}$$

$$\text{where } T = \frac{k}{\hat{k} + \hat{a}\left(k - \hat{k}\right)} \qquad \textit{Eq. 2.25}$$

$$\text{and} \quad D = \frac{\mu}{\hat{\mu} + \hat{b}(\mu - \hat{\mu})} \qquad \textit{Eq. 2.26}$$

$$\text{with } \hat{a} = \frac{1}{3} \cdot \frac{1 + \hat{v}}{1 - \hat{v}} \qquad \textit{Eq. 2.27}$$

$$\text{and } \hat{b} = \frac{2}{15} \cdot \frac{4 - 5\hat{v}}{1 - \hat{v}} \qquad \textit{Eq. 2.28}$$

The leucite grains and the glassy matrix do not deform plastically. For that reason, in our case, the stress-free-strains reduce to thermal strains which are purely spherical.

2.5.1 Pure elastic behaviour of the material

If the case of pure elastic behaviour of the material, equations 24 and 25 simplify to:

$$\begin{aligned} &\underline{\underline{\sigma}}_{kk} = T\hat{\sigma}_{kk} \\ &\underline{\underline{\mathrm{dev}\,\sigma}} = D\,\underline{\underline{\mathrm{dev}\,\hat{\sigma}}} \end{aligned} \qquad \textit{Eq. 2.29}$$

Such equation can be written for both phases:

$$\begin{cases} \sigma_{kk}^{leu} = T^{leu}\hat{\sigma}_{kk} \\ \sigma_{kk}^{glass} = T^{glass}\hat{\sigma}_{kk} \end{cases} \qquad \textit{Eq. 2.30}$$

$$\begin{cases} \underline{\underline{dev}}\,\underline{\underline{s}}^{leu} = D^{leu}\,\underline{\underline{dev}}\,\underline{\underline{\hat{s}}} \\ \underline{\underline{dev}}\,\underline{\underline{s}}^{glass} = D^{glass}\,\underline{\underline{dev}}\,\underline{\underline{\hat{s}}} \end{cases} \qquad \textit{Eq. 2.31}$$

The stresses are balanced over all the constituents of the material:

$$\begin{aligned} &\underline{\underline{\hat{\sigma}}} = (y^{leu} \cdot \underline{\underline{\sigma}}^{leu} + y^{glass} \cdot \underline{\underline{\sigma}}^{glass}) \\ &\underline{\underline{\hat{\sigma}_{kk}}} = (y^{leu} \cdot \underline{\underline{\sigma}}_{kk}^{leu} + y^{glass} \cdot \underline{\underline{\sigma}}_{kk}^{glass}) \\ &\underline{\underline{\mathrm{dev}\,\hat{\sigma}}} = (y^{leu} \cdot \underline{\underline{\mathrm{dev}\,\sigma}}^{leu} + y^{glass} \cdot \underline{\underline{\mathrm{dev}\,\sigma}}^{glass}) \end{aligned} \qquad \textit{Eq. 2.32}$$

where y^{leuc} is the volume fraction of leucite,

and $y^{glass}=1-y^{leuc}$ is the volume fraction of the glassy matrix.

This leads to the following implicit equations of homogenisation for the elastic constants:

$$y^{leu} \cdot T^{leu} + y^{glass} \cdot T^{glass} = 1 \qquad \textit{Eq. 2.33}$$

$$y^{leu} \cdot D^{leu} + y^{glass} \cdot D^{glass} = 1 \qquad \textit{Eq. 2.34}$$

In our case, the elastic properties of the glassy matrix (E, ν) and those of the whole ceramic layer are well characterised, but the values for the leucite are unknown. The volume fractions of the phases, also, are not defined, but they will be derived further from the modelling of the thermal behaviour of the material. These two equations will thus allow evaluating the elastic constants of the leucite grains.

2.5.2 Thermal expansion of the material

In the case of pure homogeneous thermal expansion (or contraction) of the material the stress-free strains reduce to isotropic spherical tensors and no macro-stress does exist:

$$\begin{cases} \underline{\underline{\varepsilon_L}} = \alpha \cdot \underline{\underline{I}} \cdot \Delta\theta \\ \underline{\underline{\hat{\varepsilon}_L}} = \hat{\alpha} \cdot \underline{\underline{I}} \cdot \Delta\theta \end{cases} \qquad \textit{Eq. 2.35}$$

$$\begin{cases} \mathrm{tr}(\underline{\underline{\varepsilon_f}}) = 3\alpha \cdot \Delta\theta \\ \mathrm{tr}(\underline{\underline{\hat{\varepsilon}_f}}) = 3\hat{\alpha} \cdot \Delta\theta \end{cases} \qquad \textit{Eq. 2.36}$$

$$\begin{cases} \underline{\underline{\mathrm{dev}}}(\underline{\underline{\varepsilon_f}}) = \underline{\underline{0}} \\ \underline{\underline{\mathrm{dev}}}(\underline{\underline{\hat{\varepsilon}_f}}) = \underline{\underline{0}} \end{cases} \qquad \textit{Eq. 2.37}$$

where α is the local coefficient of thermal expansion and $\hat{a}$ is the global coefficient of thermal expansion.

The equations for both phases become therefore:

Leucite
$$\begin{aligned} \varepsilon_{kk}^{leu} &= T^{leu} \cdot \hat{\sigma}_{kk} + T^{leu} 3\hat{k}(\hat{a}-1) \cdot \left(\sigma_{kk}^{leu} - \hat{\sigma}_{kk}\right) \\ \sigma_{kk}^{leu} &= T^{leu} \cdot \hat{\sigma}_{kk} + T^{leu} 3\hat{k}(\hat{a}-1) \cdot \left(3\alpha^{leu}\Delta\theta - 3\hat{\alpha}\Delta\theta\right) \end{aligned}$$
Eq. 2.38

Glass
$$\sigma_{kk}^{glass} = T^{glass} \cdot \hat{\sigma}_{kk} + T^{glass} 3\hat{k}(\hat{a}-1) \cdot \left(3\alpha^{glass}\Delta\theta - 3\hat{\alpha}\Delta\theta\right)$$
Eq. 2.39

where $\hat{\sigma}_{kk} = y \cdot \sigma^{leu} \cdot \sigma_{kk}^{leu} + \underbrace{y^{glass}}_{1-y^{leu}} \cdot \sigma_{kk}^{glass}$

These expressions simplify to:

$$\hat{\alpha} = y^{leu} \cdot T^{leu} \alpha^{leu} + y^{glass} \cdot T^{glass} \alpha^{glass}$$
Eq. 2.40

In our case, all the coefficients of thermal expansion are known. This relationship can thus be used to evaluate the volume fractions of the major phases of the material, i.e. the glassy matrix and the leucite. A simple formula is therefore deduced from equation 2.33:

$$\hat{\alpha} = \left(1 - y^{glas} \cdot T^{glass}\right) \alpha^{leu} + y^{glas} \cdot T^{glass} \alpha^{glass}$$
Eq. 2.41

$$\hat{\alpha} - \alpha^{leuc} = y^{glass} \cdot T^{glass} \left(\alpha^{glass} - \alpha^{leu}\right)$$
Eq. 2.42

$$y^{glass} = \frac{\hat{\alpha} - \alpha^{leu}}{T^{glass}\left(\alpha^{glass} - \alpha^{leu}\right)}$$
Eq. 2.43

The volume fractions of the phases are now defined and the elastic constants of the leucite grains can be computed through equations 2.33 and 2.34.

2.5.3 Application of the model to diffraction measurements

Due to the plane symmetry of our sample, the macroscopic stress state is biaxial.

$$\hat{\sigma}_{13} = \hat{\sigma}_{23} = \hat{\sigma}_{33} = 0$$
Eq. 2.44

$$[\hat{\sigma}] = \begin{bmatrix} \hat{\sigma}_{11} & \hat{\sigma}_{12} & 0 \\ \hat{\sigma}_{21} & \hat{\sigma}_{22} & 0 \\ 0 & 0 & 0 \end{bmatrix}$$
Eq. 2.45

in fact, no shear stress exits on the free surface. Moreover, as it has already pointed out, the stress and strains are constant over a large area of the sample surface. Thus, applying the stress equilibrium conditions:

$$\begin{cases} \dfrac{\partial \hat{\sigma}_{11}}{\partial x} + \dfrac{\partial \hat{\sigma}_{21}}{\partial y} + \dfrac{\partial \hat{\sigma}_{13}}{\partial z} = 0 \\ \dfrac{\partial \hat{\sigma}_{21}}{\partial x} + \dfrac{\partial \hat{\sigma}_{22}}{\partial y} + \dfrac{\partial \hat{\sigma}_{23}}{\partial z} = 0 \\ \dfrac{\partial \hat{\sigma}_{31}}{\partial x} + \dfrac{\partial \hat{\sigma}_{23}}{\partial y} + \dfrac{\partial \hat{\sigma}_{33}}{\partial z} = 0 \end{cases} \qquad \textit{Eq. 2.46}$$

$$\begin{cases} \dfrac{\partial \hat{\sigma}_{13}}{\partial z} = \dfrac{\partial \hat{\sigma}_{23}}{\partial z} = \dfrac{\partial \hat{\sigma}_{33}}{\partial z} = 0 \Rightarrow \hat{\sigma}_{13} = \hat{\sigma}_{23} = \hat{\sigma}_{33} = 0 \ \ \forall z \end{cases} \qquad \textit{Eq. 2.47}$$

Since the stress state is biaxial at the free surface and no gradients exist in the depth, the macro-stresses are to remain biaxial in the analysed layers. However, X-ray and neutron diffraction does not analyse the whole material but only the crystalline leucite phase. In this constituent the normal stress σ_{33} can not be neglected, even if the macroscopic value is zero. This is due to the thermal expansion mismatch between the leucite phase and the glassy matrix.

In such configuration the well-known $\sin^2\psi$ law becomes:

$$\varepsilon_{e\phi\psi} = \left(\frac{1+\nu}{E}\right)\cdot(\sigma_\phi - \sigma_{33})\sin^2\psi + \left(\frac{\nu}{E}\right)\cdot\left(\sigma_{11} + \sigma_{22} + \sigma_{33}\right) + \left(\frac{1+\nu}{E}\right)\cdot\sigma_{33} \qquad \textit{Eq. 2.48}$$

This equation leads to a linear plot of $\varepsilon_{e\phi\psi}\text{vs.}\sin^2\psi$ for a fixed ϕ direction and different ψ angles. The slope of the resulting straight line allows evaluating $(s_f - s_{33})$.

Let us now consider the deviatoric part of the local stress tensor (leucite phase):

$$\underline{\underline{S}} = \underline{\underline{\mathrm{dev}}}(\underline{\underline{\sigma}}) \qquad \textit{Eq. 2.49}$$

$$\begin{cases} \sigma_\phi = S_\phi + \dfrac{1}{3}\sigma_{kk} \\ \sigma_{33} = S_{33} + \dfrac{1}{3}\sigma_{kk} \end{cases} \Rightarrow \sigma_\phi - \sigma_{33} = S_\phi - S_{33} \qquad \textit{Eq. 2.50}$$

As it has already been pointed out, no plastic deformation occurs in the ceramic. For that reason the deviatoric part of the stress-free strains are zero tensors for both the leucite and the global material. Equation 2.24 leads thus to:

$$\begin{cases} \underline{\underline{\mathrm{S}}}^{\mathrm{leu}} = \mathrm{D}^{\mathrm{leu}} \cdot \underline{\underline{\hat{\mathrm{S}}}} \\ \mathrm{S}_{\phi}^{\mathrm{leu}} = \mathrm{D}^{\mathrm{leu}} \cdot \hat{\mathrm{S}}_{\phi} \quad \Rightarrow \sigma_{\phi}^{\mathrm{leu}} - \sigma_{33}^{\mathrm{leu}} = \mathrm{D}^{\mathrm{leu}} (\hat{\sigma}_{\phi} - \hat{\sigma}_{33}) \\ \mathrm{S}_{33}^{\mathrm{leu}} = \mathrm{D}^{\mathrm{leu}} \cdot \hat{\mathrm{S}}_{33} \end{cases} \qquad \textit{Eq. 2.51}$$

since $\hat{s}_{33} = 0$ it comes

$$\hat{\sigma}_{\phi} = \frac{1}{\mathrm{D}^{\mathrm{leu}}}\left(\sigma_{\phi}^{\mathrm{leu}} - \sigma_{33}^{\mathrm{leu}}\right) \qquad \textit{Eq. 2.52}$$

The macro-stress components are just proportional to the measured values but the mean normal stress of the leucite grains remains still undefined. This stress can be estimated using the global equation for the spherical parts:

$$\sigma_{11}^{\mathrm{leu}} + \sigma_{22}^{\mathrm{leu}} + \sigma_{33}^{\mathrm{leu}} = (\hat{\sigma}_{11} + \hat{\sigma}_{22})\mathrm{T}^{\mathrm{leu}} + \mathrm{T}^{\mathrm{leu}} 3\hat{\mathrm{k}}(\hat{\mathrm{a}} - 1)(\alpha^{\mathrm{leu}} - \hat{\alpha})3\Delta\theta \qquad \textit{Eq. 2.53}$$

$$\left(\sigma_{11}^{\mathrm{leu}} - \sigma_{33}^{\mathrm{leu}}\right) + \left(\sigma_{22}^{\mathrm{leu}} - \sigma_{33}^{\mathrm{leu}}\right) + \underbrace{\left(\sigma_{33}^{\mathrm{leu}} - \sigma_{33}^{\mathrm{leu}}\right)}_{0} + 3\sigma_{33}^{\mathrm{leu}} = (\hat{\sigma}_{11} + \hat{\sigma}_{22})\mathrm{T}^{\mathrm{leu}} + \mathrm{T}^{\mathrm{leu}} 3\hat{\mathrm{k}}(\hat{\mathrm{a}} - 1)(\alpha^{\mathrm{leu}} - \hat{\alpha})3\Delta\theta$$

Eq. 2.54

$$\sigma_{33}^{\mathrm{leu}} = \frac{1}{3}\mathrm{T}^{\mathrm{leu}}(\hat{\sigma}_{11} + \hat{\sigma}_{22}) - \frac{1}{3}\left[\left(\sigma_{11}^{\mathrm{leu}} - \sigma_{33}^{\mathrm{leu}}\right) + \left(\sigma_{22}^{\mathrm{leu}} - \sigma_{33}^{\mathrm{leu}}\right)\right] + \mathrm{T}^{\mathrm{leu}} 3\hat{\mathrm{k}}(\hat{\mathrm{a}} - 1)(\alpha^{\mathrm{leu}} - \hat{\alpha})\Delta\theta$$

Eq. 2.55

This last expression needs just to know the change of temperature $\Delta\theta$. Due to some recovery of the glass/leucite mixture $\Delta\theta$ does not correspond to the interval between the melting point and the room temperature but is defined by the recovery threshold (about the half of the melting point): $\Delta\theta = -\left[\frac{605 + 273}{2} - 293\right] =$ -146 °K

2.5.3.1 Calculation of theoretical value of the stress component s_{33}

As we have pointed out, the general equations, which describe the relation between the local and global mechanical properties of the material, are the following ones: $T = \frac{k}{\hat{k} + \hat{a}\left(k - \hat{k}\right)}$ and

$$D = \frac{\mu}{\hat{\mu} + \hat{b}(\mu - \hat{\mu})}$$

In the flow-chart (Figure 2.3) all the mechanical and physical parameters of the three constituent sample are resumed:

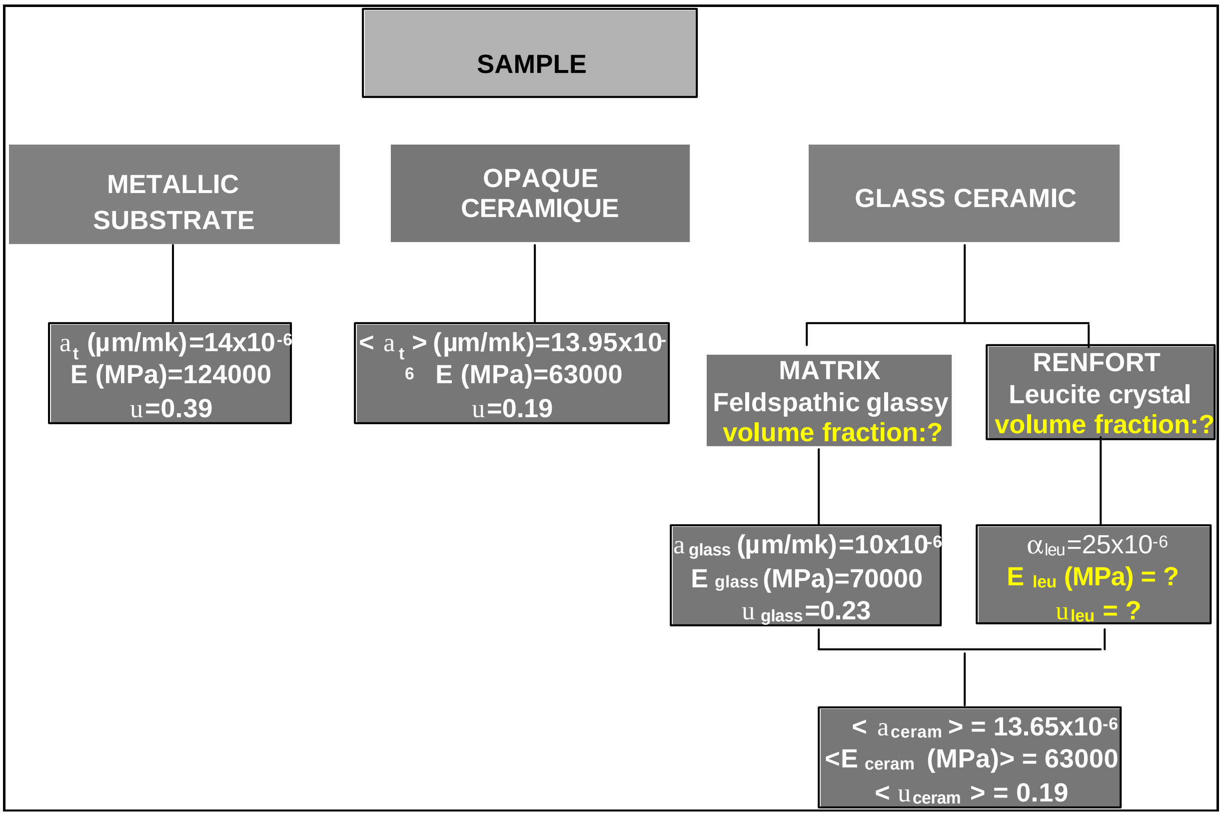

Figure 2.3: Mechanical and physical properties of constituent sample.

Taking the equation $\hat{a} = \frac{1}{3} \cdot \frac{1+\hat{\nu}}{1-\hat{\nu}}$ and $\hat{b} = \frac{2}{15} \cdot \frac{4-5\hat{\nu}}{1-\hat{\nu}}$ and substituting the value $\hat{\nu}_{\mathrm{CERAM}}=\hat{\nu}=0.19$ we obtain: $\hat{a} = 0.4897$ and $\hat{b} = 0.5021$ and

then $\hat{\mu}_{\mathrm{ceram}} = \frac{E}{2\left(1+\hat{\nu}_{\mathrm{cerem}}\right)} = 33871$

$$\hat{k}_{ceram} = \frac{E}{3(1-2\hat{\nu}_{ceram})} = 26471$$

Now we can calculate: $T^{leu} = \frac{k}{\hat{k} + \hat{a}(k - \hat{k})} = 0.74$ and $D^{leu} = \frac{\mu}{\hat{\mu} + \hat{b}(\mu - \hat{\mu})} = 0.9259$

$T^{glass} = \frac{k}{\hat{k} + \hat{a}(k - \hat{k})} = 1.124$ and $D^{glass} = \frac{\mu}{\hat{\mu} + \hat{b}(\mu - \hat{\mu})} = 1.0360$

and consequently: $y^{glass} = \frac{\hat{\alpha}_{cer} - \alpha^{leu}}{T^{glass}(\alpha^{glass} - \alpha^{leu})} = 0.6732$ and finally

y^{leuc}=1- y^{glass} = 0.3268 is the volume fraction of leucite, y^{glass} is the volume fraction of the glassy matrix.

This leads to the following implicit equations of homogenisation for the elastic constants:

$$y^{leu} \cdot T^{leu} + y^{glass} \cdot T^{glass} = 1$$

$$y^{leu} \cdot D^{leu} + y^{glass} \cdot D^{glass} = 1$$

In our case, we know the elastic properties of the glassy matrix (E, ν) and those of the whole ceramic layer, but the values for the leucite are unknown.

For the preview calculations, the volume fractions of the two phases are defined so we can obtain from $\hat{\sigma}_{11} = \frac{1}{D^{leu}}\left(\sigma_{11}^{leu} - \sigma_{33}^{leu}\right)$ and $\hat{\sigma}_{22} = \frac{1}{D^{leu}}\left(\sigma_{22}^{leu} - \sigma_{33}^{leu}\right)$:

$$\sigma_{33}^{leu} = \frac{1}{3}T^{leu}\left(\hat{\sigma}_{11} + \hat{\sigma}_{22}\right) - \frac{1}{3}\left[\left(\sigma_{11}^{leu} - \sigma_{33}^{leu}\right) + \left(\sigma_{22}^{leu} - \sigma_{33}^{leu}\right)\right] + T^{leu}3\hat{k}(\hat{a}-1)\left(\alpha^{leu} - \hat{\alpha}\right)\Delta\theta$$

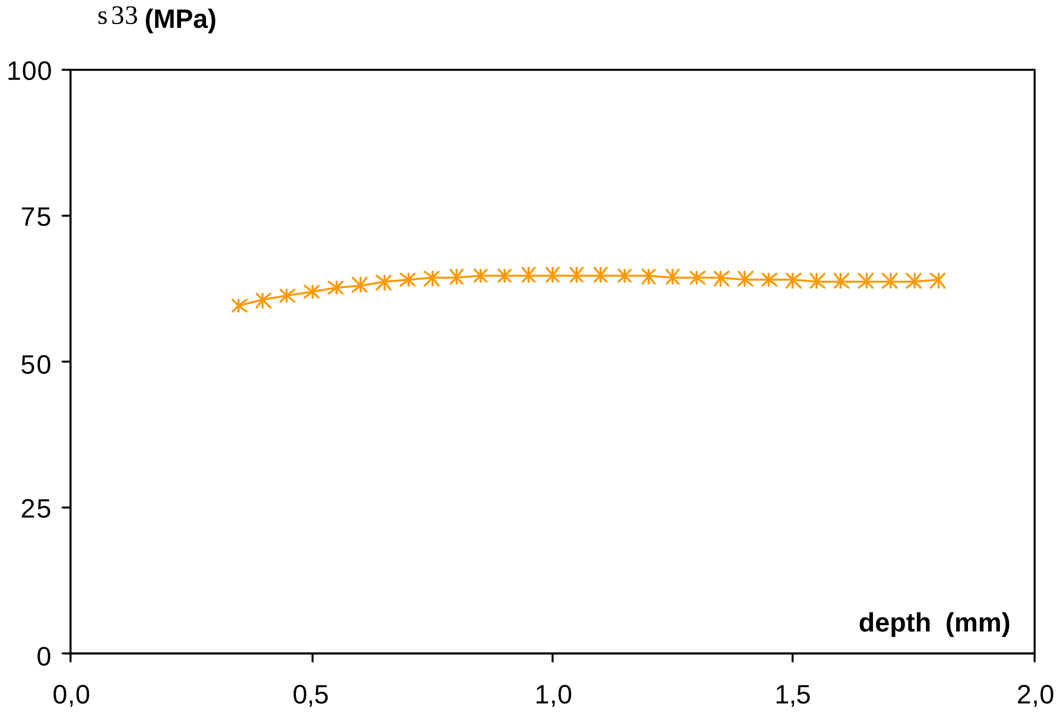

Figure 2.4: Theoretical value of the stress component s_{33}.

2.6 Theoretical prediction of residual stresses due to the thermal mismatch between the ceramic coating and the metal substrate

The sample consists in three different layers as in the Figure 2.5:

The calculations assume flat plane symmetry of the sample and that the longitudinal, transverse and normal directions are the principal directions of stress and strain. The stresses are biaxial. No plastic deformation occurs during cooling. The different layers of the sample exhibit linear isotropic elastic behaviour.

$$\underline{\underline{\hat{\sigma}}} = \begin{bmatrix} \hat{\sigma}_{11} & 0 & 0 \\ 0 & \hat{\sigma}_{22} & 0 \\ 0 & 0 & 0 \end{bmatrix} \qquad \text{Eq. 2.56}$$

and for the strain $$\underline{\underline{\hat{\varepsilon}}} = \begin{bmatrix} \hat{\varepsilon}_{11} & 0 & 0 \\ 0 & \hat{\varepsilon}_{22} & 0 \\ 0 & 0 & \hat{\varepsilon}_{33} \end{bmatrix} \qquad \text{Eq. 2.57}$$

Applying the equations of compatibility:

$$\begin{cases} \varepsilon_{11} = A_{11}z + B_{11} \\ \varepsilon_{22} = A_{22}z + B_{22} \end{cases} \qquad \text{Eq. 2.58}$$

The strain components are decomposed into elastic and thermal parts:

$$\begin{matrix} e_{11} = e_{e11} + e_{q11} \\ e_{11} = e_{e11} + e_{q11} \end{matrix} \quad \text{where} \quad \begin{matrix} \varepsilon_{\theta 11} = (\alpha - < \alpha >)\Delta\theta \\ \varepsilon_{\theta 11} = (\alpha - < \alpha >)\Delta\theta \end{matrix} \qquad \text{Eq. 2.59}$$

where $< \alpha >= \int_0^h \alpha(z)\,dz$ **.**

From equations 2.58 and 2.59 we deduce:

$$\begin{cases} \varepsilon_{e11} = A_{11}x_3 + B_{11} - (\alpha - < \alpha >)\Delta\theta \\ \varepsilon_{e22} = A_{22}x_3 + B_{22} - (\alpha - < \alpha >)\Delta\theta \end{cases} \qquad \textit{Eq. 2.60}$$

In the plane stress condition Hooke's law is expressed by following equations

$$\begin{cases} \varepsilon_{e11} = \left(\dfrac{1+\nu}{E}\right)\cdot\sigma_{11} - \left(\dfrac{\nu}{E}\right)\cdot(\sigma_{11} + \sigma_{22}) \\ \varepsilon_{e22} = \left(\dfrac{1+\nu}{E}\right)\cdot\sigma_{22} - \left(\dfrac{\nu}{E}\right)\cdot(\sigma_{11} + \sigma_{22}) \end{cases} \qquad \textit{Eq. 2.61}$$

$$\begin{cases} E\varepsilon_{e11} = \sigma_{11} - \nu\sigma_{22} \\ E\varepsilon_{e22} = -\nu\sigma_{11} + \sigma_{22} \end{cases} \qquad \textit{Eq. 2.62}$$

$$\begin{aligned} \Delta &= \begin{vmatrix} 1 & -\nu \\ -\nu & 1 \end{vmatrix} = 1-\nu^2 \\ \Delta_1 &= \begin{vmatrix} E\varepsilon_{e11} & -\nu \\ E\varepsilon_{e22} & 1 \end{vmatrix} = E(\varepsilon_{e11} + \nu\varepsilon_{e22}) \end{aligned} \qquad \textit{Eq. 2.63}$$

$$\begin{cases} \sigma_{11} = \left(\dfrac{E}{1-\nu^2}\right)\cdot(\varepsilon_{e11} + \nu\varepsilon_{e22}) \\ \sigma_{22} = \left(\dfrac{E}{1-\nu^2}\right)\cdot(\varepsilon_{e22} + \nu\varepsilon_{e11}) \end{cases} \qquad \textit{Eq. 2.64}$$

$$\begin{cases} \sigma_{11} = \left(\dfrac{E}{1-\nu^2}\right)\cdot\left[(A_{11} + \nu A_{22})z + (B_{11} + \nu B_{22}) - (1+\nu)(\alpha - < \alpha >)\Delta\theta\right] \\ \sigma_{22} = \left(\dfrac{E}{1-\nu^2}\right)\cdot\left[\nu(A_{11} + A_{22})z + (\nu B_{11} + B_{22}) - (1+\nu)(\alpha - < \alpha >)\Delta\theta\right] \end{cases} \qquad \textit{Eq. 2.65}$$

calling:

$$C_{11} = \frac{E(A_{11} + \nu A_{22})}{1-\nu^2}$$
$$D_{11} = \frac{E(B_{11} + \nu B_{22})}{1-\nu^2} \qquad \textit{Eq. 2.66}$$

it becomes:

$$\begin{cases} \sigma_{11} = C_{11}x_3 + D_{11} - \dfrac{E}{1-\nu}(\alpha - <\alpha>)\Delta\theta \\ \sigma_{22} = C_{22}x_3 + D_{22} - \dfrac{E}{1-\nu}(\alpha - <\alpha>)\Delta\theta \end{cases} \qquad \textit{Eq. 2.67}$$

The four constants C_{11}, C_{22}, D_{11}, D_{22} are determined by the equilibrium condition of the whole body:

- **Equilibrium of forces:**

$\int_{z=0}^{h} \hat{\sigma}_{11}(z)dz = 0$ it leads to following condition

$$C_{11}\frac{h^2}{2} + D_{11}h - \Delta\theta\int_0^h \frac{E}{1-\nu}(\alpha - <\alpha>)dz = 0$$

$$\Rightarrow \frac{h^2}{2}C_{11} + hD_{11} = \Delta\theta\int_0^h \frac{E}{1-\nu}(\alpha(z) - <\alpha>)dz \qquad \textit{Eq. 2.68}$$

- Equilibrium of momenta:

$\int_{z=0}^{h} z\sigma_{11}(z)dz = 0$ it leads to following condition

$$\frac{h^3}{3}C_{11} + \frac{h^2}{2}D_{11} = \Delta\theta\int_0^h z\frac{E}{1-\nu}(\alpha(z) - <\alpha>)dz \qquad \textit{Eq. 2.69}$$

To summarise:

$$\begin{cases} \dfrac{h^2}{2}C_{11} + hD_{11} = \Delta\theta\displaystyle\int_0^h \frac{E}{1-\nu}(\alpha(z) - <\alpha>)dz \\ \dfrac{h^3}{3}C_{11} + \dfrac{h^2}{2}D_{11} = \Delta\theta\displaystyle\int_0^h z\frac{E}{1-\nu}(\alpha(z) - <\alpha>)dz \end{cases}$$

Eq. 2.70

The equations are exactly the same for the second direction thus leading to:

$$\begin{cases} C_{22} = C_{11} \\ D_{22} = D_{11} \end{cases}$$

Eq. 2.71

Calculated residual stresses in the three zone of sample (Figure 2.5), due to the thermal mismatch between the ceramic coating and the metal substrate, are shown in figure 2.6.

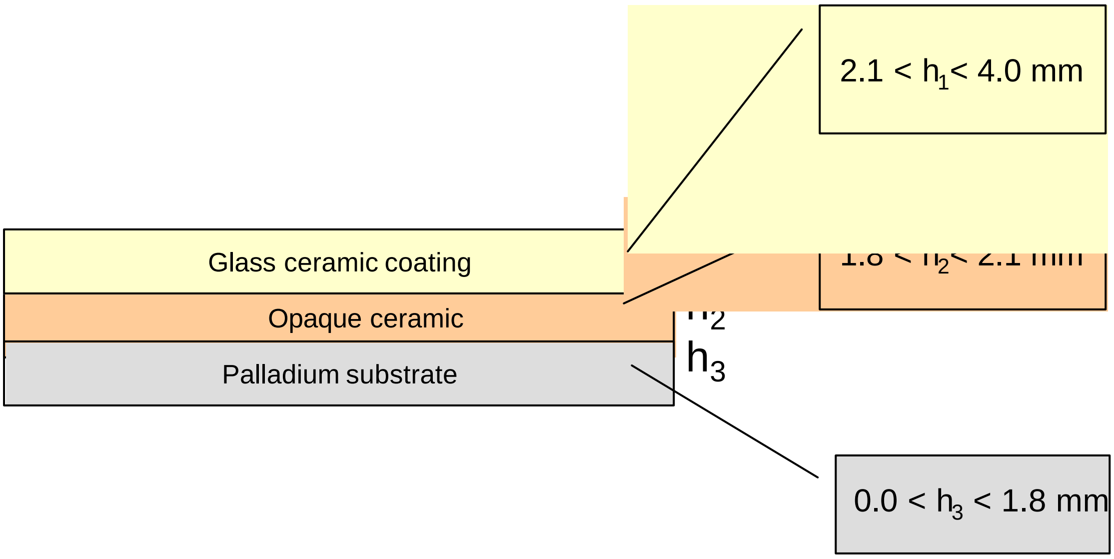

Figure 2.5: Sample S1 and its studied zone.

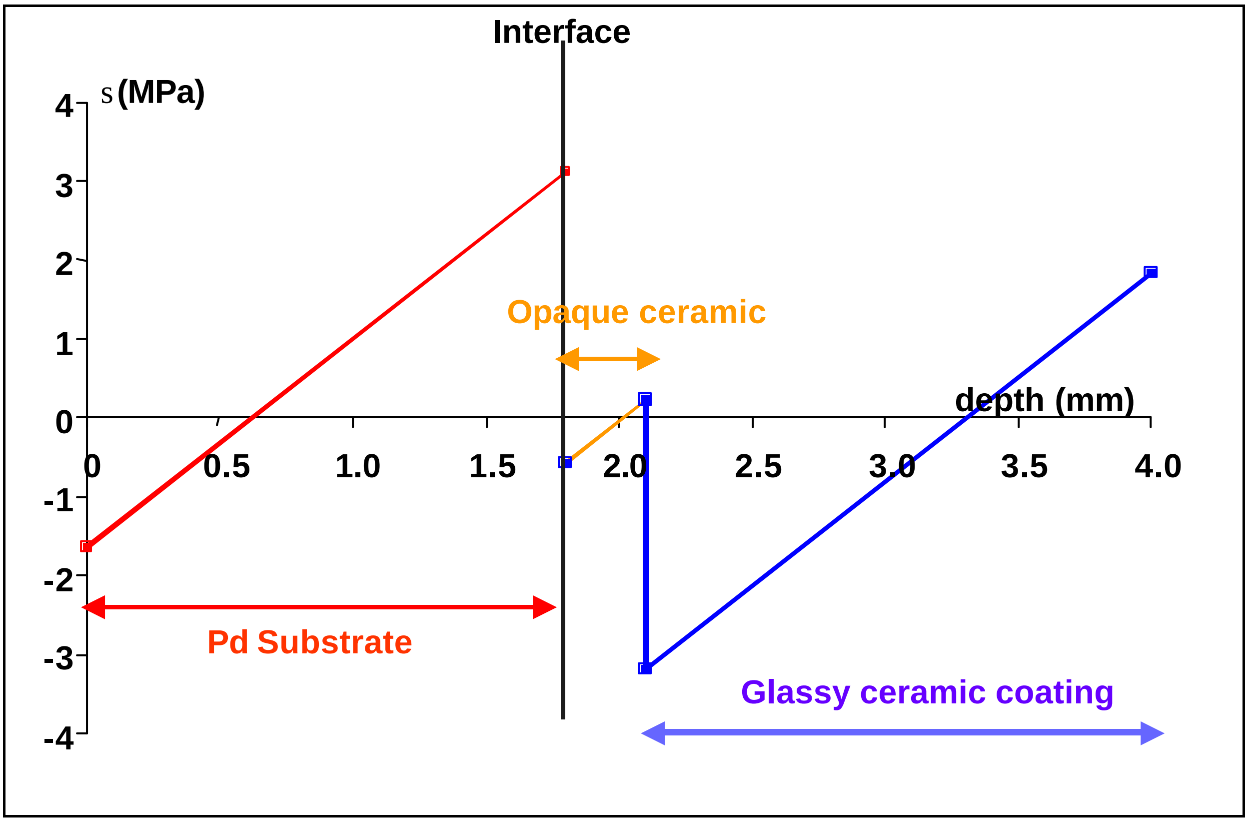

Figure 2.6: Residual stresses due to the thermal mismatch between the ceramic coating and the metal substrate.

References

[2.1] Noyan IC, Cohen JB, Editors. Residual stresses. Stuttgart: Springer-Verlag (1987).

[2.2] Voigt W. *Lehrbuch für Kristallphysik*, Teubner, Berlin, (1928) 962-967.

[2.3] Reuss A. *Z. Ang. Math. Mech.*, 9 (1929), 49-51.

[2.4] Eshelby J.D. The determination of the elastic field of an ellipsoidal inclusion and related problems. *Proc. Of the royal society London*, 241A (1957), 376-396.

[2.5] Kröner E. *Z. für Physik*, 151 (1958), 504-518.

[2.6] Kneer G.: Dissertation, Clausthal, (1964).

[2.7] Morris P.R. *Int. J. Eng. Sci.*, 8 (1970), 49-61.

[2.8] Sprauel J.M., Castex L., *EPDIC 1*, Materials Science Forum. 79-82 (1991), 143-152.

[2.9] Metalor® Data sheet.

[2.10] O'Brien WJ, Dental Materials and Their Selection, 2nd ed., 1997 edited by O'Brien WJ and published by Quintessence Publishing.

[2.11] Kon M et al., Effect of leucite crystals on the strength of glassy porcelain, J Dent. Mater. 13(2): 138-147, 1994.

[2.12] Whitlock RP, Tesk JA, Widera, GEO, Holmes A. and Parry EE: Consideration of some factors influencing compatibility of dental porcelains and alloys. Part I. Thermo-physical properties. pp. 273-282. In Proc. 4th Int. Precious Metals Conference, Toronto, June 1980. Willowdale, Ontario: Pergamon Press Canada, April 1981.

[2.13] Williams® international Data sheet.

CHAPTER 3

THE METHOD

3.1 Introduction

The study of residual stress on a Porcelain-Fused to Metal (PFM) on casted alloy substrate by different techniques, offer great interest in dental applications. To evaluate the mechanical behaviour of the sample at the metal/ceramic interface different non-destructive analyses of the residual stresses in leucite coating and palladium alloy substrate have been carried out.

A careful processing of the experimental data is however needed in zones very difficult to analyse due to physical phenomena (absorption for high-energy synchrotron radiation and dispersion of wavelength for neutron diffraction).

It is well known that the stress profiles at the surface and the interfaces of multi-layer samples are difficult to analyse. In neutron measurements, it is due to great parasitic peak shifts which are obtained in the measurements and for synchrotron radiation measurement it is linked to a strong absorption of the radiation in the material.

In this chapter, we will introduce an innovative approach to solve these problems. This approach will allow evaluating the residual stresses at the surface, in the bulk of materials and at interfaces, by different diffraction techniques.

Classical X-ray diffraction (XRD) have been employed to evaluate the stress state at the surface of the palladium substrate just before the thermal process induced by fusion of the coating onto it.

Chemical etching X-ray diffraction measurements have been carried out to analyse the near surface in-depth stress profiles and therefore to have a reference for the synchrotron radiation measurements.

Furthermore, to obtain internal and through surface residual strain data from which the in-depth residual stress profiles have been derived, **neutron diffraction measurements** have been carried out in both the palladium substrate and the glass-ceramic coating.

High-Energy Synchrotron Radiation measurements (HESR) have been done for the analysis of the superficial layers of the substrate (the first 80 µm) and of course the bulk of the coating and at the metal/ceramic interface zone.

In our work, a new program has been developed for the simulation of synchrotron radiation instruments. A simulation program already written in a previous study has also been used to describe the neutron spectrometers.

In this chapters two principals aims have been focused on:

- Recall to the principal information of the existing neutron spectrometer program and
- Introduction to the new simulation programme developed for the synchrotron radiation spectrometer.

3.2 Simulation of the two axis neutron spectrometer

It is well known that near surface neutron measurements and experiments performed at the interface between two different materials are difficult to analyse, as in our case. It happens because of great parasitic peak shifts which are obtained in this kind of condition.

Anyway, interface and near surface measurements are in general of great interest for the engineers, since the cracks are often initiated from these zones. A numerical simulation of the whole two-axis neutron spectrometer has been developed [3.1] to correct these systematic errors (Figure 3.1). This program allows also to optimise the experimental conditions and to define precisely the true volume of the neutron gauge.

The simulation program accounts for all the major components of the neutron spectrometer: the characteristics of the neutron guide or tube, the monochromator, up to hundred primary and secondary slits, the detector. An integrated feature oriented CAD drawing module defines the sample. It allows the description of very sophisticated specimens. The software accounts for the horizontal and vertical divergence of the incident and diffracted beams, for the local conditions of diffraction in the monochromator and the sample, and for the absorption by the monochromator and the sample.

The simulation program first computes the distribution of intensity and wavelength across the incident beam. The precise shape and size of the probe volume is then calculated. The intersection between this neutron probe and the sample is also computed, thus defining the diffracting volume. A theoretical diffraction peak is finally calculated through a Monte Carlo simulation method. The whole simulation program allows thus to optimise the experimental conditions and to predict all parasitic shifts of the diffraction peak. This approach has already been tested on other neutron experiments [3.2],[3.3].

It is very important to note that the depth affected by the stresses remains low in comparison to the size of the neutron beam. Therefore, it becomes necessary to localise precisely the true position of the neutron gauge inside the sample. In other terms, we have carried out a measurement realising a precise strain scanning across the studied surface. Consequently, the true position of the neutron gauge volume is then derived from the evolution of the diffracted intensity versus the scanned depth. The reliability of this method is, in the case of neutron diffraction measurements, better than 0.05 mm.

As it has already been pointed out, parasitic shifts of the diffraction peaks arise when the neutron gauge volume is not entirely immersed in the studied sample. Such impediment is particularly important in the case of near surface measurements.

Evaluation of the stress profiles in the palladium alloy substrate (**S1 sample**) is thus particularly difficult due to the small thickness of the sample. In fact, to obtain an acceptable diffracted intensity, the neutron gauge volume cannot be less than a few tens of mm^3. Under such condition, the neutron probe is never completely immersed in the analysed material.

The residual stress gradients are bigger than the neutron probe at the interfaces. In these conditions, a very precise scanning near the interface has to be imposed to obtain precise measurements. It is also necessary to localise precisely the neutron probe and his diffracting part. This has been achieved through the modelling of the neutron spectrometer and the synchrotron instruments.

Working at the interface, it is necessary to take different directions for evaluating all the tensor components of the residual stresses. Moreover, the lattice parameters of two materials are very different. In fact, the lattice parameter of the Cubic Face Centred palladium substrate is 0.395 nm and for the tetragonal leucite the lattice constants are a= b= 1.309 nm c= 1.375 nm. For this reason, we have not realised our measurements with the same instrumentation due to a big difference between the lattice parameters. For the ceramic great wavelength are required (> 0.4 nm). As we have already pointed out, it is necessary to define precisely the position of neutron probe. This has been realised by the modelling of the spectrometer. This one, realised for the totality of facilities (by neutrons and by synchrotrons), is based on a Monte Carlo method and take in account all the elements of the instrument: the guide, the monochromator if it is necessary, the primary and secondary slits and the sample.

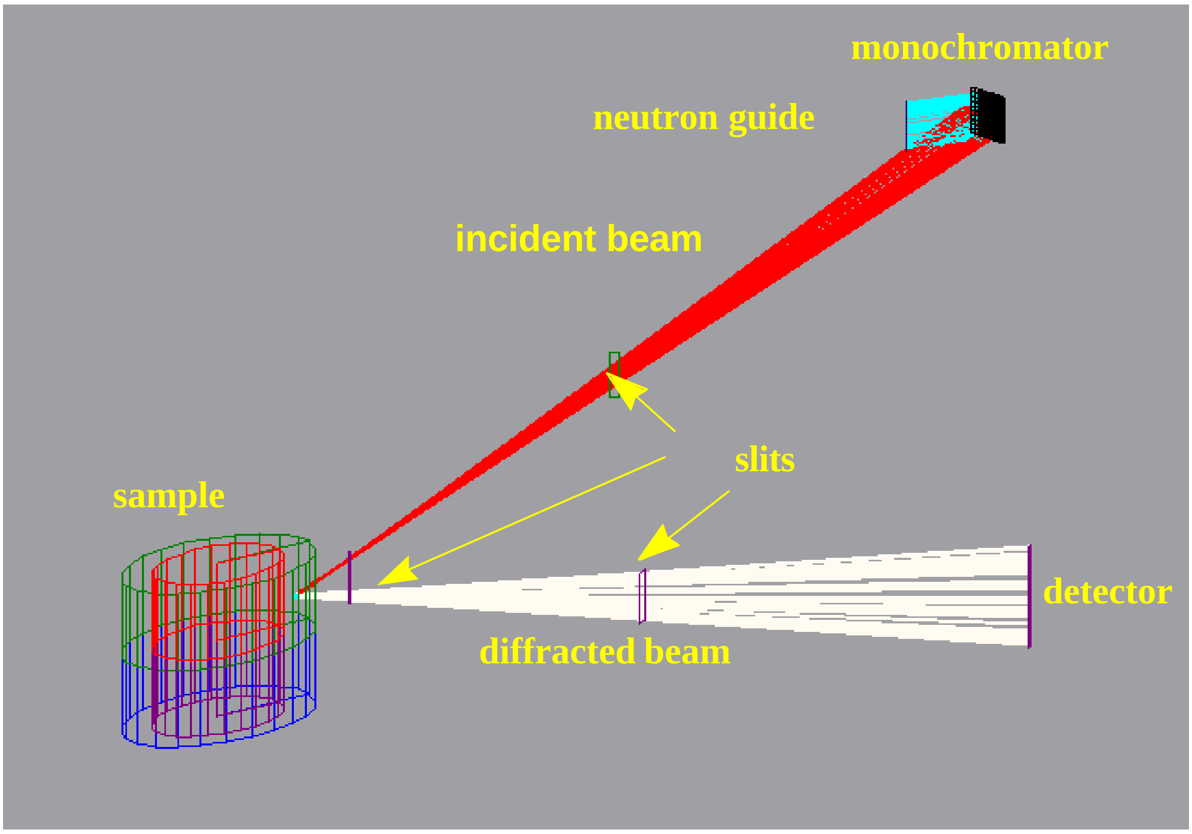

Figure 3.1: Example of simulation of a two-axis neutron spectrometer.

The true position of the neutron gauge volume is then derived from the evolution of the diffracted intensity versus the scanned depth. Such a curve can be defined by experimental methods (Figure 3.2) or by the Monte Carlo simulation programs (Figure 3.1).

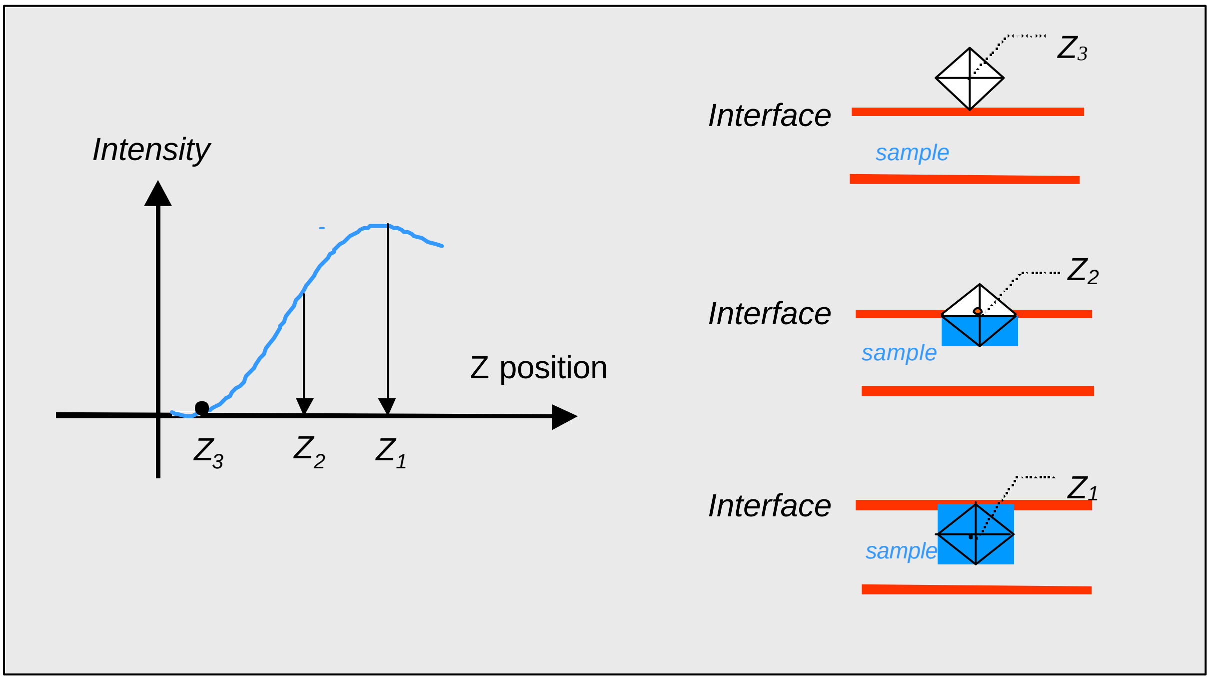

Figure 3.2: Evolution of intensity inside the sample.

The evolution of the diffracted intensity is plotted versus the position Z of the geometric centre of the neutron probe. The intensity increases when the gauge volume enters the material. For the X-rays, it then decreases quickly. Its evolution is very slow for the neutrons (Figure 3.3).

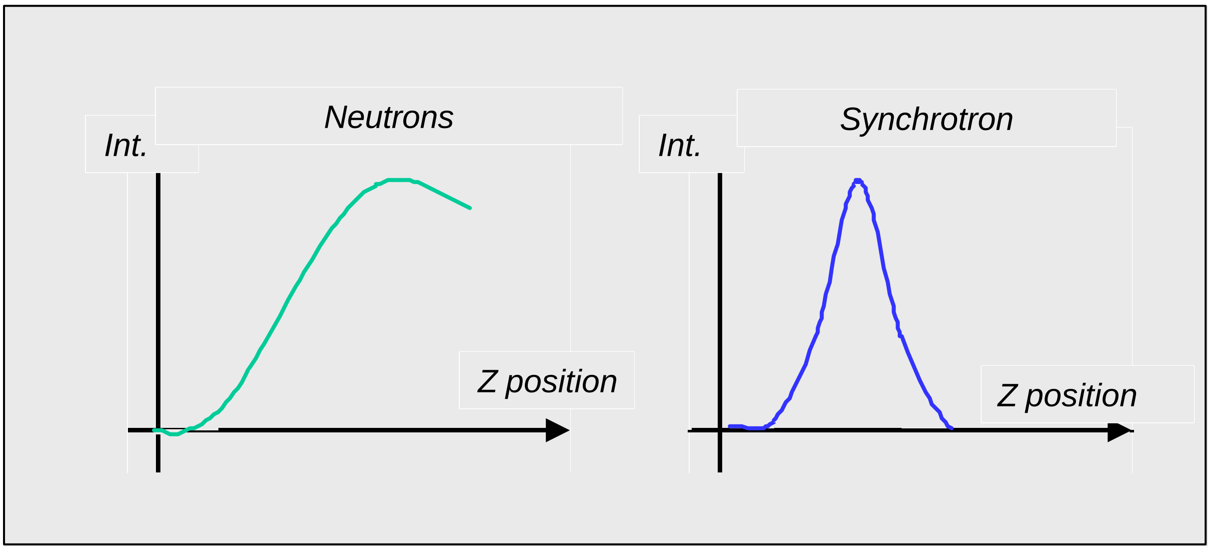

Figure 3.3: In-depth intensity curves considering the absorption of neutron and synchrotron radiation.

Classically (Figure 3.2), it is considered that at half maximum of this curve, exactly half the neutron probe is immersed.

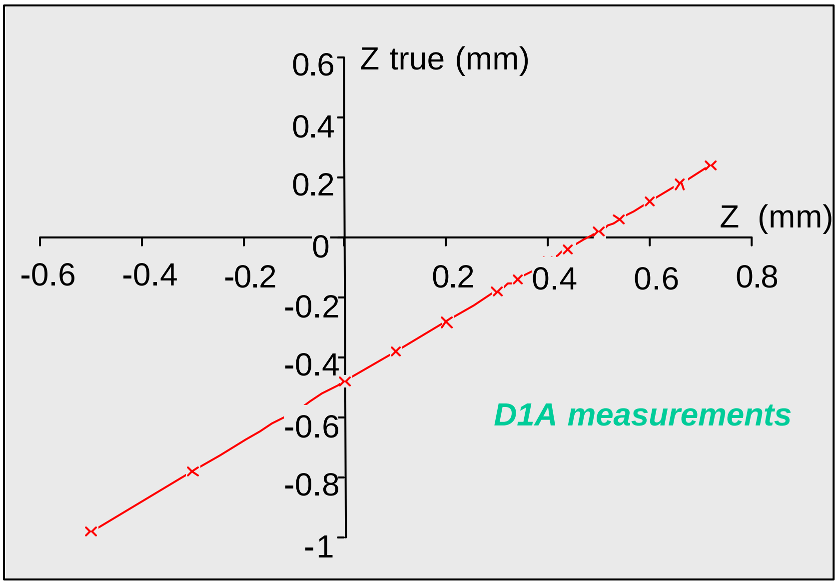

Figure 3.4: Analysed sample S1 (D1A measurement on palladium alloy substrate reported in details in Chapter 5, § 5.3.2). In this figure is shown the scanned depth Z versus theoretical Z_{true}.

In our case (Figure 3.4), due to the strong absorption of the palladium, this assumption is valid neither for the neutrons nor for the X-rays. The precise position Z has been defined therefore through the adjustment of the experimental data (neutrons and synchrotron radiation) to the theoretical curve Figure 3.6. The accuracy of this method is a few tens of micrometers for neutron strain scanning and a few microns for synchrotron measurements.

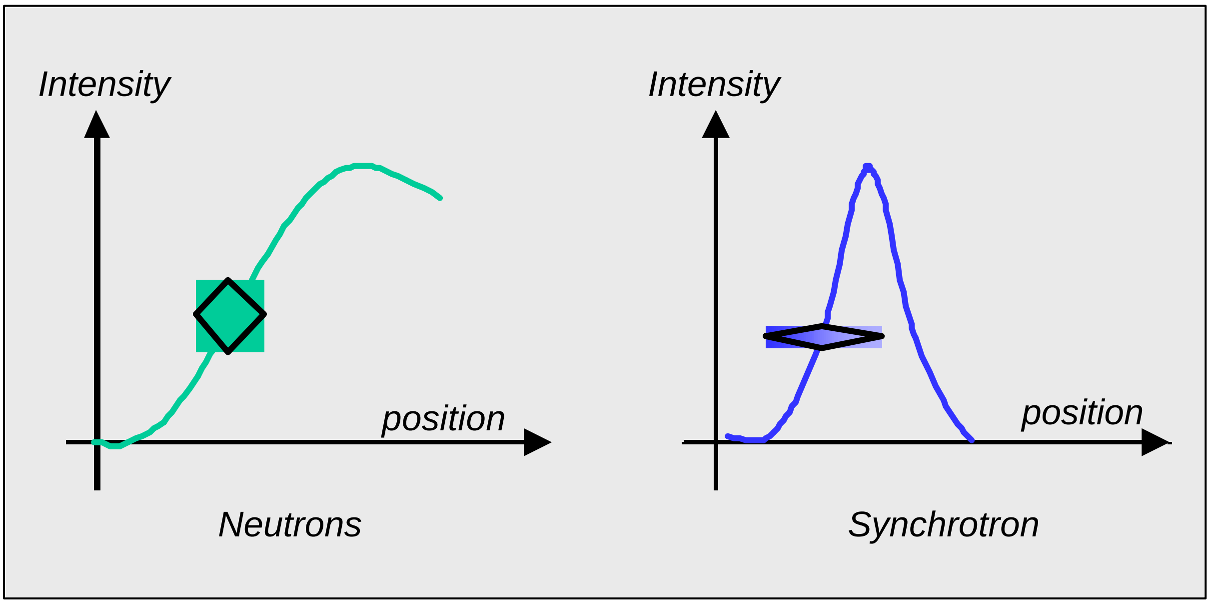

Figure 3.5: Evolution of the diffracted intensity can be plotted versus the position of the geometric centre of the gauge volume.

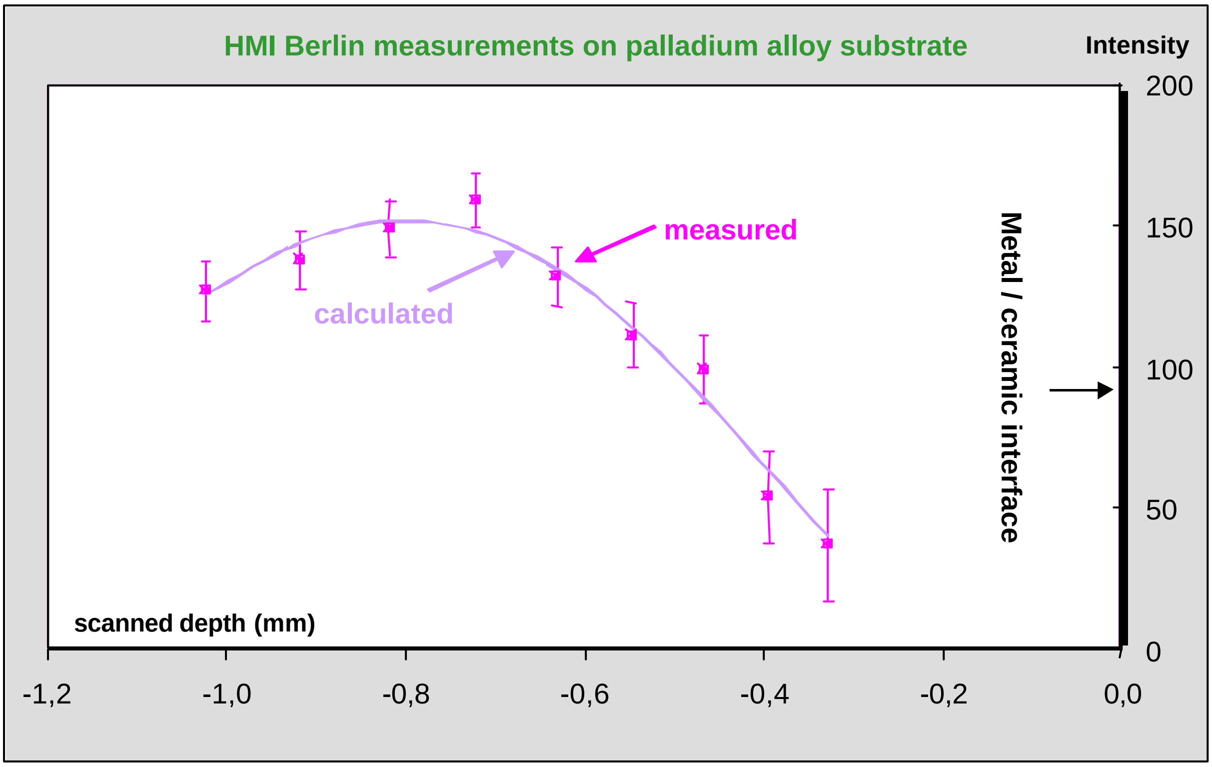

Figure 3.6: Studied sample S1 (HMI measurement on palladium alloy substrate reported in details in Chapter 5, § 5.3.1). Distribution of the diffracted intensity versus the scanned depth is shown.

Usually, it is assumed that each measurement is carried out at the position Z defined by the geometric centre of the neutron (or synchrotron radiation) probe. This approximation is valid only when the gauge volume is entirely immersed in the sample and the material is little absorbent (Figure 3.8). For the palladium, that is strongly absorbent, the true centre of gravity Z_{true} of the diffracting volume (that is the immersed part of neutron probe) has to be considered. This position has to account for the absorption phenomena (which is stronger for X-rays than for the neutrons, as shown in the Figure 3.5) and for the evolution of the local conditions of diffraction in the diffracting volume. Our simulation programs allow defining the relation between Z and Z_{true} (Figure 3.4).

Using our simulation programs, for given initial conditions, we obtain the relation between the geometric centre of the probe (z) and the centre of the diffracting volume (z_{true}). The experimental intensities are compared to the simulated curves to define precisely the position (z) of the neutron probe. In such a way, we obtain the position z_{true}. Therefore, we can evaluate the strain by Bragg's law and finally determinate the stress profile.

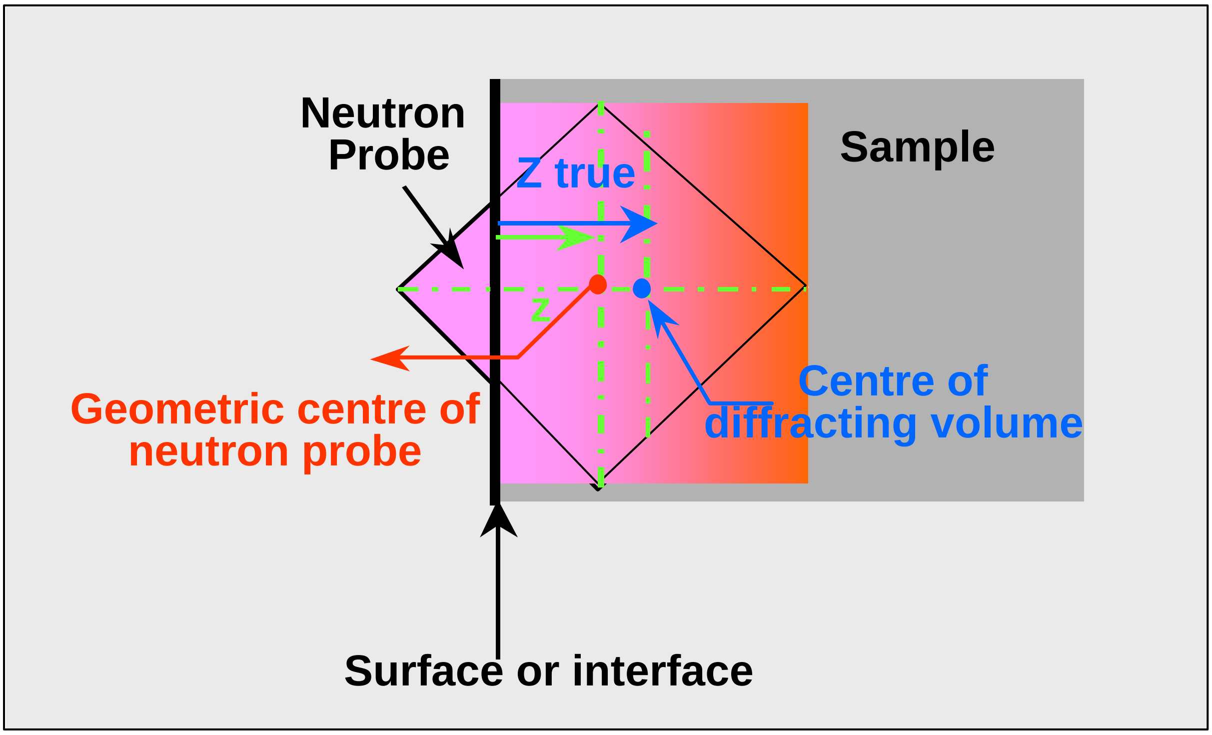

Figure 3.7: Neutron probe position.

Introduction to the new simulation programme developed for the

synchrotron radiation spectrometer applied to a metallic substrate (sample S).

Now we present, our method applied to a metallic substrate (sample S).

As we have pointed out the evaluation of residual stress by high-energy synchrotron measurements in a palladium alloy leads careful evaluation of experimental data obtained in zones, which are very difficult to analyse owing to physical phenomena, like absorption, and geometrical problems. We have therefore introduced an innovative approach to solve these problems [3.4].

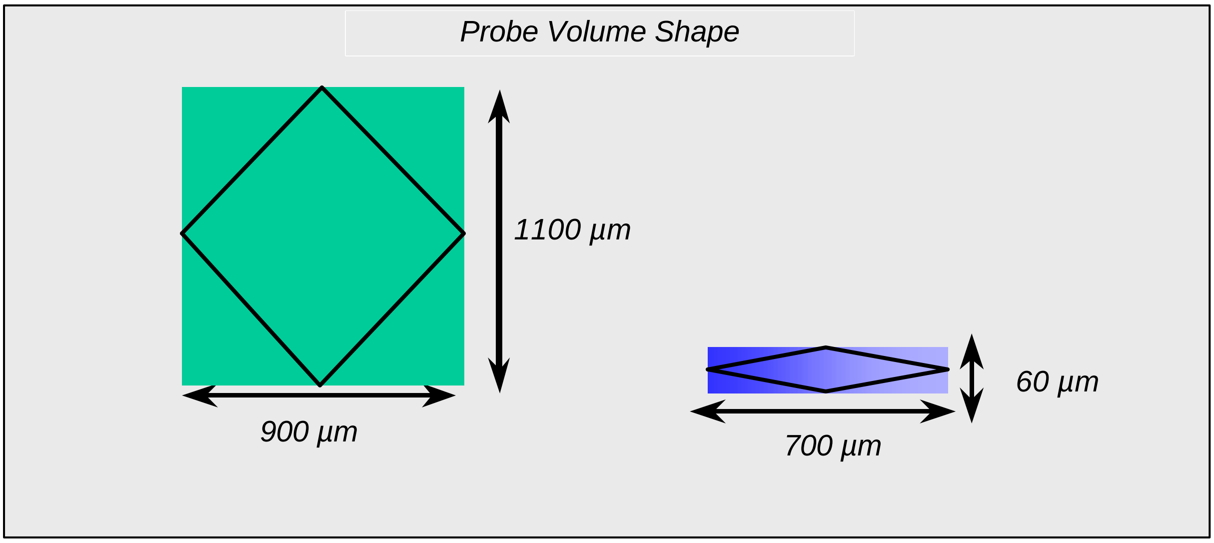

Figure 3.8: Shape of gauge volume for neutron and for synchrotron radiation measurements.

3.3.1 Position of the gauge volume and mean analysed depth:

Reliable evaluation of the in-depth stress profile requires defining accurately the position of the probe volume inside the sample. For that purpose, a precise scanning is usually performed across the studied surface or interface. This enables to plot the evolution of the diffracted intensities versus the adjustment depth of the instrument. These intensities grow when the synchrotron radiation probe enters the analysed material and then decrease quickly because of the strong absorption of the X-rays. At half-maximum of these curves it is then generally assumed, for classical adjustment procedures, that the geometrical centre of the probe volume matches the studied surface or interface. This is not true for high-density materials, like palladium. In fact, for such matter, the absorption of the X-rays affects the position of the maximum of the in-depth intensity curves (Figure 3.9). Classical procedures would thus lead to considerable errors in the determination of the true measurement depth. Absorption depends on the photon energy. These errors depend thus on the selected diffraction peak.

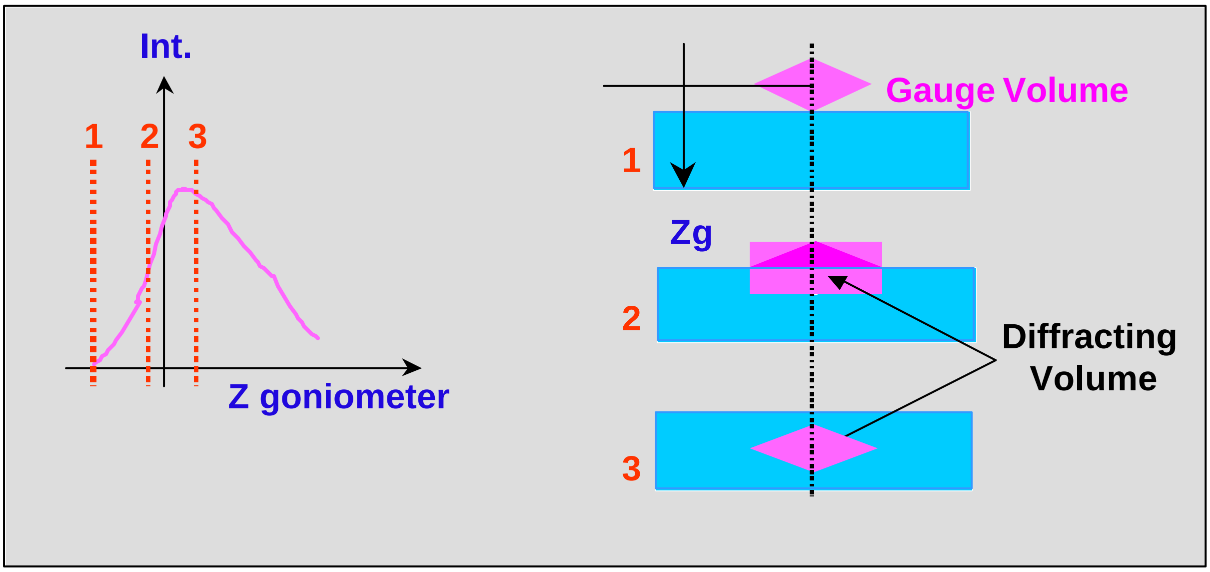

Figure 3.9: Measurement problems at the interface / surface

Whatever the position of the X-ray gauge inside the material, it is also usually assumed that the measurement is carried out in a position Z_0, located at the centre of gravity of the probe volume. For stress evaluation on low density material, this approximation is generally acceptable. However, in the case of palladium, which is strong absorbent, this assumption is no longer valid. It fact, it is then necessary to define, for each position of the probe volume, a true mean depth <Z> in the diffracting volume (immersed part of the gauge volume) which accounts for absorption of the X-rays by the material and for changes of the local conditions of diffraction (reflectivity).

3.3.2 Simulation software

Our new simulation program is based on a Monte Carlo method. It is designed to simulate any diffraction experiment carried out with X-rays and permits to predict, under the conditions of the true measurement, the diffracted intensity, as well as the shape and position of the gauge volume in the matter. A whole diffraction pattern can also be simulated.

For that purpose, the different elements of the instrument are first to be defined:

- selecting the number, size and position of the primary and secondary collimation slits,
- entering the characteristics of the detector,
- if necessary, building a monochromator,
- assembling the different parts of the instrument,
- describing the geometry and the position of the sample (CAD drawing module),
- characterising the materials (attenuation coefficients, lattice parameters).

At the beginning of the calculations, the shape, size and position of the gauge volume is also computed from the boundaries of all possible elementary paths of the incident and diffracted X-ray beams. The diffracting volume is then defined through the intersection between the gauge volume and the sample geometry.

The program itself is based on a traditional Monte-Carlo method. At least one million of elementary X-ray paths are built randomly, for each energy range and sample position, joining the source to the detector and crossing the different parts of the experimental set (primary slits, sample, secondary slits and detector). The radiation/matter interactions (absorption and diffraction) are then defined for all the simulated paths and their contributions are integrated to compute the global diffracted intensity received by the detector. At this step the mean weighted position <Z> of the diffracting volume is also calculated, accounting for the absorption of the X-rays by the sample and for the changes of local diffraction conditions. Two types of theoretical curves are thus obtained for each X-ray energy range and sample position:

- Distribution of the diffracted intensity versus the position Z_0 of the geometrical centre of the probe volume (fitting curves of Fig. 3.10). These curves are adjusted to the experimental intensities to localise the sample surface or interface.
- Relation between the mean position of the diffracting volume <Z> and the adjustment depth Z_0 (Fig. 3.11). These curves are used to define the measurement depth.

For the synchrotron radiation measurements the in-depth stress profile of the palladium alloy substrate (Chapter 5, § 5.6, Sample S) has been deduced from the positions of the 500 acquired diffraction peaks, using a least squares optimisation method. This profile has been defined for that purpose by a mathematical function. The least square refinement accounts also for the elastic anisotropy of the palladium crystallites. It is well known [5.6] that the size of the X-ray beam is very small (Figure 3.8). The true position of the diffracting volume inside the sample has to be localised therefore very precisely. As for neutrons, this is obtained by strain scanning across the studied interface, with a step of 10 µm.

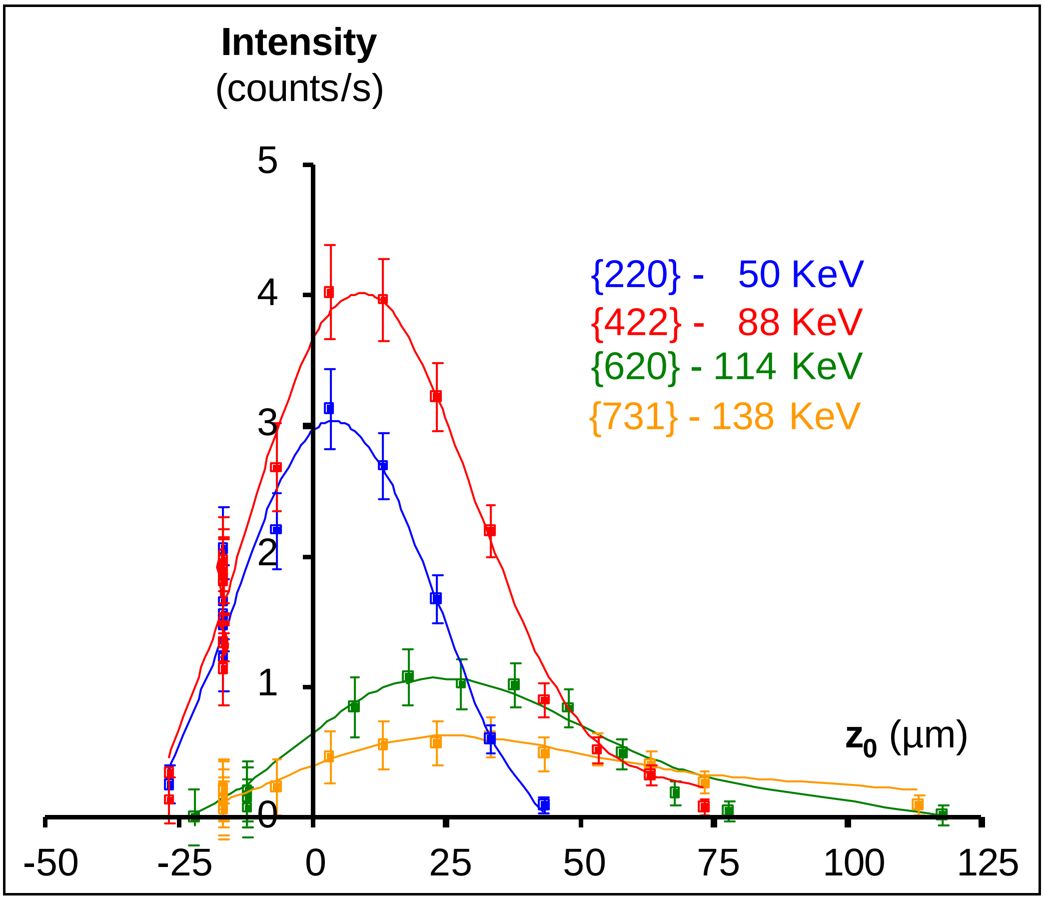

Figure 3.10: Studied sample S (ID15A measurement on palladium alloy substrate reported in details in Chapter 5, § 5.6) Evolution of the diffracted intensity versus adjusted depth Z_0.

For the synchrotron radiation measurements the in-depth stress profile of the palladium alloy substrate (Chapter 5, § 5.6, Sample S) has been deduced from the positions of the 500 acquired diffraction peaks, using a least squares optimisation method. This profile has been defined for that purpose by a mathematical function. The least square refinement accounts also for the elastic anisotropy of the palladium crystallites. It is well known [5.6] that the size of

the X-ray beam is very small (Figure 3.8). The true position of the diffracting volume inside the sample has to be localised therefore very precisely. As for neutrons, this is obtained by strain scanning across the studied interface, with a step of 10 µm.

The results show very strong absorption effects; for this reason, these phenomena have been completely modellised by the Monte Carlo simulation. It has allowed to predict the in–depth evolution of the diffracted intensity and the true centre of gravity of the diffracting volume (accounting for the absorption effects). As for the neutron experiments, the precise position of the diffracting volume has been defined through the adjustment of the experimental data to the theoretical curves.

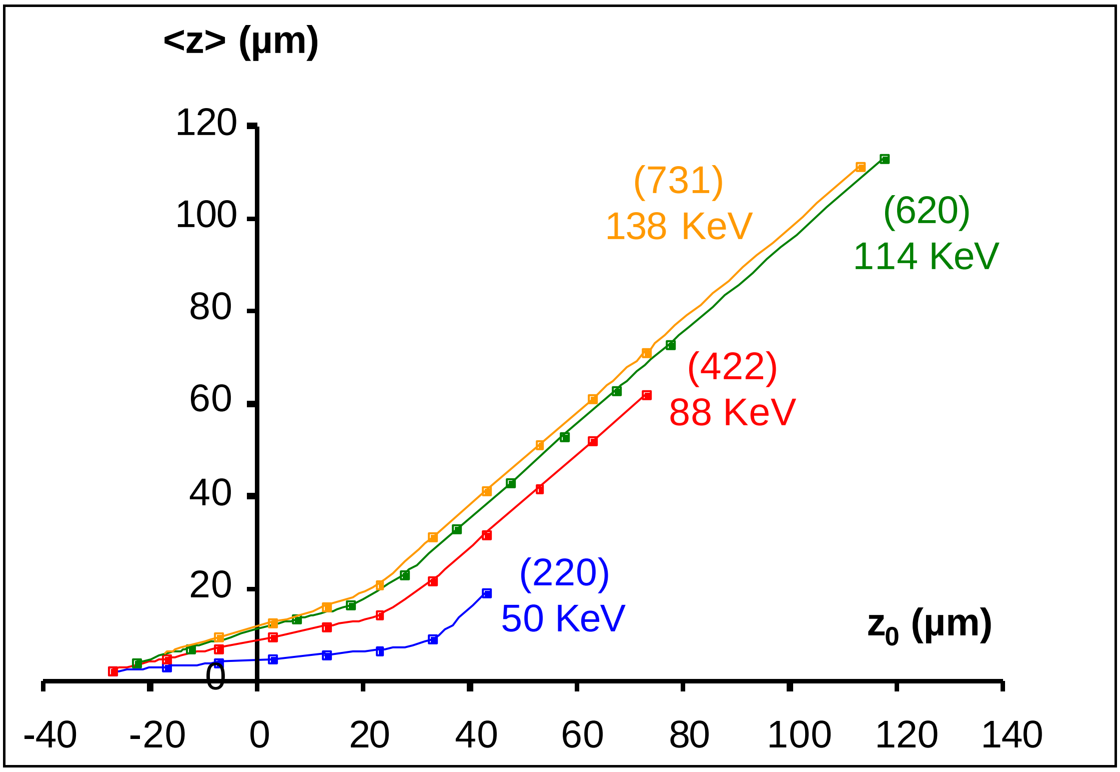

Figure 3.11: Variation of depth versus energy of the X-ray photons (ID15A measurement on palladium alloy substrate reported in details in Chapter 5, § 5.6).

REFERENCES

[3.1] Thesis of Eric Pluyette, "Contribution de la diffraction neutronique a l’evaluation des contraintes residuelles au voisinage d’interface", Univ. Reims Champagne Ardenne, N°D’ORDRE: 97-Reims-011.

[3.2] J.M. Sprauel et al, ICRS6, July 2000, Oxford.

[3.3] J.M. Sprauel, oral presentation, Journal-article, Journal of Neutron research, in press MECA-SENS 2000, Reims, 14-15 December 2000.

[3.4] A. Carradó, J.M. Sprauel, L. Barrallier, A. Lodini, “ Neutron and Synchrotron evaluation of residual stresses in coatings ” oral presentation, Journal-article, Journal of Neutron research, in press MECA-SENS 2000, Reims, 14-15 December 2000.

CHAPTER 4

CHARACTERISATION OF SAMPLES

4.1 Introduction

Ceramic/metal bounds are used in a variety of dental applications, because this way the strength of the metallic substrate can be combined with the biocompatibility of ceramics and with its optical performance. For the combination of these different materials the Porcelain-Fused to Metal (PFM) technique has been developed as strenghtening mechanism for porcelain [1.6].

To understand the behaviour of the samples (glassy porcelains containing leucite crystals fuse on palladium alloy substrate) at metal/ceramic interface, first it is better to know the internal structure of its components (substrate and coating). So, during the stage in “La Sapienza” University of Rome (Italy) it was determined the composition and the structure of ceramic coating and metallic substrate. It has required the use of several surface and in core techniques. This chapter comprises a variety of methods for the microstructural characterisation of the samples. Here electron microscopy documents the complex constitution of the compound system. Consequently, to characterise the interface between glass-ceramic coating moulded on a metal casting alloy substrate and the mechanism of adhesion, micro-analytical investigation were carried out by X-ray diffraction (XRD), by optic microscopy (OM), by Scanning Electron Microscopy (SEM) and Transmission Electron Microscopy (TEM) both equipped with and Energy Dispersive Spectrometer (EDS).

The analyses were performed in the following laboratories:

- ICMAT laboratory CNR (Montelibretti, Rome, Italy), XRD,
- MécaSurf laboratory (E.N.S.A.M , Aix en Provence, France), O.M,
- INN-NUMA laboratory (ENEA Casaccia, Rome, Italy) SEM and TEM,
- CIGA laboratory (Camerino University, Macerata, Italy) SEM.

4.2 Analysed samples

Two samples are studied:

- a palladium alloy plate without coating before thermal processing (sample S in Figure 4.1)

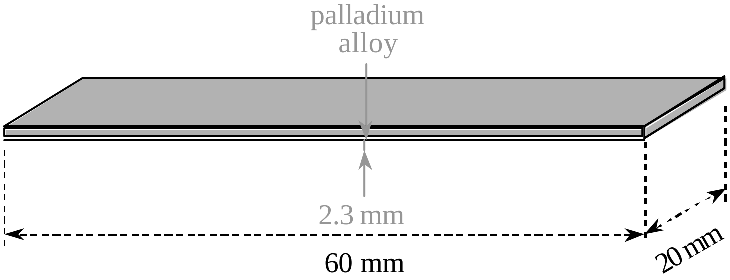

Figure 4.1: Design of the analysed sample S. It represents the Pd alloy substrate *__before thermal processing__*

- a glass-ceramic coating moulded on a metal casting alloy substrate (sample S1 in Figure 4.2).

They have been examined with SEM and TEM, equipped by Energy Dispersive Spectrometer (EDS).

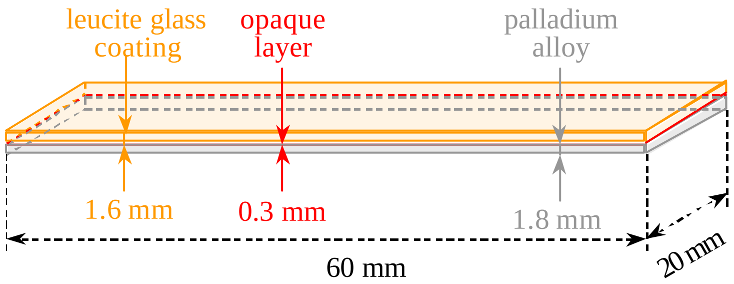

Figure 4.2: Description of the sample S1: glass-ceramic coating moulded on a metal casting alloy substrate: Glassy ceramic coating[XII] (A), Ceramic interface[XIII] (B) and Palladium alloy substrate[XIV] (C).

The analyses, which we have performed, are resumed in the following table:

Sample	**Definition**	**Analyses**
S	Pd alloy substrate before thermal processing	SEM, TEM, XRD
S1	A Glassy ceramic coating B Ceramic interface C Pd alloy substrate	SEM, XRD,TEM SEM, XRD, TEM SEM, TEM

Table 4.1: Description of the samples and performed analyses.

4.3 X-Ray Diffraction (XRD) measurements

X-ray diffraction is an analytical technique whereby crystalline compounds can be simply identified and quantified within a mixture or a pure phase. The results obtained are as a compound or mineral name as opposed to a list of elements as in other analytical methods. Solid and powdered samples can be analysed and matched against a database of 70000 recorded phases, thereby identifying the unknown phases that are contained within a sample.

[XII] *Glassy ceramic coating = leucite glass coating = Will-Ceram® body*
[XIII] *Ceramic interface = opaque ceramic interface = Will-CeramÒ opaque*
[XIV] *Pd alloy substrate = Cerapall®*

Each pure mineral or compound has a specific X-ray diffraction pattern and it is these that are matched against the unknowns. This method is a non-destructive analytical technique.

As it has already been pointed out, XRD is widely used to identify crystalline phases, to measure crystallite sizes, lattice parameters, orientation and to provide quantitative phase analysis and atomic coordinates. Furthermore can characterise the crystalline phases present and give information pertaining to the degree of crystallisation and the orientation texture. These information are important for relating the production of a material to its structure and hence its properties [4.1],[4.2].

XRD is an efficient analytical technique used to identify and characterise unknown crystalline materials. Monochromatic X-rays are used to determine the interplanar spacings of the unknown materials. Samples are analysed as powders with grains in random orientations to insure that all crystallographic directions are *"sampled"* by the beam. When the Bragg conditions for constructive interference are obtained, a *"reflection"* is produced, and the relative peak height is generally proportional to the number of grains in a preferred orientation.

X-ray spectra generated by this technique, thus, provide a structural fingerprint of the unknown. Mixtures of crystalline materials can also be analysed and relative peak heights of multiple materials may be used to obtain semi-quantitative estimates of abundance.

Data reduction routines rapidly determine peak position, relative intensities, and calculate intra - crystalline d-spacings. The complete ASTM powder diffraction file is available for identification of unknown crystalline phases.

The advantages of X-ray powder diffraction are:

- *rapid identification of unknown phases*
- *small quantities of samples are sufficient*
- *ease of sample preparation of natural and synthetic samples*
- *large library of known crystalline structures*

The sample is powdered and packed into a holder. It is then placed in the goniometer and bombarded with X-rays generated from a copper or chrome tube. A detector collects the diffracted rays and the information relayed to a computer where, using the Bragg's equation, it is converted to d-values of specific intensities. This information can then be shown graphically in the form of a diffraction pattern or diffractogram. The diffractogram from the unknown sample can then be matched against the database using the PC-Identify software.

4.4 Microscopy techniques

4.4.1 Metallographic imaging modes

The reflected light microscope is the most commonly used tool for the study of the microstructure of metals. It has long been recognised that the microstructure of metals and alloys has a profound influence on many of the properties of the metal or alloy. Mechanical properties (strength, toughness, ductility, etc.) are influenced much more than physical properties (many are insensitive to microstructure). The structure of metals and alloys can be viewed at a wide range of levels - macrostructure, microstructure, and ultra-microstructure.

The scientific observation and characterisation of the grain structure of metals and alloys is termed metallography and, in its most basic form, involves the following stages:

- *Removal of a suitable section*
- *Grinding a flat surface suitable for observation*
- *Polishing*
- *Etching (chemical or electrochemical)*
- *Observation of grain structure (e.g. with a metallurgical microscope)*

In the study of microstructure by metallography, it can determine what phases or constituents are present, their relative amounts, and their size. The microstructure is established based upon the chemical composition of the alloy and the processing steps. A small specimen is cut from a larger mass (for example: a casting, forging, rolled bar, plate, sheet, or wire) for evaluation. First, the specimen must be polished to a very high luster, free from any damage introduced by sectioning, grinding, or polishing. Otherwise, the true structure will not be revealed, and the interpretation will be inaccurate. Specimens are generally viewed in the as-polished condition first using bright-field illumination to observe those constituents that have a natural colour reflectivity difference from the bulk of the metal. This procedure is commonly used to examine intermetallic compounds, inclusions and other small particles that might be present. Some other small precipitates that have essentially the same reflectivity as the metal may also be observed if they have a much different hardness and polishing rate than the surrounding metal.

4.5 Scanning Electron Microscopy

Scanning Electron Microscope (SEM) is one of the most versatile and widely used tools of modern science as it allows the study of both morphology and composition of biological and physical materials.

By scanning an electron probe across a specimen, image resolution of about 50 Å of the morphology or topography of a specimen, with great depth of field, different magnifications can be obtained. Compositional analysis of a material may also be obtained by monitoring X-rays produced by the electron-specimen interaction. Thus, some detailed maps of elemental distribution can be produced from multi-phase materials.

SEM is often equipped with EDS (energy dispersive spectrometer) or WDS (wavelength dispersive spectrometer) to chemically characterise the materials for quantitative microanalysis (Figure 4.3). SEM with secondary and back-scattered electrons (chemical contrast) was employed.

Experimental procedures for samples studied by scanning electron microscope and EDS analysis were:

- Cleaning and sample preparation
- Metallisation for ceramic coating (carbon coated)
- X-ray Microanalysis (EDS,), qualitative and quantitative analysis

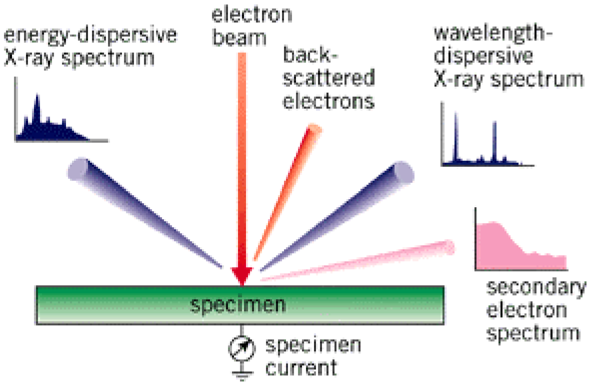

Figure 4.3: Schematic SEM diagram.

SEM consists of an energetically well-defined, highly focused beam of electrons scanned across a sample.

Secondary Electron Imaging (SEI) works on the principle that this electron beam generates electrons from the specimen with kinetic energies much lower than the primary incident electrons, called secondary electrons. Because of their low energies and low penetration depth, the detection of secondary electrons as a function of primary beam position makes it possible to attain high magnifications (as much as x 100000 in some cases) and high resolutions (up to ~50 Å resolution) for imaging the areas of interest.

Back-scattered electrons (BSE) are those electrons of the primary beam that, after interaction with sample, are scattered back with energy over 50 eV. The number of electron back scattered from the sample is directly proportional to atomic number (Z) of the substance hit by the primary beam. BSE originate not only from the surface but also from a certain depth within the sample, depending on its composition and on the energies of the primary beam electrons. BSE, when collected by appropriate detector, can therefore provide a contrast related to the chemical composition of selected area of the sample.

BSE can sometimes provide useful information even when a BSE detector is not available: back-scattered electron, when re-emerging from specimen, can interact with atoms of the surface and produce secondary electrons, also called SE II.

Backscattered Electron Imaging (BEI) detects high-energy electrons which backscatter quasi-elastically off the sample. This imaging detector operates in two modes:

- Topographical, which yields a topographic image of the sample surface and
- Compositional, which distinguishes between areas of relative low and high average atomic weights.

EDS detects X-rays from the sample excited by the highly focused, high-energy primary electron beam penetrating into the sample. When the high-energy electrons interact with the atoms of material in this "interaction volume" typically few microns in diameter, they generate characteristic X-rays, which are fingerprints of the individual atoms, encountered. These X-rays can penetrate through the material, allowing them to escape and be detected by the X-ray detector. Because the intensity of the individual X-ray is related to the quantity of the "parent atom" in the interaction volume, quantitative elemental analysis can be obtained from the sample with the aid of the powerful computer and software analysis capabilities. The software also enables one to collect elemental maps of the sample as well as line-scans, digitised secondary and backscattered electron images and perform other more sophisticated analyses.

4.6 Transmission Electron Microscopy

Transmission Electron Microscope (TEM) allows the user to determine the internal structure of materials.

Materials for TEM must be prepared to thicknesses, which allow electrons to transmit through the sample, much like light is transmitted through materials in conventional optical microscopy. Because the wavelength of electrons is much smaller than that of light, the optimal resolution attainable for TEM images are many orders of magnitude better than that from a light microscope. Thus, TEM can reveal the finest details of internal structure - in some cases as small as individual atoms. A resolution about 1 Å can be routinely obtained for many materials.

Phase determination as well as defect and precipitate orientation is typical outcomes of conventional TEM experiments. Microstructural characterisation of materials, including unit cell periodicities, can be readily determined using various combinations of imaging and electron diffraction techniques. Images obtained from a TEM are two-dimensional sections of the material under study.

The energies of the electrons in the TEM determine the relative degree of penetration of electrons in a specific sample, or alternatively, influence the thickness of material from which useful information may be obtained.

400 kV TEM JEOL 4000 FX microscope equipped with EDS Germanium detector not only provides the highest resolution available but also allows for the observation of relatively thick samples performed TEM measurements.

Because of the high spatial resolution obtained, TEM is often employed to determine the detailed crystallography of fine-grained materials. Thus, TEM is a complementary tool to conventional crystallographic methods such as X-ray diffraction.

Chemical analyses of solids can be routinely carried out via the use of spectrometers attached to electron microscopes to analyse very small regions of the sample (about nm).

When electrons interact with a specimen, various signals produced are directly related to the chemical composition of the material. With the attachment of energy or wavelength dispersive spectrometers, the precise elemental composition of materials can be obtained with high spatial resolution. In some instruments, such as a TEM equipped with an energy dispersive spectrometer (EDS), elemental analyses can be obtained from areas as small as a few nanometres diameter. Because of low count rates, these analyses usually have a relative error between 5% and 10%.

TEM is mainly employed in material science to study microphases and interfaces; the possibility to determine the lattice parameters of the observed materials either by means electron diffraction methods or by high resolution images, is of peculiar importance.

TEM can be employed to study:

- Morphology: shape, dimensions and position of the micro-crystals or particles observed on the sample
- Crystallography: position of atoms and their order degree. Study of defects in the atomic scale
- Composition: chemical composition of phases and phase mixtures

Available techniques:

- *TEM bright and dark field images TEM and/or STEM*
- Electron Diffraction Mode
- *EDS qualitative and quantitative information on the atomic species (Z > 4) present in the sample*

4.6.1 TEM specimen preparation

S and S1 specimen were prepared by plane section and cross section techniques respectively.

Plane section

Step 1: To prepare an initial slice from a large piece of material (60 x 20 x 1.2 mm^2) it was used a rotating diamond - impregnated cut-off wheel with counterbalanced loading to avoid excessive pressure on the specimen. The dimensions of cut-section are 0.3 x 20 x 1.2 mm^3. This is following cut in five slices of 0.3 x 4 x 1.2 mm^3 (Figure 4.4).

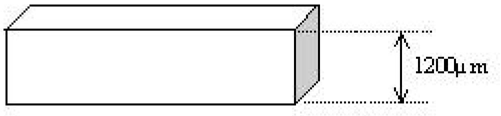

Figure 4.4: TEM slide from sample S.

Step 2: A mechanical thinning of sample was performed for obtaining a flat parallel-side sheet of 60 µm thick. A lapping machine was used for the different grinding and polishing steps (Figure 4.5).

The specimen was glued to the central core of a precision grinder. The material was removed and then polished going from coarse paper to fine until a smooth flat surface is obtained (180, 400, 600, 1000 and 1200 grit).

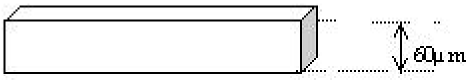

Figure 4.5: A parallel-sided disk was prepared by using precision grinder.

Step 3: Lapping is achieved by feeding silicon carbide (6, 3, 1 µm) suspended in alcohol.

Step 4: By means, a lever punch one of these slices has been obtained a 3 mm disc.

Step 5: A dimple grinder (Figure 4.6) was used for the final thinning of specimen, for obtaining a disc containing a depression in its centre of 10 µm thick.

In fact this mechanical dimpling thins the centre of the sample yielding produces a larger thin area with thicker rims that makes ductile samples easier to handle.

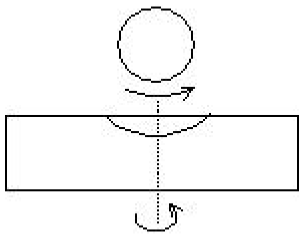

Figure 4.6: Dimple grinder.

Step 6: A beam of argon ions at energy of 5 keV was used to remove material from the surface of a sample. This process is known as sputtering and is used for thinning specimens for electron microscopy. The technique offers the only approach to the deformation-free thinning of materials.

Ions with energy of 5 keV only penetrate a few nanometers into materials and, by collision, one or more atoms in the sample may be ejected from the surface by each incident ion. The bombarding ion is done with a gas that must be heavy for a fast thinning rate, and must not interact chemically with the specimens.

Two guns were employed to bombard both sides of disc specimen at the same time the angle of incidence (5°) and obtaining a hole in the centre of sample. During thinning specimen, it is rotated (Figure 4.7 and Figure 4.8).

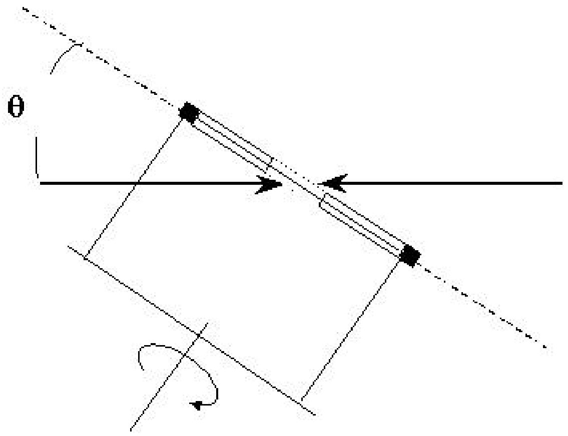

Figure 4.7: Schematic diagram.

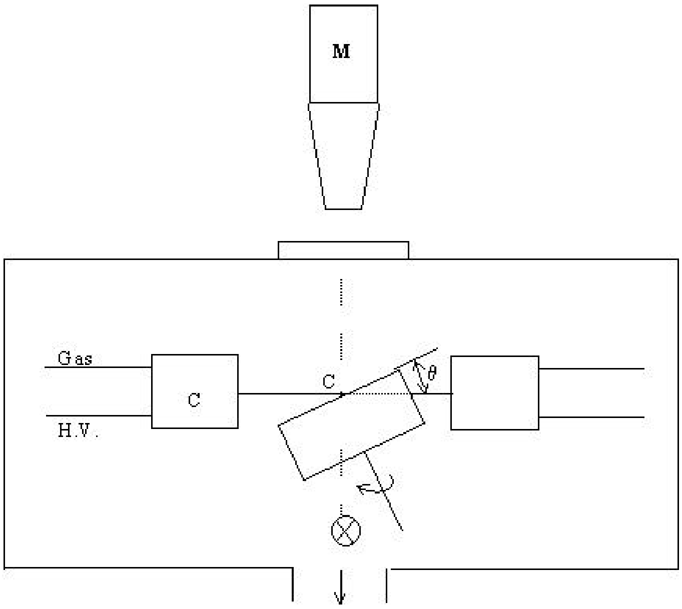

Figure 4.8: Precision ion polished system ion beam.

Cross-section

To investigate the variation of the microstructure and of the composition interface zone of S1 sample cross – sectional thinning technique has been needed. Cross section is one of the most difficult techniques to obtained ion-milled TEM sample.

Briefly, only the Step 1 is different in comparison of plane section.

To prepare successfully a cross section of a specific area composed of three different materials a slice was cut perpendicular to the surface of sample. Then a 3 x 20 x 3.7 mm^3 sample (Figure 4.9, A) was obtained by cutting a slice, with the original surface exactly bisecting it [4.4]. This one is following cut in order to obtain a slice of 3 x 3 x 3.7 mm^3 (Figure 4.9, B).

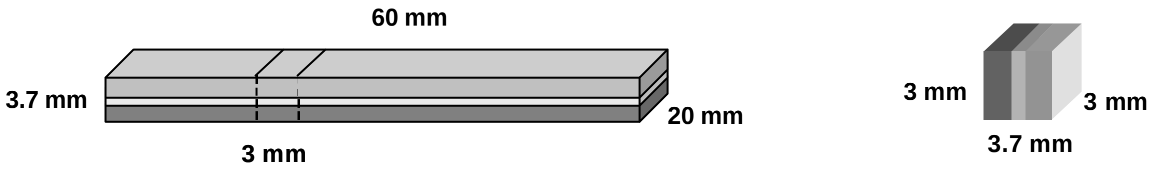

A: Perpendicular cut **B:** TEM slice

Figure 4.9: A schematic preparation of sample preparation.

Step 2: Mechanical thinning was performed. The start thickness of sample was about 4000 µm and its final thickness was 120 µm was obtained using coarse paper starting to 800 until 1200 grit.

Step 3: The same procedure like before.

Step 4: It was not realised.

Step 5: By dimple grinder, the sample contained a depression of 40 µm thick.

Step 6: Ion milling was the standard step employed to prepare plane section TEM thins sample (Figure 4.10).

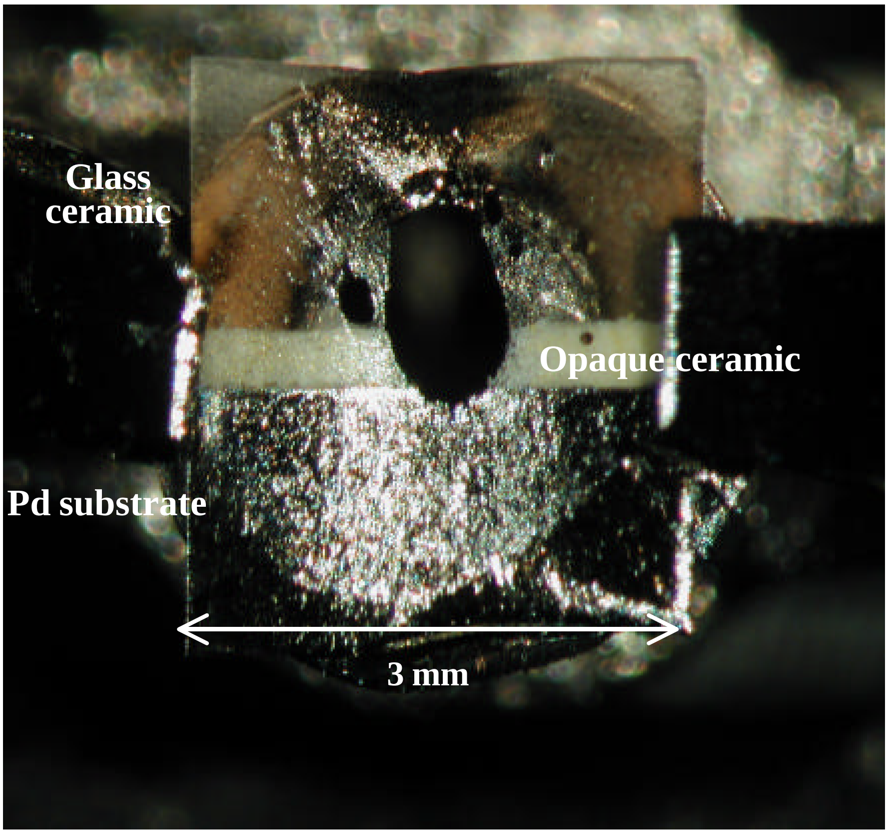

Figure 4.10: Cross-section TEM thin sample.

4.7 Microstructure: sample characterisation

Microstructural of Palladium alloy substrate and leucite- type glass-ceramic coating were investigated using XRD, OM, SEM and TEM both equipped with EDS [4.9], [4.10], [4.11].

4.7.1 XRD experimental procedures

X-ray measurements have been performed by means two-axis powder diffractometer XRD - 3000 P designed by Seifert, according to Brentano - Bragg geometry.

XRD were carried out to determine the phase in: P1 and P2 powders, A and B coatings and C substrate on diffractometer operating at 50 kV and 30 mA with Cu $K_{\alpha 1}$ radiation ($\lambda_{K\alpha 1}$ =

0.15406 nm) and graphite monochromator, in a θ- 2θ geometry coupled with a scintillation detector. The experimental conditions used are listed in the Table 4.2 below:

Sample		Primary slits	Secondary slits	Start - end angle (°)	Step width (°)	Preset time (hours)
S		2 mm / soller /3 mm	0.3 mm / soller / 0.2 mm	35 - 140	0.02	1
S1	A			5 - 80	0.04	24
	B			5 - 80	0.04	24
	C			35 - 140	0.02	1
P1 [XV]				5 - 80	0.02	24
P2 [XVI]				5 - 80	0.02	24

Table 4.2: Experimental parameters.

Phases identified by x-ray diffraction in glass-ceramic coating and ceramic interface zone and their associated powders (JCPDS cards) are presented in table 4.4.

XRD patterns of B opaque ceramic and of P1 powder contained diffraction lines of different crystalline phases: **$KAlSi_2O_6$, CeO_2, TiO_2, ZrO_2** [XVII]and a broad maximum due to an **amorphous component** (

Figure *4.11*).

In P2 powder and in A ceramic coating samples a great amorphous fraction is present. Two crystalline phases have been detected: **$KAlSi_2O_6$ and TiO_2** (Figure 4.12).

[XV] *P1 powder is the opaque powder used for preparing the opaque coating B*

[XVI] *P2 powder is the powder used for preparing the glass ceramic coating A*

[XVII] *For more detail, refinement parameter of opaque powder and body powder (see § 4.7.2.1).*

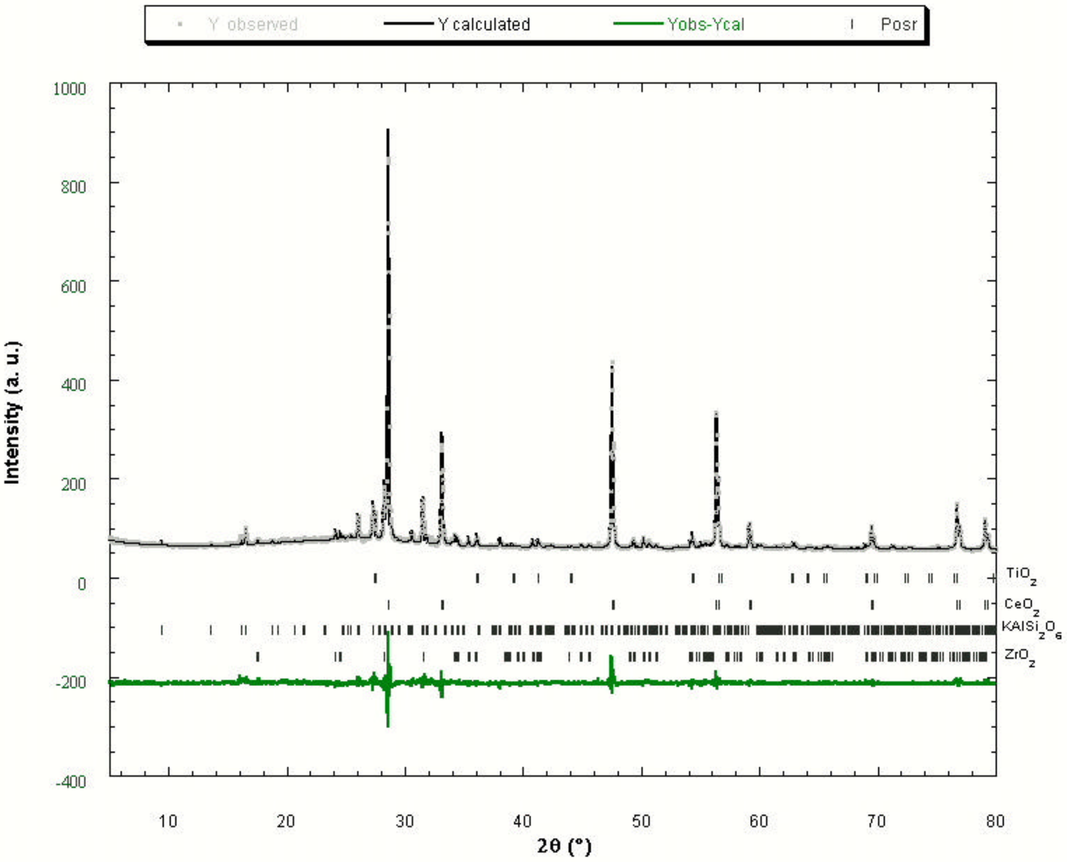

Figure 4.11: X-ray diffraction patterns of opaque ceramic interface[XVIII] *(B)*

[XVIII] *Ceramic interface = opaque ceramic interface = Will-CeramÒ opaque*

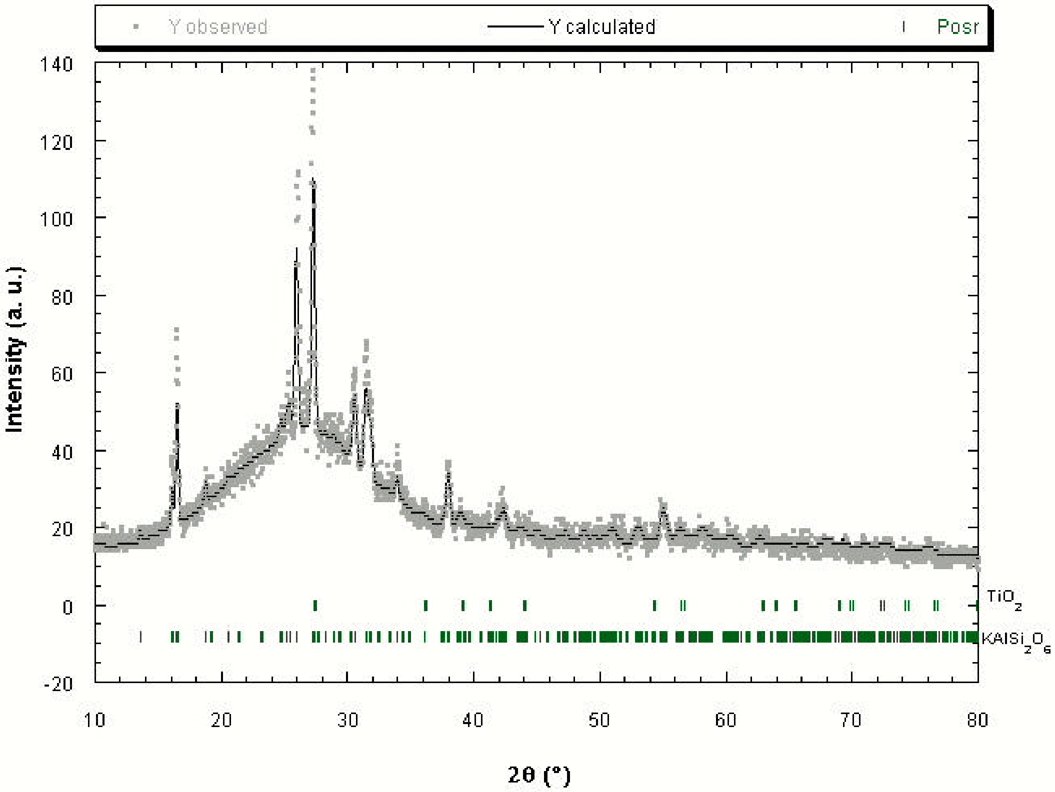

Figure 4.12: X-ray diffraction patterns of glassy ceramic coating[XIX] *(A)*

Figure 4.13, reports X-ray spectrum palladium alloy substrate. Table 4.3 reports the experimental interplanar distances (*d*), coming from the peaks positions in Figure 4.13. These distances do not correspond to theoretical values of *d* from the JCPDS **5-0681** card. In fact, the substrate is a ternary solid solution composed by palladium, silver and tin an overall, the tin presence induces an expansion of the lattice parameter (see §4.10.1).

[XIX] *Glassy ceramic coating = leucite glass coating = Will-Ceram® body*

hkl	d – from literature (Å)	d – experimental (Å)
111	2.2420	2.2796
200	1.9483	1.9760
220	1.3776	1.3932
311	1.1723	1.1888
222	1.1227	1.1430
400	0.9724	0.9863
331	0.8927	0.9024
420	0.8699	0.8827

Table 4.3: Miller indices with corresponding to interplanar distances d for some intense peaks of CFC phase Palladium (on the left); values of reference of d (in the middle); experimental values of d (on the right).

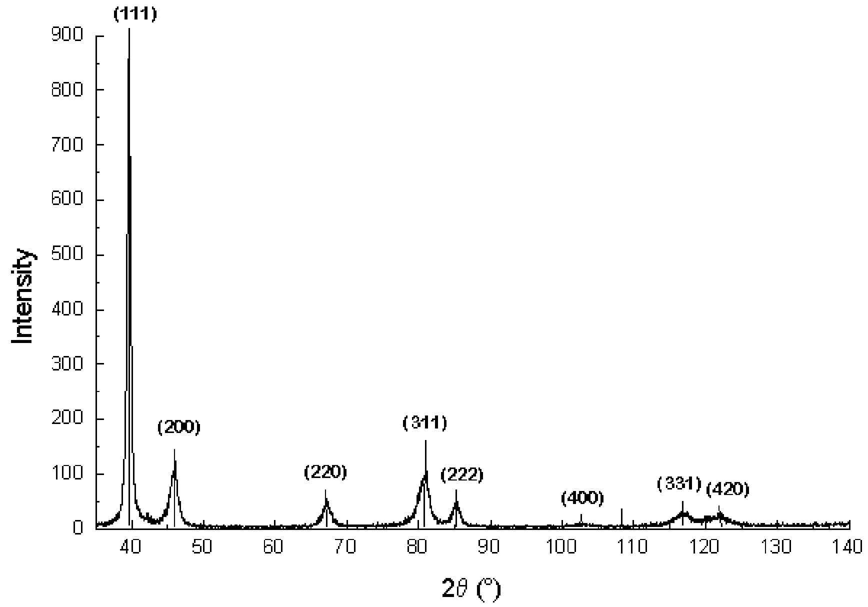

Figure 4.13: X-ray diffraction patterns of palladium alloy substrate (C).

Specimen	**Phase**	**Formula**	**JCPDS cards**
Glass-ceramic coating (A)	Titanium dioxide	TiO_2	33-1381
	Leucite	$KAlSi_2O_6$	38-1423
Opaque ceramic interface (B)	Leucite	$KAlSi_2O_6$	38-1423
	Cerianite	CeO_2	43-1002
	Rutile	TiO_2	21-1276
	Baddeleyite	ZrO_2	37-1484

Table 4.4: Phases identified by x-ray diffraction in glass-ceramic coating and ceramic interface zone and their associated powders (JCPDS cards).

4.7.2 Rietveld analysis

Structures have been determined qualitatively using Rietveld method of powder P1, P2 and zone A and B of sample S1 studied by X-ray powder diffraction (more in detail in Appendix A.4).

Briefly, Rietveld Analysis [4.6] is a "whole pattern" treatment rather than a limited number of reflections of the X-ray data and it gives the type of structural analysis normally obtained by a single crystal diffractometer. It was originally conceived as a refinement method for crystal structures using neutron diffraction data. Nevertheless, it is also used for X-ray diffraction.

The Rietveld method requires knowledge of the approximate crystal structure of all phases of interest. The input data required calculating a synthetic pattern includes the space group symmetry, number of atoms, atomic positions, temperature factor, site occupancies, and latticing parameters. The refinement is conducted by minimising the sum of the weighted, squared differences of this calculated pattern and the observed intensities every step in a digital powder pattern. In a typical refinement, individual scale factors (related to the weight percents of each phase) and profile, background, and lattice parameters are varied. In favourable cases, the atomic positions and site occupancies can also be successfully varied. Since the method uses all lines, severely overlapping reflections are not a problem. The method can obtain the following crystallographic information:

- *Lattice parameters:*

Since systematic errors (caused by sample displacement) are corrected during refinement, accurate values up to one part in 1000 can be obtained on solid samples without an internal standard. Additionally, accurate cell dimensions can be computed on low symmetry materials.

- *Accurate phase quantification:*

  Scale factors are refined and are related to weight percent of each phase. Complex mixtures with overlapping reflections are quantified with a high degree of accuracy (about 1 wt. %).

- *Crystallite size and strain:*

  A mathematical function is used to model the profiles and to separate diffraction peak broadening due to size from that due to strain. Size and microstrain values are derived simultaneously from the XRD pattern.

- *Site occupancies:*

  Yields quantitative information as to the extent of solid solution or isomorphous substitution.

- *Atom Positions:*

Positions of selected cations in the unit cell can be computed.

Order/Disorder and crystallite size determinations:

The degree of crystal perfection or the degree of atomic ordering can be determined by the Scherrer line broadening measurements. The crystallite size in a structure can be evaluated by diffraction line broadening studies as crystallite size becomes smaller than 2000. This quantification of the degree of order is important in many materials applications. Many order/disorder conditions are temperature related. These effects can be kinetically followed by high temperature diffractometry.

4.7.2.1 An example of refinement powder P1 (opaque ceramic):

The Rietveld method is a crystal structure refinement method, from powder diffraction data.

Only, the pattern of samples P1 (opaque ceramic powder) was calculated from a series of structural parameters (cell, atomic co-ordinates, thermal motion, etc) and peak shape and width parameters (plus background, Lorentz-polarisation correction, etc), and compared to the observed data. Parameters have been adjusted by a least-square process. The used PROGRAM is FullProf.2k (Version 1.8a - Dec2000-LLB JRC).

For the samples P2 (glass ceramic powder) the refinement was not possible due to the great quantity of amorphous. The precise volume fraction of amorphous and crystallised parts are not possible to quantify, this is due to the difficulty to obtain reference powder from the manufactured, which are required for quantitative phase analysis.

Powder P1

```
=> Crystal Structure Refinement for phase: 1
 =>-------> Pattern#  1
 => Crystal Structure Refinement for phase: 2
 =>-------> Pattern#  1
 => Crystal Structure Refinement for phase: 3
 =>-------> Pattern#  1
 => Crystal Structure Refinement for phase: 4
 => Scor: 1.8133

  ==> RESULTS OF REFINEMENT:

------------------------------------------------------------------------------------
 => Phase No.  1 Name: Rutile                     P 42/m n m
------------------------------------------------------------------------------------

 ==> ATOM PARAMETERS:

  Name     x      sx       y      sy       z       sz      B    sB   occ.   socc.

 Ti    0.00000(   0)  0.00000(   0)  0.00000(   0)  0.998(  0)  0.125(  0)
 O     0.30519(   0)  0.30519(   0)  0.00000(   0)  1.672(  0)  0.250(  0)

 ==> PROFILE PARAMETERS FOR PATTERN#  1

 => Cell parameters      :
                              4.59970   0.00041
                              4.59970   0.00041
                              2.96237   0.00047
                             90.00000   0.00000
                             90.00000   0.00000
                             90.00000   0.00000
```

=> Phase No. 2 CeO2 F m 3 m

```
==> ATOM PARAMETERS:

 Name     x      sx        y      sy        z       sz       B    sB   occ.   socc.

Ce     0.00000(    0)  0.00000(    0)  0.00000(    0)  0.460(  0)  0.020(  0)
O      0.25000(    0)  0.25000(    0)  0.25000(    0)  0.922(  0)  0.040(  0)


=> Cell parameters        :
                               5.41295    0.00011
                               5.41295    0.00011
                               5.41295    0.00011
                              90.00000    0.00000
                              90.00000    0.00000
                              90.00000    0.00000
```

=> Phase No. 3 Leucite I 41/a

```
==> ATOM PARAMETERS:

 Name     x      sx        y      sy        z       sz       B    sB   occ.   socc.

K      0.36600(   0)  0.36450(   0)  0.11470(   0)  0.460(  0)  1.000(  0)
Al1    0.05790(   0)  0.39640(   0)  0.16660(   0)  0.460(  0)  0.320(  0)
Si1    0.05790(   0)  0.39640(   0)  0.16660(   0)  0.460(  0)  0.680(  0)
Al2    0.16760(   0)  0.61150(   0)  0.12830(   0)  0.460(  0)  0.320(  0)
Si2    0.16760(   0)  0.61150(   0)  0.12830(   0)  0.460(  0)  0.680(  0)
Al3    0.39240(   0)  0.64180(   0)  0.08600(   0)  0.460(  0)  0.320(  0)
Si3    0.39240(   0)  0.64180(   0)  0.08600(   0)  0.460(  0)  0.680(  0)
O1     0.13180(   0)  0.31310(   0)  0.11000(   0)  0.922(  0)  1.000(  0)
O2     0.09210(   0)  0.51070(   0)  0.13030(   0)  0.922(  0)  1.000(  0)
O3     0.14530(   0)  0.67980(   0)  0.22750(   0)  0.922(  0)  1.000(  0)
O4     0.13330(   0)  0.68410(   0)  0.03540(   0)  0.922(  0)  1.000(  0)
O5     0.29000(   0)  0.57720(   0)  0.12050(   0)  0.922(  0)  1.000(  0)
O6     0.48260(   0)  0.61740(   0)  0.16670(   0)  0.922(  0)  1.000(  0)


=> Cell parameters        :
                              13.09754    0.00094
                              13.09754    0.00094
                              13.71113    0.00148
                              90.00000    0.00000
                              90.00000    0.00000
                              90.00000    0.00000
```

=> Phase No. 4 Baddeleyite P 21/c

```
==> ATOM PARAMETERS:

 Name     x      sx        y      sy        z       sz       B    sB   occ.   socc.

Zr     0.27580(   0)  0.04040(   0)  0.20890(   0)  0.460(  0)  1.000(  0)
O1     0.06900(   0)  0.34200(   0)  0.34500(   0)  0.922(  0)  1.000(  0)
O2     0.45100(   0)  0.75800(   0)  0.47900(   0)  0.922(  0)  1.000(  0)
```

```
=> Cell parameters      :
                            5.14757   0.00043
                            5.21246   0.00046
                            5.31534   0.00048
                           90.00000   0.00000
                           99.22233   0.00657
                           90.00000   0.00000

=> Global user-weigthed Chi2 (Bragg contrib.):.337
```

```
=> Phase:  1
=> Bragg R-factor:  14.2       Vol:   62.676( 0.013)  Fract(%):   11.77( 0.34)
=> Rf-factor= 8.41             ATZ:  159.730          Brindley:  1.0000
```

```
=> Phase:  2
 => Bragg R-factor:  3.68       Vol:  158.600( 0.005)  Fract(%):   41.60( 0.38)
 => Rf-factor= 1.93             ATZ:  688.450          Brindley:  1.0000
```

```
=> Phase:  3
 => Bragg R-factor:  28.7       Vol: 2352.085( 0.350)  Fract(%):   31.38( 0.66)
 => Rf-factor= 21.4             ATZ: 3491.950          Brindley:  1.0000
```

```
=> Phase:  4
 => Bragg R-factor:  15.5       Vol:  140.775( 0.021)  Fract(%):   15.25( 0.26)
 => Rf-factor= 11.7             ATZ:  492.890          Brindley:  1.0000
```

4.8 Optical Microscopy

A small section of sample S has been obtained with a hacksaw without overheating the specimen .as a consequence of an excessive heating can result in changes in the grain structure.

Before grinding a flat surface, suitable for observation under the microscope, the specimen has been mounted in a epoxy resin to allow easy handling. It has been grinded using water-lubricated SiC abrasive papers, starting with a coarse grade (e.g. 120 grit), and progressively working though finer grades until all but the faintest scratches have been removed (e.g. 1200 or 2000 grit). The paper was mounted on a rotating disk and the surface of the specimen held in contact with it. The result should be a surface which reflects light uniformly to give a high gloss. The polishing technique is carried out in a similar fashion to grinding, on a rotating disk, which carries a cloth impregnated with the polishing medium (e.g. diamond) in a lubricant (alcohol).

To reveal the grain structure, a procedure of etching was used, which may be an electrochemical etching. The surface was then quickly dried with warm air.

The most obvious effect of the etchant is that the surface has been dulled in the procedure but, on observation of the etched surface under the microscope, details of the grain structure (and other structural aspects) has been revealed.

4.8.1 Observation of grain structure

The grain structure has been observed using a reflected light microscope. This instrument in that the illumination is directed internally down the barrel of the microscope and out through the objective lens assembly to impinge normally on the surface to be examined. The light reflected from the surface is gathered by the objective and transmitted through the eyepiece to form the image of the surface.

Generally the effect of the etchant is a preferential chemical dissolution of grain boundaries only or of grain boundaries and surface of grains.

The etchant preferentially attacks the material at the grain boundaries, which is of high reactivity. The effect is that the grains are rendered as areas of different reflectivity, depending of the orientation of the lattice planes in each grain with respect to the incident illumination. If planes of atoms are arranged parallel with the surface, high reflectivity occurs, and the grain appears bright.

After polishing and electro-polished with a solution of 50% methanol, 33% nitric acid, 17% phosphoric acid [4.6] the palladium alloy substrate was observed by reflected light microscopy (RLM) coupled to an image analyser system. The morphology was observed by a RLM (Figure 4.14).

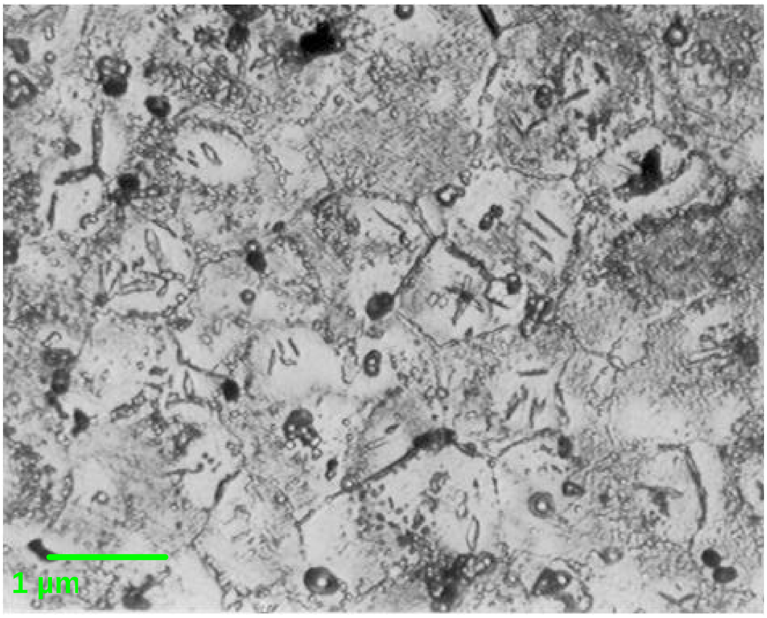

Figure 4.14: Micrograph of the palladium alloy substrate (sample S) after etching (1000 X).

In this image inside the grain it is possible to note the presence of twin. More detail are present In the paragraph of TEM measurement.

4.9 SEM experimental procedures and results

The morphology and chemical composition of specimen S and S1 were investigated by SEM Cambridge S 360 equipped with a energy dispersive X-ray spectrometers Si(Li) and Cambridge Stereoscan 250 MKII equipped with a Germanium. Qualitative microanalyses have performed by EDS to chemically characterise the specimens. SEM with secondary and back-scattered electrons (chemical contrast) was employed.

The sample S and S1 were surface polished. S was electro-polished with a solution of 50% methanol, 33% nitric acid, and 17% phosphoric acid, [4.6] before metallisation. By means of sputter coater fine grain size conductive film on very thin carbon layer was deposited on ceramic coating of the specimen S in vacuum. SEM picture along a defined area of sample - analysed by BSE is shown in Figure 4.15.

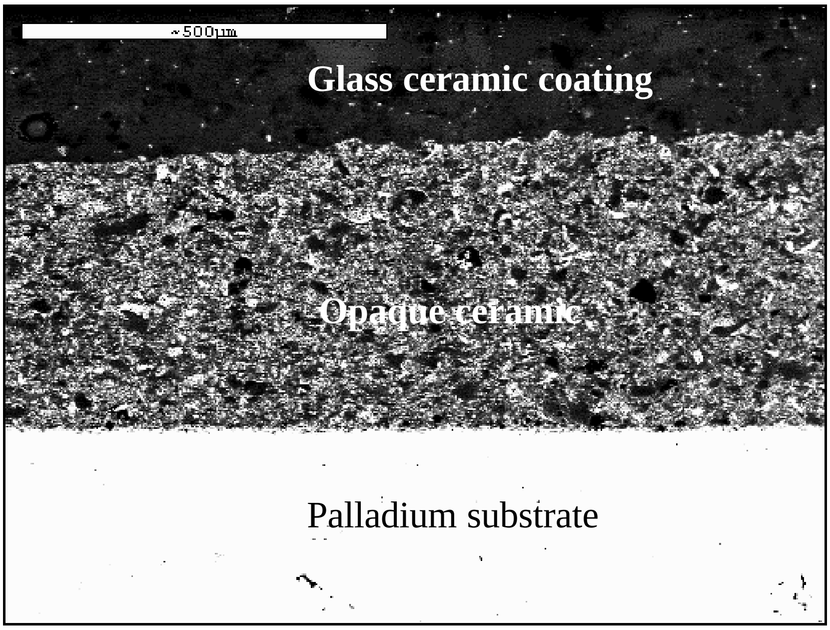

Figure 4.15: BSE micrograph of a section of sample S1

The results of this measurement by BSE show that palladium alloy and leucite are homogeneous.

Figure 4.16: BSE micrograph of interface between opaque ceramic and palladium substrate.

In the **opaque ceramic** (Figure 4.18) have been detected different regions. There are different precipitates and the region appears not homogeneous.

- White regions are rich in tin, there are also silicon and aluminium and traces of potassium, sodium, cerium and titanium in variable percentage;
- Dark white regions tin and silicon are in the same proportion and traces of aluminium sodium and cerium.
- Grey regions silicon is the element more detected. Traces of aluminium, potassium and titanium.

Figure 4.17: scanning electron micrography by BSE of ceramic interface (zone B).

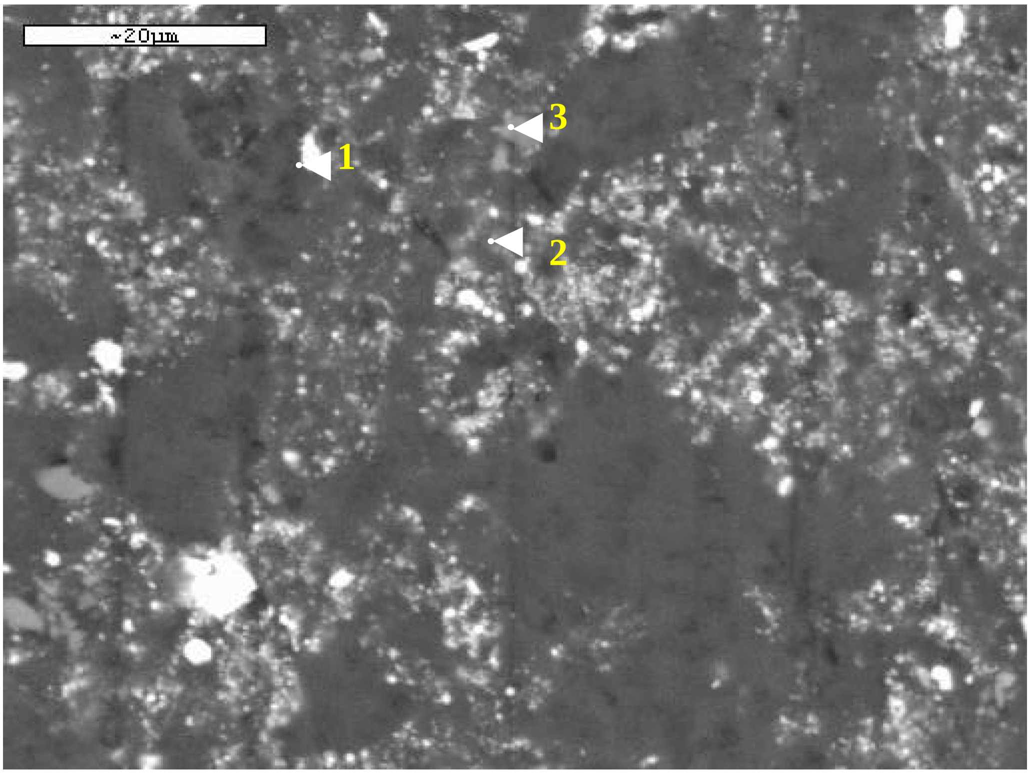

Figure 4.18: Scanning electron micrograph by BSE of opaque ceramic interface (zone B)

In **glassy ceramic coating** different regions have been studied (Figure 4.19). EDS has shown that:

- Light grey regions: titanium is the element more detected. There are also aluminium silicon, tin and potassium.
- Grey regions: silicon is the element more detected. Traces of aluminium, potassium and sodium.
- Black regions: there are a strong concentration of silicon and aluminium, few titanium and traces of potassium and sodium.
- White regions are rich in tin; there are also traces aluminium silicon and sodium.

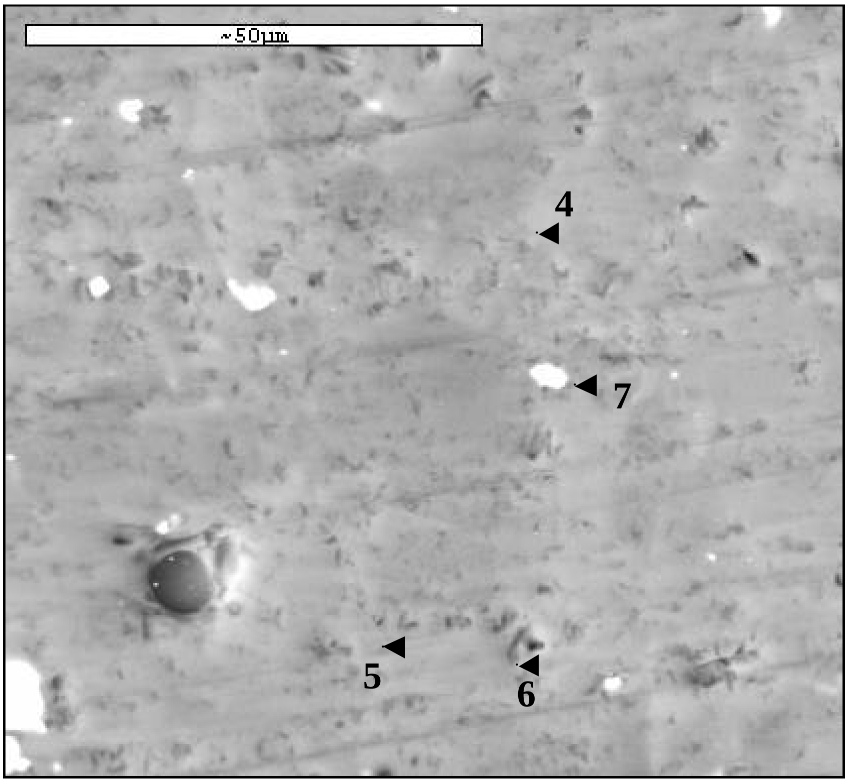

Figure 4.19: Scanning electron micrograph by SE of glassy ceramic (zone A)

As shown in Figure 4.20, a brittle fracture due to cleavage is present. The grain size is approximately 70 μm.

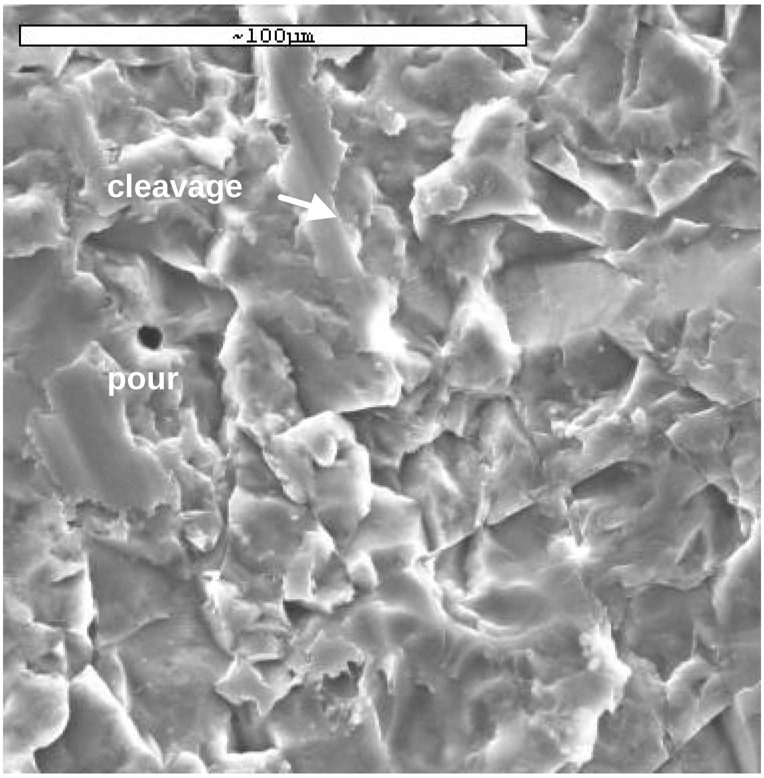

Figure 4.20: SE micrograph of glassy ceramic coating

The results of microstructure measurements of sample S1 are resumed in the Table 4.5.

	zone	**description**	**+++++ (wt.%)**	**++ (wt.%)**	**+ (wt.%)**
Opaque ceramic interface	1	white	Sn	Si and Al	K, Na, Ce, Ti
	2	dark white	Sn, Si		Al, Na, Ce
	3	grey	Si		Al, K, Ti
Glassy ceramic coating	4	light grey	Ti		Al Si, Sn, K
	5	grey	Si		Al, K, Na
	6	black	Si, Al	Ti	K, Na
	7	white	Sn		Al, Si, Na

Table 4.5: Resume of microstructure measurements on sample S1.

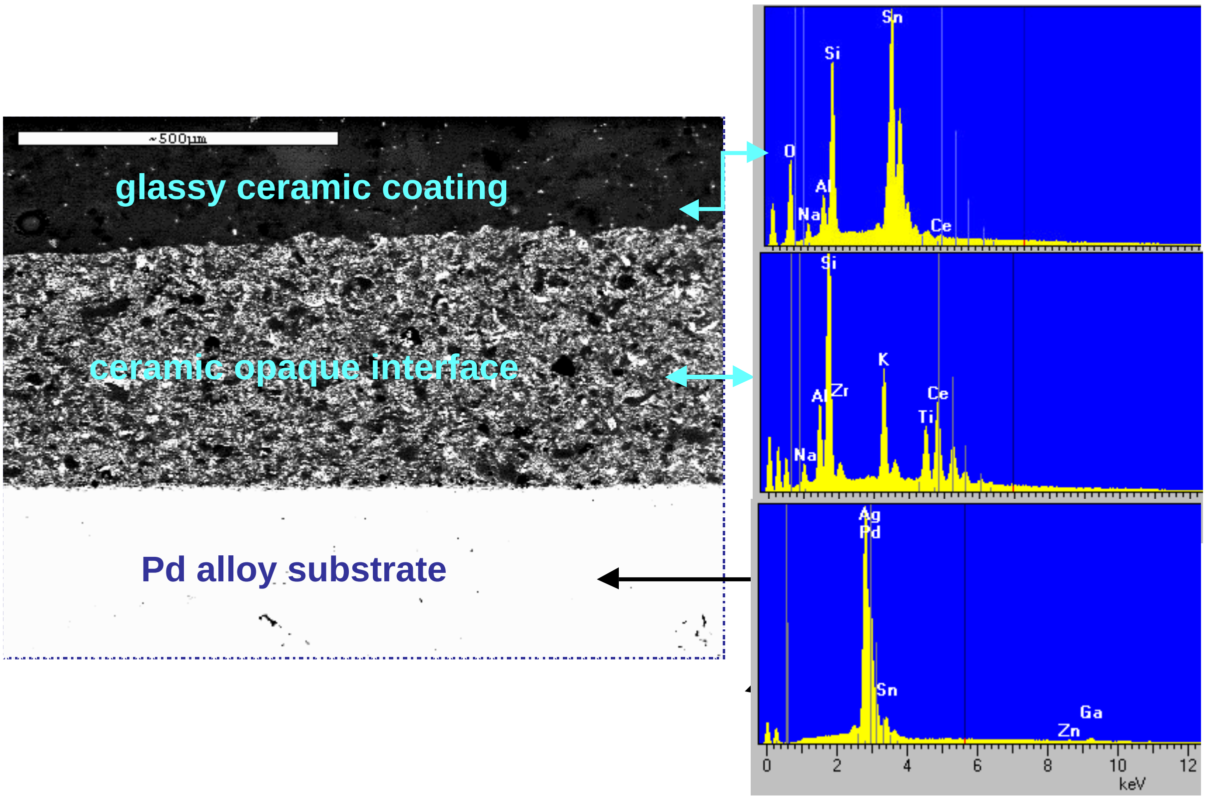

Figure 4.21: Micro-structural analyses: SEM and EDS pattern of palladium region, of interface region and of leucite coating region

4.10 TEM results on S sample - Palladium alloy substrate - and on S1 sample - ceramic coating on Palladium substrate

To investigate the interface and the bulk of sample, the characterisation at the high spatial resolution is needed to understand the kind of defects and growth structures.

TEM analyses were performed on samples prepared by ion milling at glazing angle.

4.10.1 Results on as received Palladium specimen (free of thermal treatments)

When the sample is imaged along [111] direction (Figure 4.22) and [200] direction (Figure 4.23), the dark field images of the lamellas are showed.

It has been taken two diffraction spots before in a zone where the twin appeared bright and then working on matrix there the twins can observed that the structure are modulated. In the bright field images, it could note a high density of twins. Between the lamellas was carried out an X-ray analysis where the observed elements are palladium and tin. This one is in a less percentage than palladium. The same composition was found in the lamellas.

In this case, it is possible to do two hypotheses: crystallographic grow (twin) or chemical origin due to the positioning of tin in the palladium matrix. To understand how of these phenomena is present, elemental-mapping acquisition was performed in the zone 1 and in the zone 2 (Figure 4.24).

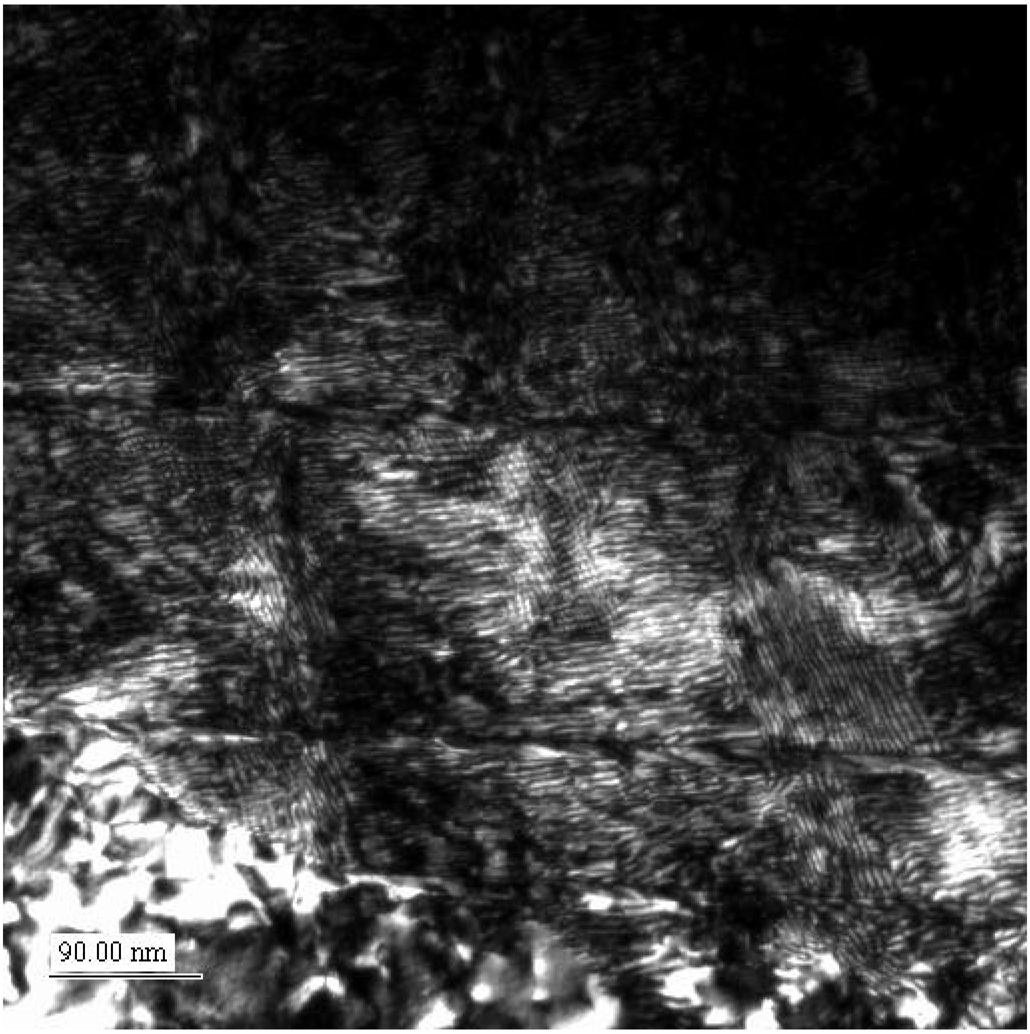

Figure 4.22: Sample imaged along [111] direction.

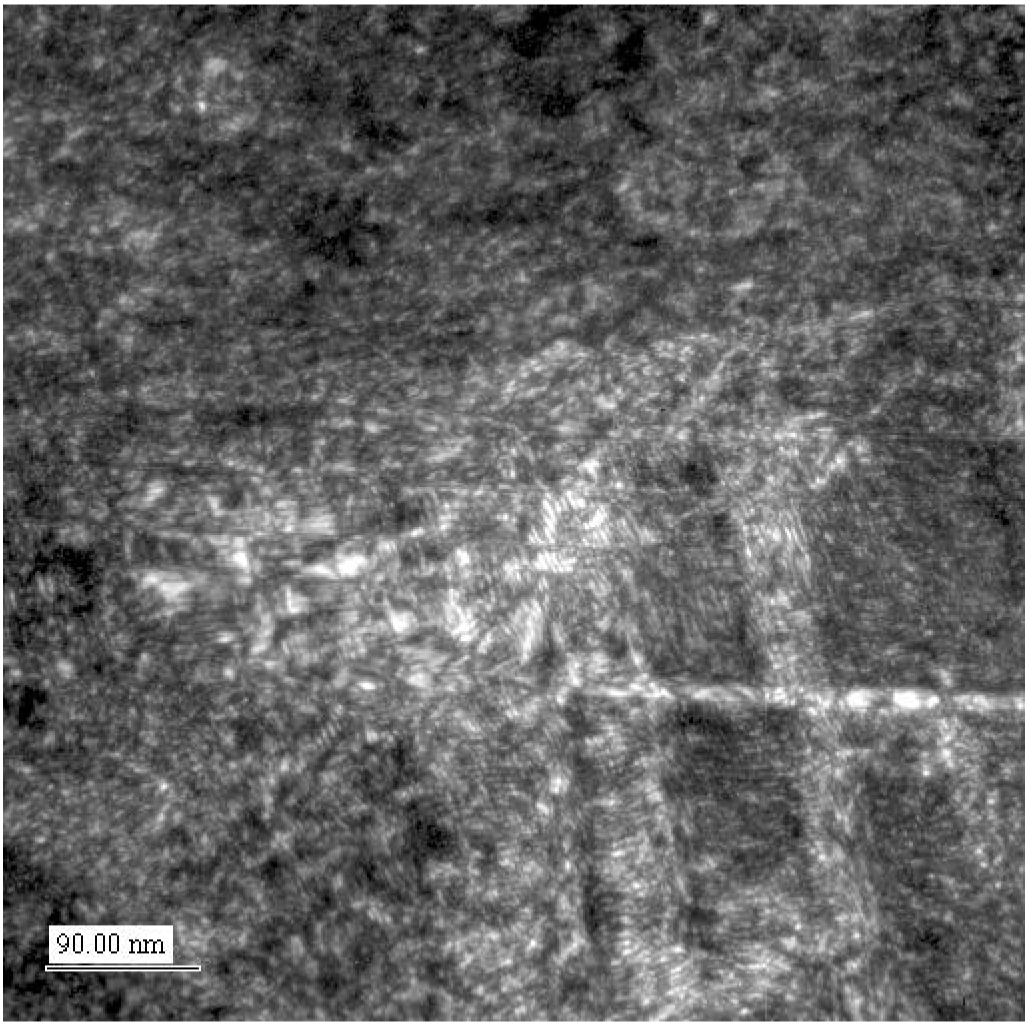

Figure 4.23: Sample S imaged along [200] direction.

There are not different chemical origins, so the different structures are only due to crystallographic origin. The twins' existence (Figure 4.25) depends on the crystal orientation. To verify their existence, it has realised the electron diffraction in these zones where the little spot show the twins and the big spot is the main grain matrix. (Figure 4.24)

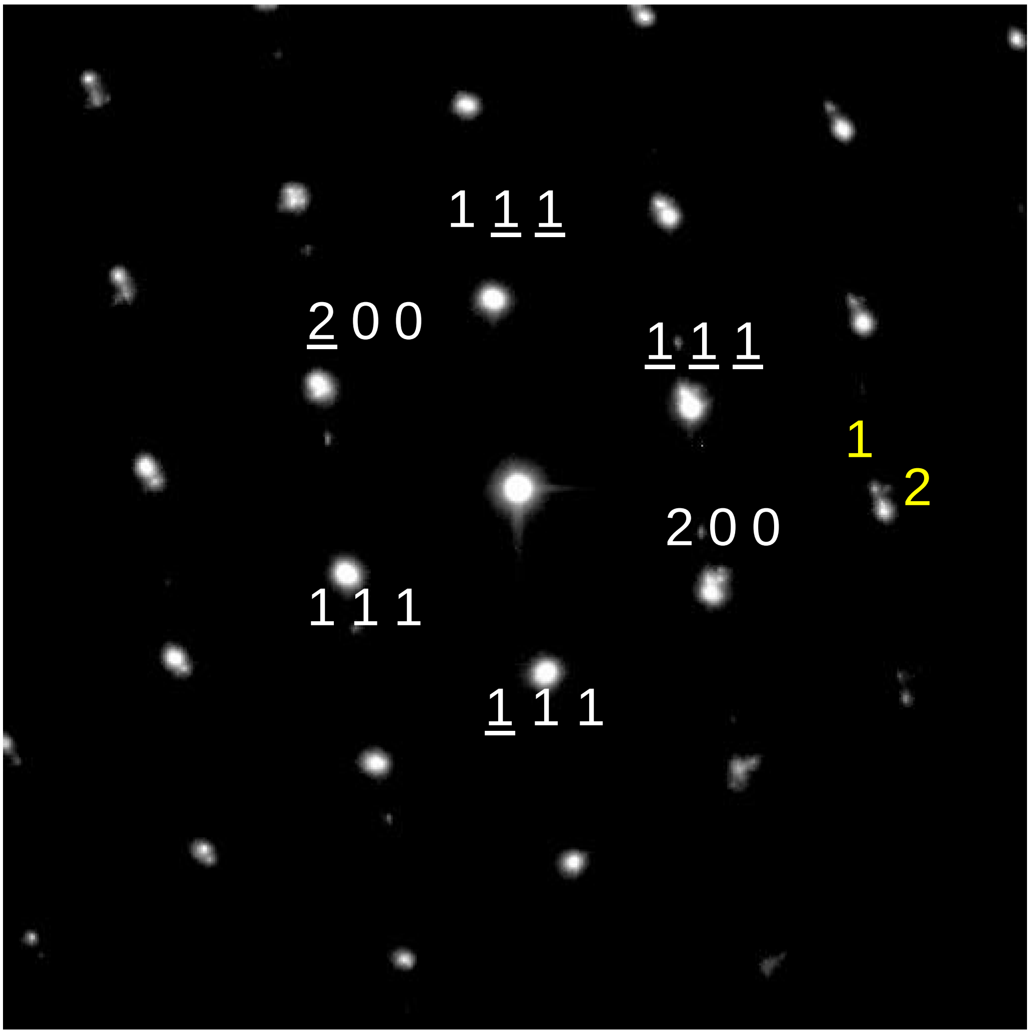

Figure 4.24: Electron diffraction pattern of palladium: 1 - little spot: twin; 2- big spot main grain matrix.

The substrate is a ternary solid solution composed by palladium, silver and tin. The palladium matrix is structurally a solid solution of alloy elements in palladium. The high density of twins in <111> planes is a typical feature of cold deformed CFC alloys. There is twin on all the <111> planes inducing an hardening of alloy, the substitutional atoms too (as Sn) produce hardening of alloy. The presence of tin induces first an expansion of the lattice parameter. This one confirms the results obtained by X-ray diffraction (Table 4.3) on the analysed sample. Second a solid solution hardening.

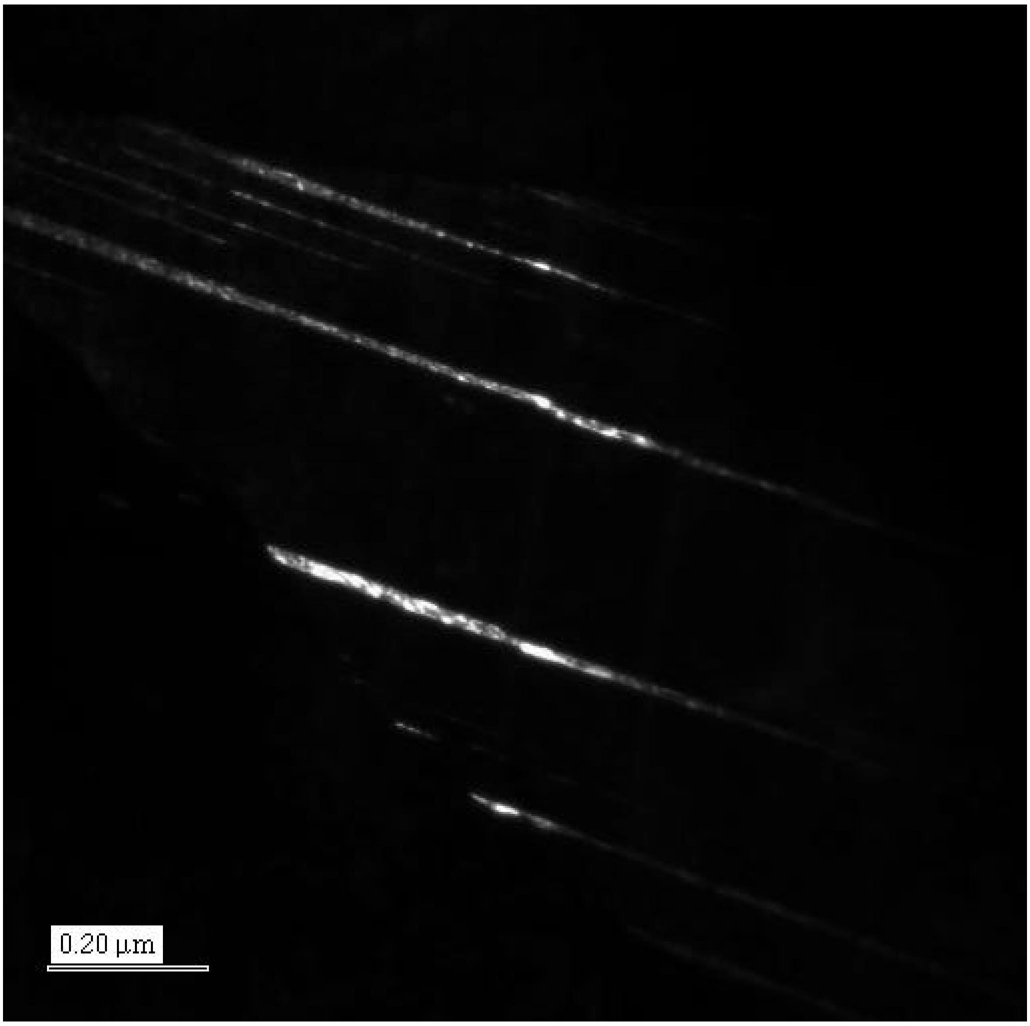

Figure 4.25: Dark field for twins.

4.10.2 Results on as S1 sample

In the S1 sample with palladium and ceramic, the palladium is free of defects as results of high temperature thermal treatment and there are not segregation zones. A good mechanical anchorage is shown at the interface.

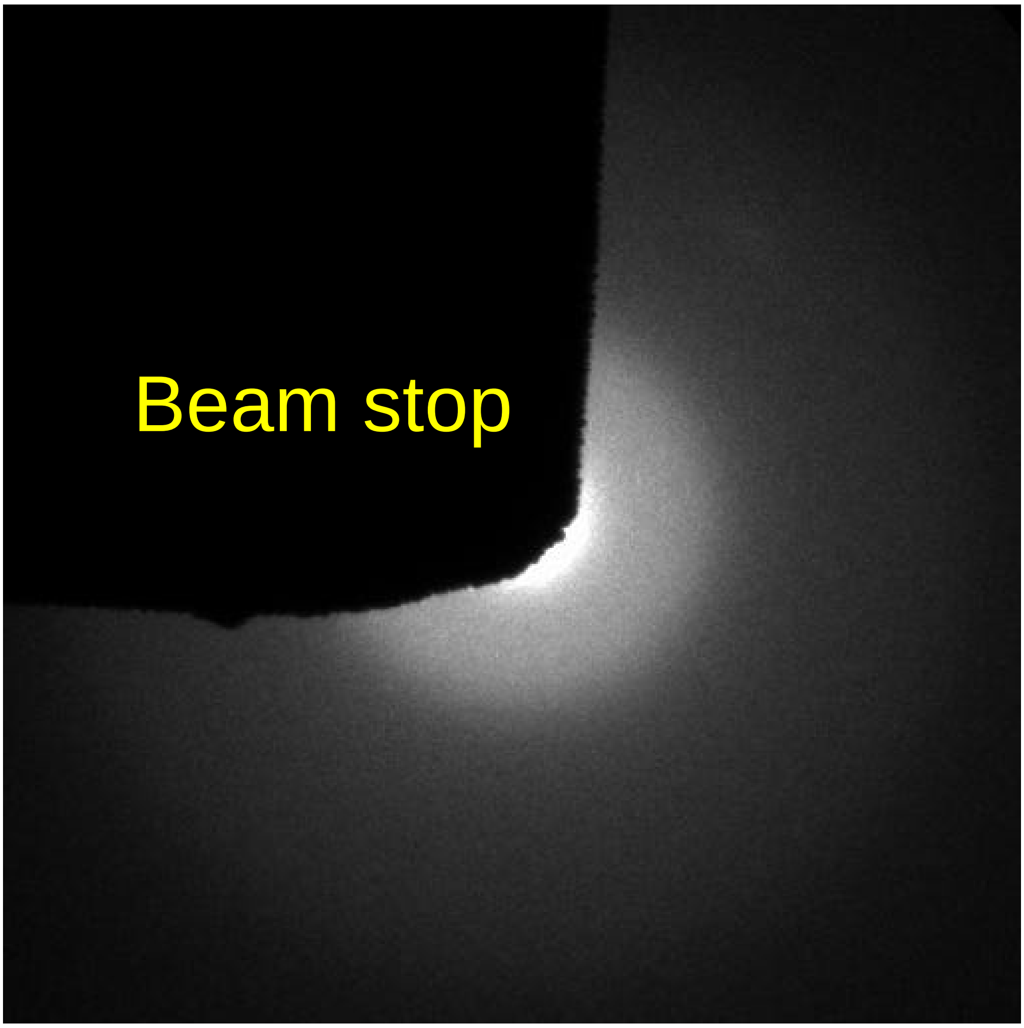

Figure 4.26: Electron diffraction pattern of amorphous in the ceramic interface.

Bright file image (Figure 4.27) shows that opaque ceramic interface is an inhomogeneous material containing controlled - grown microcrystalline phases in a glassy matrix. As it has pointed out in the chapter 1 they are produced by thermal heat treatment of a glass solidified melt. The chemical composition of this melt and the chosen heat treatment conditions determine the type and the amount of crystalline phases in the glassy ceramic. This information is very important for the determination of the residual stresses in the glassy ceramic coating due to its different phases.

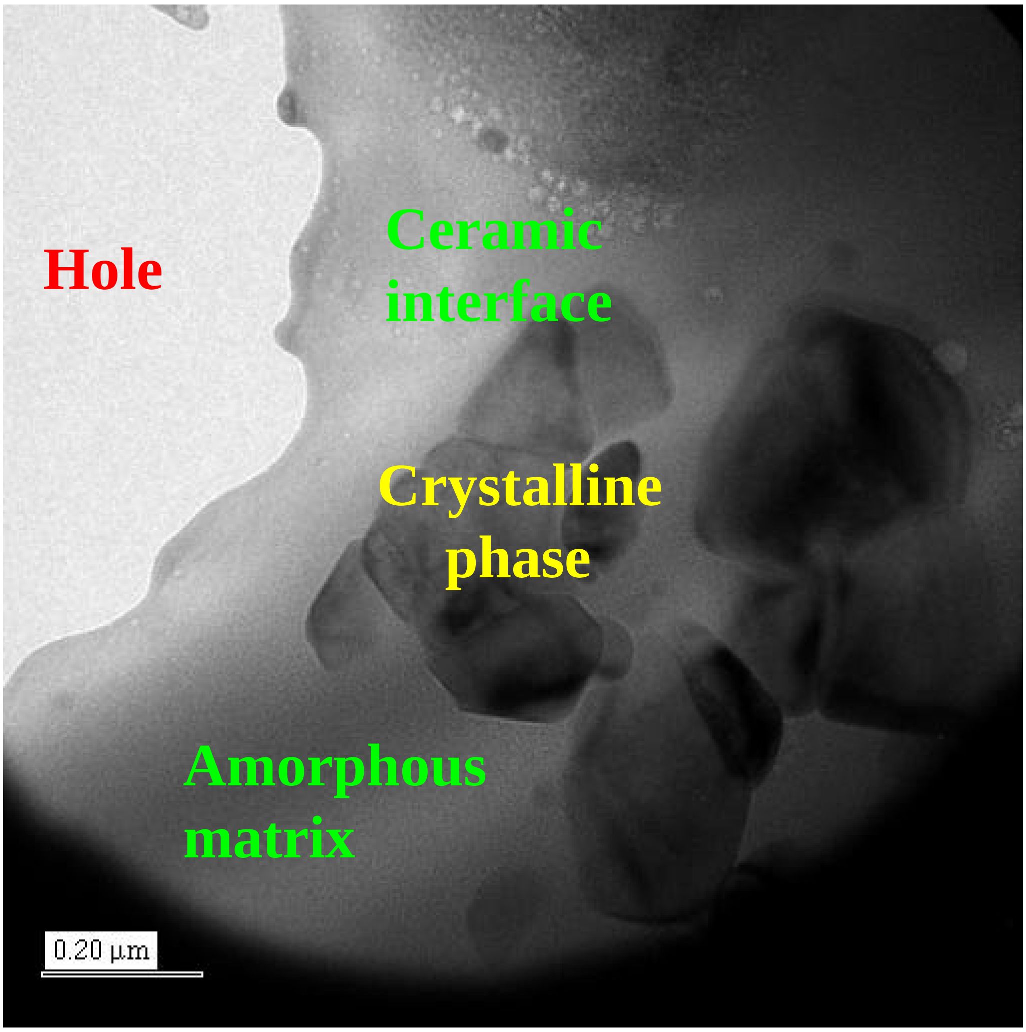

Figure 4.27: Bright field of ceramic interface.

Figure 4.28 and Figure 4.29 are a bright field of opaque interface ceramic zone and of palladium substrate respectively. As from XRD measurements these observations confirm the existence of a great amorphous fraction that is present in the ceramic. The ceramic is inhomogeneous and multiphase, as observed during SEM measurements. In the crystalline regions chemical composition confirm the SEM and XRD results.

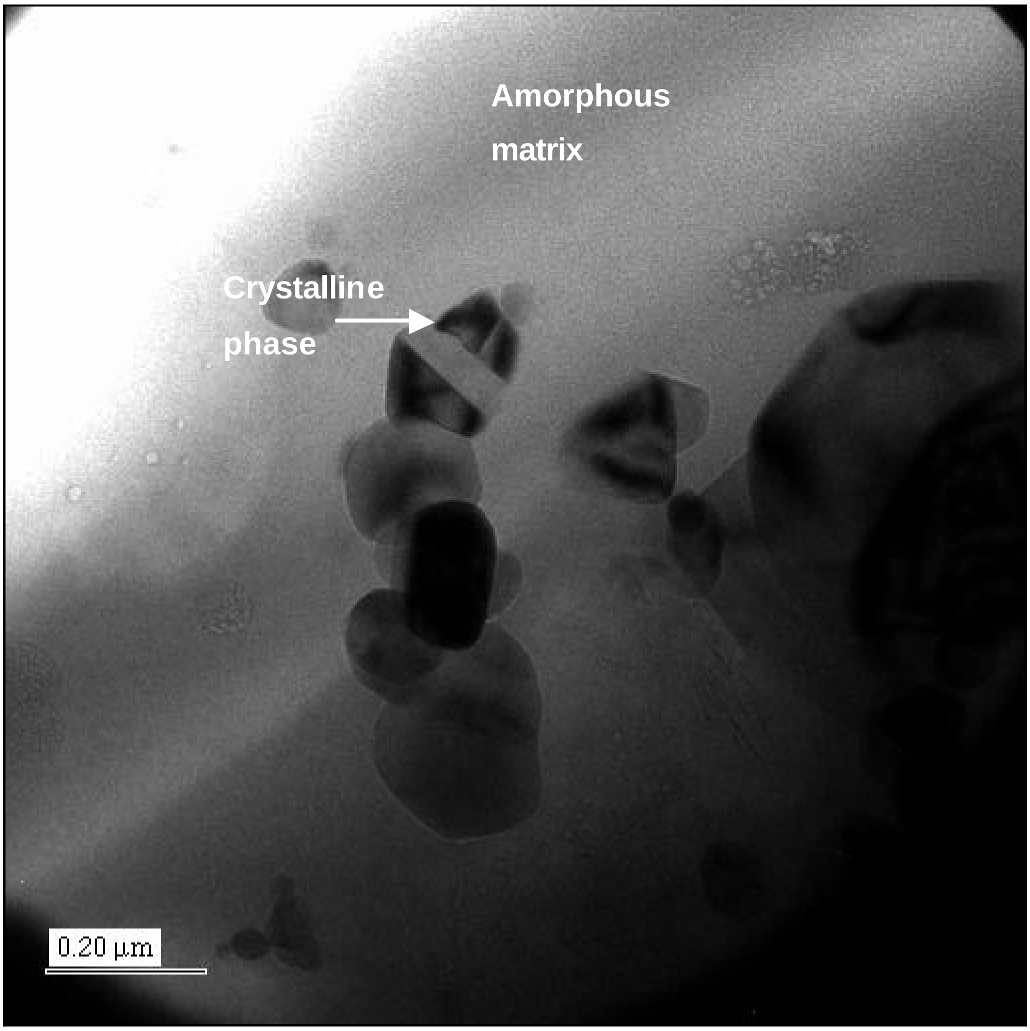

Figure 4.28: Bright field of ceramic interface.

TEM results show the microstructure of opaque ceramic interface that is constituted of crystal of leucite in an amorphous matrix.

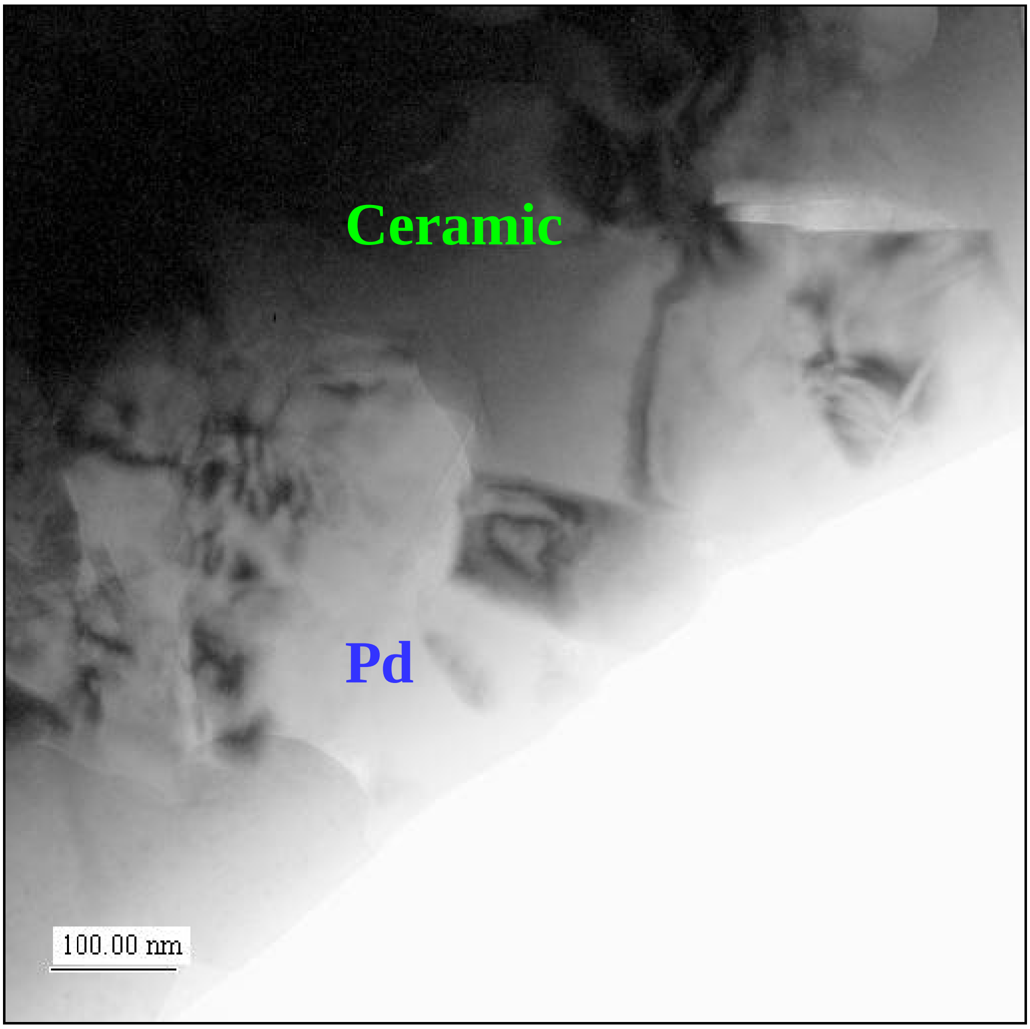

Figure 4.29: Bright field of palladium substrate.

Chemical mapping by EELS (elementary energy loss spectroscopy) shows the presence of a rough interface which can justify mechanical adhesion and does not show strong evidence of elemental inter-diffusion at the interface.

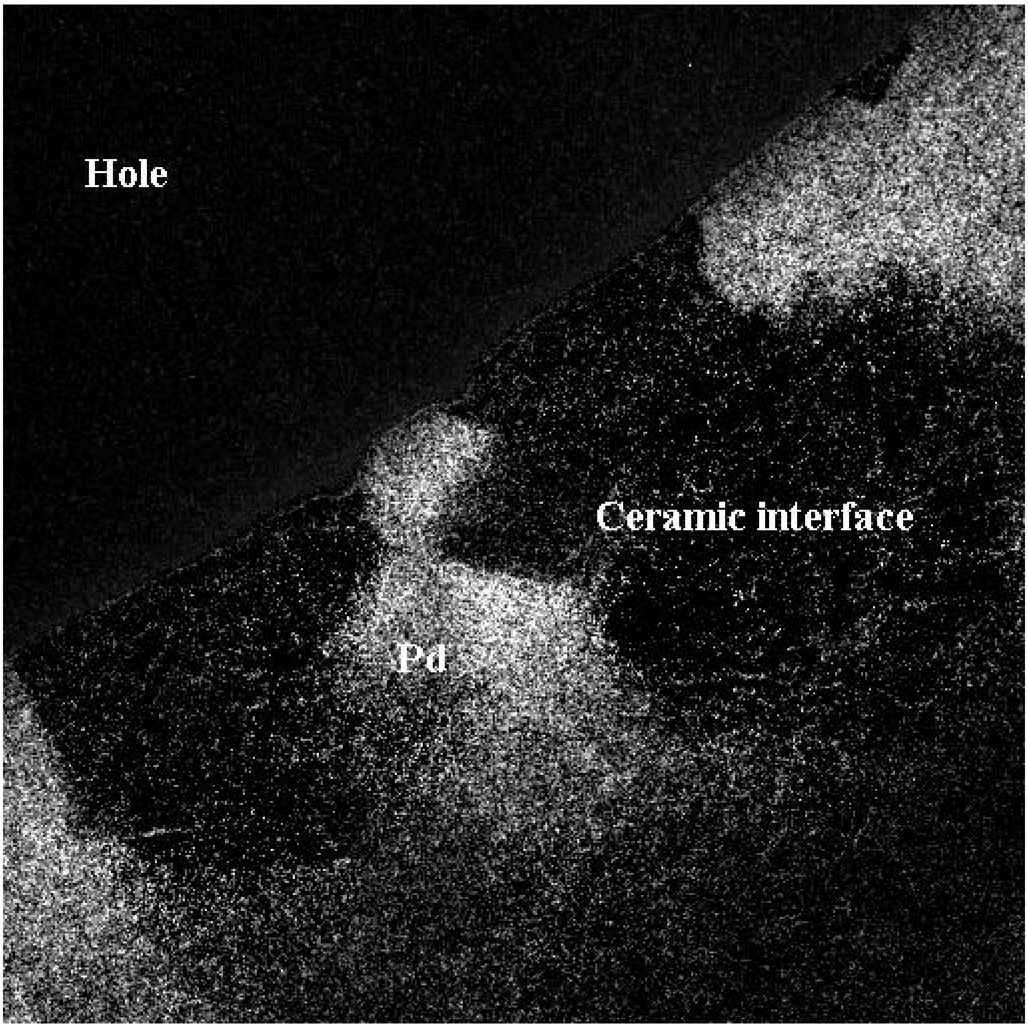

Figure 4.30: Presence of mechanical anchorage.

4.10.3 Conclusion

As it has been discussed before, two bonding mechanisms are possible whereby dental porcelain may be retained to the structure of a metal casting:

- mechanical interaction
- adhesion (chemical bonding)

The principal modes of failure in dental porcelain to metal may be classified as follows:

- failure within the porcelain
- failure at the metal-porcelain interface
- failure within the metal oxide layer. [4.13], [4.14]

Tendency towards failure at the metal-porcelain interface can be reduced by so-called "compression bonding". This arises from the presence of chemical bonding and a slight mismatch in the respective coefficients of thermal expansion of the porcelain and alloy. The composition of the porcelain is such that the thermal expansion of the material is about 5 - 10% less than that of the alloy (the latter being 15 x 10^{-6}/°K, approximately). Cooling the fused porcelain-metal combination results in the metal contracting somewhat more than the ceramic, (too great a mismatch would result in shearing in the chemical bonding). Due to the presence of chemical bonding, the porcelain is subjected to a compressive strain at the interface.

Bonding is normally achieved via a thin transitional metal oxide layer formed on the metal surface by oxidation prior to sealing and also formed in situ during the sealing process by redox reactions between the ceramic and the metallic materials. Undoubtedly, one of the major attributes of dental ceramics is an ability to tailor their thermal expansion characteristics. This can be achieved by careful selection of the starting glass composition and the heat treatment schedule employed to crystallise the glass so that specific crystalline phases are formed.

Glass-ceramics facilitate the manufacture of matched thermal expansion seals and coatings to a very wide range of metals and alloys (Table 4.6). In the sealing process, the glass is initially heated to a temperature high enough to melt the glass and allow it to flow into the metal parts where it wets the surface and reacts to form an interface. In addition to the matching of thermal expansions, it is essential that a chemical bond be formed at the interface between the glass-ceramic and the metal. However, it is also important that any chemical reactions that occur do not result in the formation of undesirable reaction products that change the properties of the glass-ceramic in the interfacial region.
This requires a thorough understanding of the relevant glass-ceramic/metal interactions in order that steps can be taken to minimise reactions that may lead to localised modifications of the glass-ceramic microstructure.

Material	**a_t (°K^{-1}) @25-500 °C**
Cerapall palladium alloy substrate	14 x10^{-6}
Will-Ceram® opaque	13.95 x10^{-}
Will-Ceram® body	13.65 x 10^{-6}

Table 4.6: Thermal expansion coefficients. (Ivoclar Williams)

References

[4.1] B. D. Cullity, Elements of X-ray diffraction (second edition) 1978, Addison-Wesley Publishing Company. Chapters 10 and 11.

[4.2] B. E. Warren, X-ray diffraction, Chapter 7, 1990, Dover Publications, INC. New York.

[4.3] R. E. Lee, Scanning Electron Microscopy and X-ray Microanalysis, 1993, PTR Prentice Hall, Englewood Cliffs, New Jersey.

[4.4] P.J. Goodhew, Practical methods in electron microscopy Vol. 11, Thin foil preparation for electron microscopy, 1985 Elselvier, Amsterdam, N.Y. Oxford.

[4.5] David B. Williams and C. Barry Carter, Transmission electron microscopy. Spectrometry IV.

[4.6] Kushner, 1968.

[4.7] Hugo M. Rietveld, J. Appl. Cryst. (1969). 2, 65-71.

[4.8] Bell, A. M. T.; Henderson, C. M. B.; Cernik, R. Rietveld Studies Of Leucite Analogues J. Materials Science Forum 1996; Issue 228 -231; Number 2, 765-770.

[4.9] Redfern, S. A. T.; Henderson, C. M. B, Monoclinic-Orthorhombic Phase Transition In The K~2mgsi~5O~1~2 Leucite Analogue. American Mineralogist 1996; Vol; 81; Number 3 -4, 369-374.

[4.10] Ota, T.; Matsubara, T.; Takahashi, M.; Hikichi, Y.; Suzuki, Thermal Expansion Of Nepheline-Leucite Ceramic Composites H. Journal- Ceramic Society Japan 1995; Vol 103; Number 5; Issue 1197, 523-524.

[4.11] Music, S.; Zivko-Babic, J.; Mehulic, K.; Ristic, M.; Popovic, S.; Furic, K.; Selinger-Kocijan, D.; Celap, S.; Ivanis, T. Microstructural Properties Of Leucite-Type Glass-Ceramics For Dental Use Croatica Chemica Acta 1997; Vol. 70; Number 2, 703-718.

[4.12] Holand, W.; Rheinberger, V.; Wegner, S.; Frank, M. Needle-Like Apatite – Leucite Glassy Ceramic As A Base Material For The Veneering Of Metal Restorations In Dentistry Journal of Materials Science Materials In Medicine 2000; Vol. 11; Part 1, 11-18.

[4.13] L. Denry, J. A. Holloway, S. F. Rosenstiel, Crystallization kinetics of a low-expansion feldspar glass for dental applications, J Biomed Mater Res, 1998, 41, 398-404.

[4.14] JR Jr Mackert, SW Twiggs, AL Williams, High-temperature X-ray diffraction measurement of sanidine thermal expansion, J Dent Res, Aug 2000; 79(8): 1590-5.

CHAPTER 5

DIFFRACTION MEASUREMENTS FOR RESIDUAL STRESS EVALUATION

5.1 X-ray diffraction stress measurements

X-ray diffraction XRD provides an accurate and well-established, method of determining the residual stress distributions produced by surface treatments. XRD methods offer a number of advantages compared to the various mechanical or the non-linear-elastic (ultrasonic or magnetic) methods currently available for the measurement of near-surface stresses. XRD methods are based upon linear elasticity, in which the residual stress in the material is calculated from the strain measured in the crystal lattice, and are not usually significantly affected by material properties such as degree of cold work or preferred orientation.

XRD methods are applicable to most polycrystalline materials, metallic or ceramic, and are non-destructive at the sample surface.

The shallow depth of penetration of the X-ray beam can be a disadvantage when trying to characterise a subsurface stress distribution with only surface measurements.

X-ray stress measurements were performed on the surface of the Palladium substrate (sample S, Figure 5.1) just before the manufacturing of the coating. The determination of stresses was carried out using a Siemens D500 apparatus. Stress tensors can be determined automatically.

Measurements have been conducted, for that purpose, at Mécasurf Laboratory – E.N.S.A.M in Aix en Provence, with the Cr K_α and Cu K_α radiation. Experimental conditions used are listed in the Table below.

Set-up	**Wavelength (nm)**	0.154 (K_α Cu)	0.229 (K_α Cr)
Parameters	Young's Modulus (MPa)	124 000	
	Poisson's Ratio	0.39	
	Coefficient of Anisotropy	1.7	
	Diffracting Planes	{331}	{311}
	$2\theta_0$ (unstressed Bragg angle °)	147	148
	Data Processing	Biaxial	
Angles	ϕ Angles (°)	0, 90	
	ψ Angles (°)	-37.5, -34.1, -30.5, -26.6, -22.2, -17, -9.7, 0, 13.8, 19.8, 24.5, 28.6, 32.3, 35.8, 39.2	
Acquisition	Acquisition Time per peak (s)	90	
	ψ Oscillations (°)	±3	

Table 5.1: Experimental parameters.

5.1.1 Chemical etching measurements

Chemical etching measurements is a well-known method to evaluate residual stress distribution in depth. It has been realised on palladium alloy substrate. It is important to note that these measurements are the references for the results obtained by synchrotron radiation measurements on sample S.

No precise information was found in literature about the chemical products to use for our alloy; so some test were realised in order to etch the sample. It has been used a solution named “aqua regia” (2 vol. of HCl and 1 vol. nitric acid) which is strongly reactive and toxic product.

The method consists of a step by step chemical removal of superficial layers. At each step residual stress evaluations could be performed. The chemical etching zone was circular with a diameter of 3 mm. To remove 5 µm of material it needed about 30 minutes of continuous sequences of acid deposition (some seconds) followed by washing with a pipette. During these operations, the non-etched surface of the sample was protected by email. This protection layer was then dissolved to define precisely the removed depth. Roughness measurements were used for that purpose to acquire the whole profile of the etched surface. The sample was also examined by optical microscopy to detect eventual corrosion.

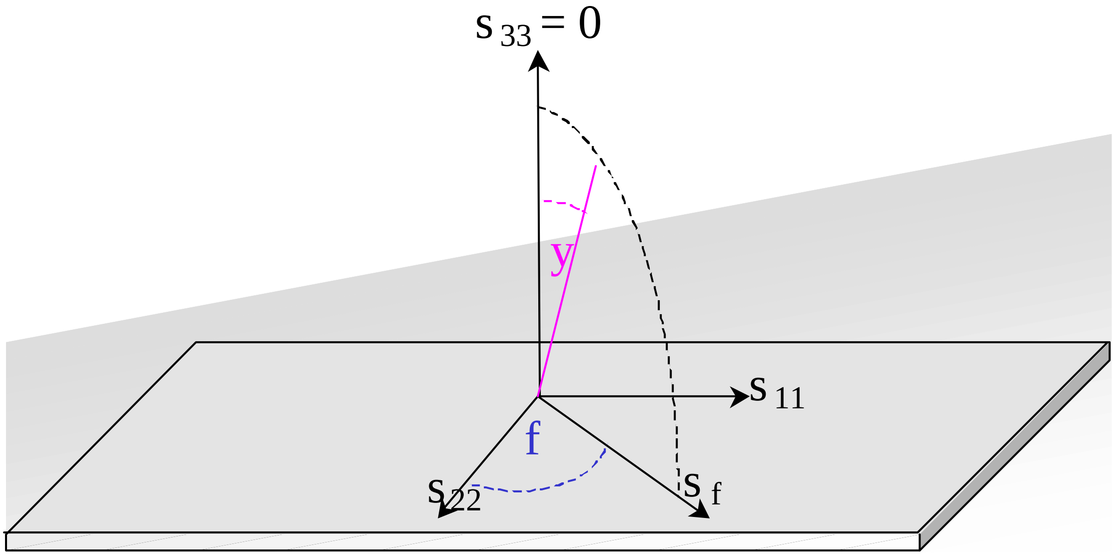

Figure 5.1: Schema of residual stress distribution in sample S.

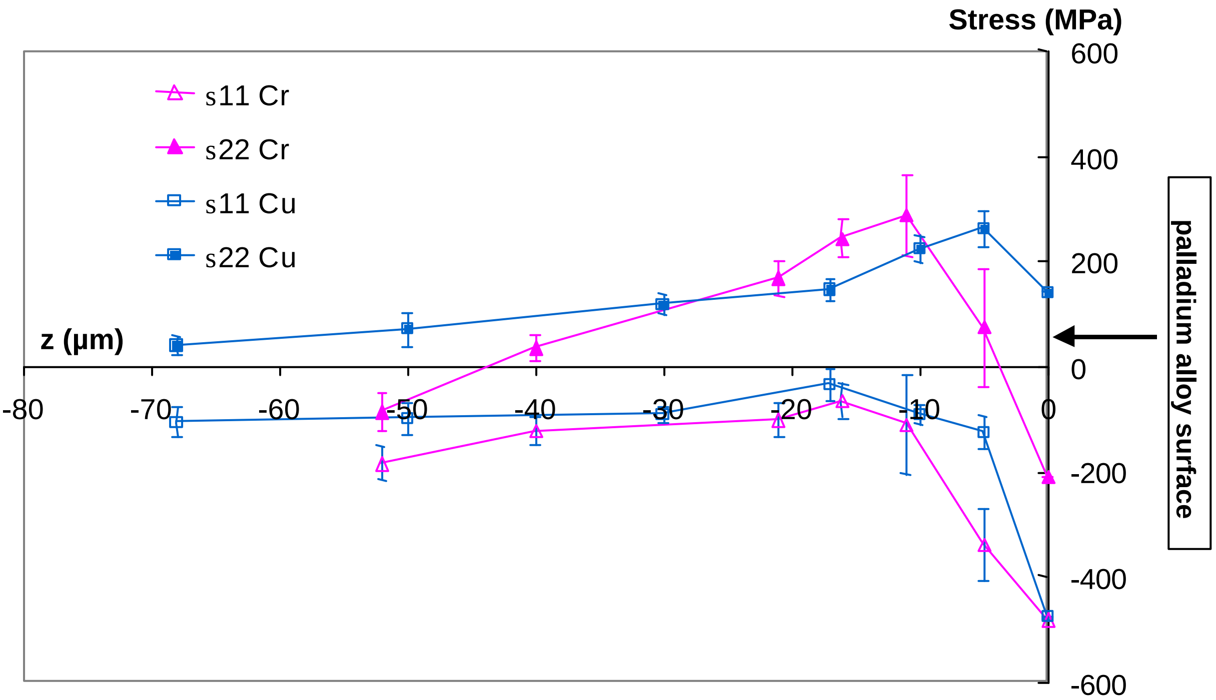

Figure 5.2: Residual stresses in-depth distribution in s_{11} and s_{22} directions.

The in-depth residual stress distribution was estimated through the X-ray $\sin^2\psi$ method. Figure 5.2 shows the longitudinal (σ_{11} component) and transverse (σ_{22} component) stress profiles. No shear stresses have been observed in our sample.

5.2 Neutron diffraction measurements

The principal advantage of neutrons is their greater penetration relative to laboratory X-rays in most materials. Neutrons penetrate on the order of millimetres compared to microns for X-rays. In neutron diffraction method, the strain is measured in the crystal lattice, and the residual stress is calculated, assuming a linear elastic distortion of the crystal lattice.

This chapter is dedicated to the evaluation of residual stresses at surface, in the bulk of materials and at interfaces, by different diffraction measurements of samples S and S1.

The results obtained by neutron diffraction have shown that to analyse near surface measurements or data obtained at the metal/ceramic interface it is necessary to account for some optical aberrations bound to the instrumentation.

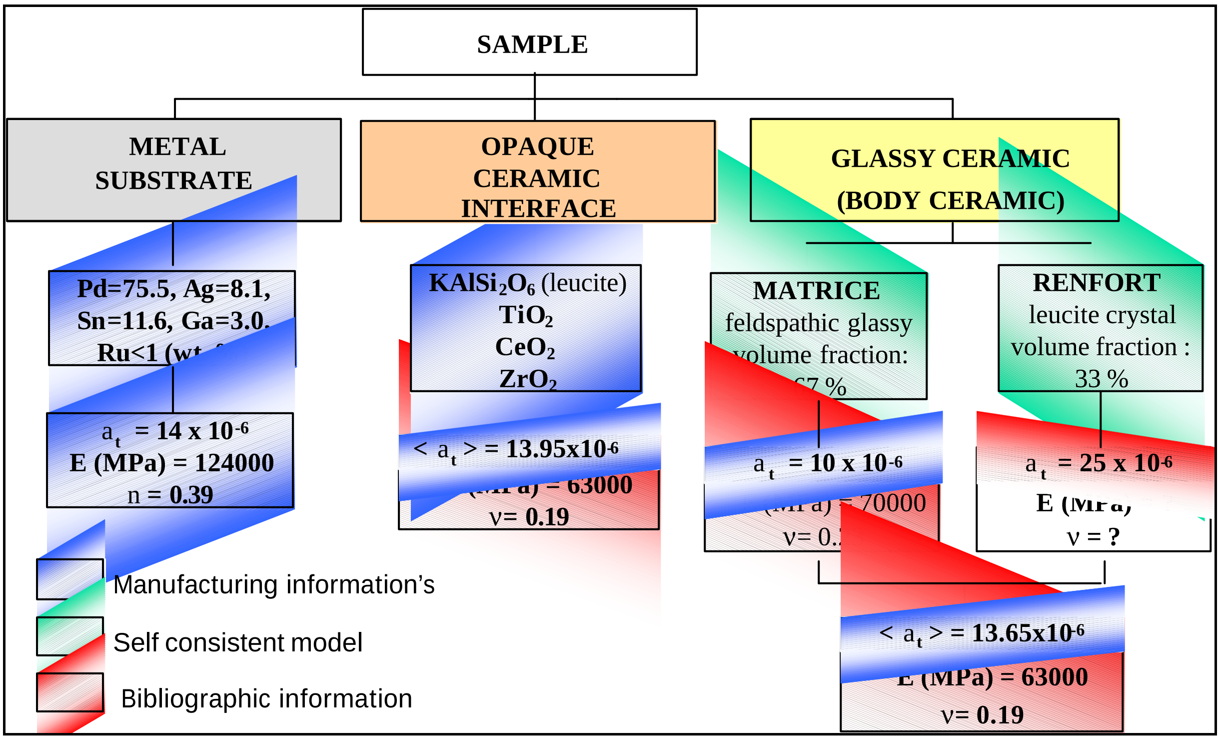

Figure 5.3: Schema of sample S1

5.3 Neutron diffraction measurements on palladium alloy substrate.

As it has already been pointed out, parasitic shifts of the diffraction peaks arise when the neutron gauge volume is not entirely immersed in the studied material. Such impediment is particularly important in the case of near surface measurements.

Evaluation of the stress profiles in the palladium alloy substrate and in leucite coating is thus particularly difficult due to the small thickness of the sample. In fact, to obtain an acceptable diffracted intensity, the neutron gauge volume cannot be less than a few tens of mm^3.

Due to the great difference of the lattice parameters of the palladium and the leucite (Table 5.2), these two constituents could not be characterised on one single neutron instrument. For the ceramic a great wavelength is required (> 0.4 nm). The experiments have been carried out therefore on G5.2 at LLB (Saclay, F), using cold neutrons. For the palladium substrate, the measurement conditions are more classical. The experiments have been carried out on E3 at HMI (Berlin, D) and on D1A at ILL (Grenoble, F).

Definition	**Lattice parameter (nm)**
Leucite coating	Tetragonal a = b = 1.309 c = 1.375
Palladium alloy substrate	CFC a = 0.395

Table 5.2: Lattice parameters of leucite and palladium alloy.

5.3.1 Neutron diffraction measurements on HMI-BENSC

The bulk of the metallic substrate has been studied at the E3 diffractometer of the HMI-BENSC (Figure 5.5). The experimental conditions are reported in Table 5.3.

Set-up	Equipment	E3 two-axis diffractometer
	Monochromator	{220} Cu
	Detector	multideterctor
	Primary slit (mm^2)	1.5 x 10
	Secondary slit (mm^2)	1.5 x 10
Parameters	Wavelength (nm)	0.137
	Diffracting plane	{331}
	Unstressed Diffraction angle (°)	99
	Data processing	triaxial

Angles	ϕ Angles (°) ψ Angles (°)	0, 90 0, 30, 60, 90
Stress	Longitudinal and transverse components	σ_{11}, σ_{22}

Table 5.3: Experimental parameters HMI.

The neutron gauge was set to 1.5 × 1.5 × 10 mm^3. Due to low diffracted intensity, it was not possible in a reasonable time to obtain valid results for positions nearest the interface than 300 µm. The triaxial method has been used to evaluate the stresses in the longitudinal (σ_{11}) and transverse (σ_{22}) directions of the sample. These measurements have been carried out in ω mode with four ψ incidences (0°, 30°, 60° and 90°).

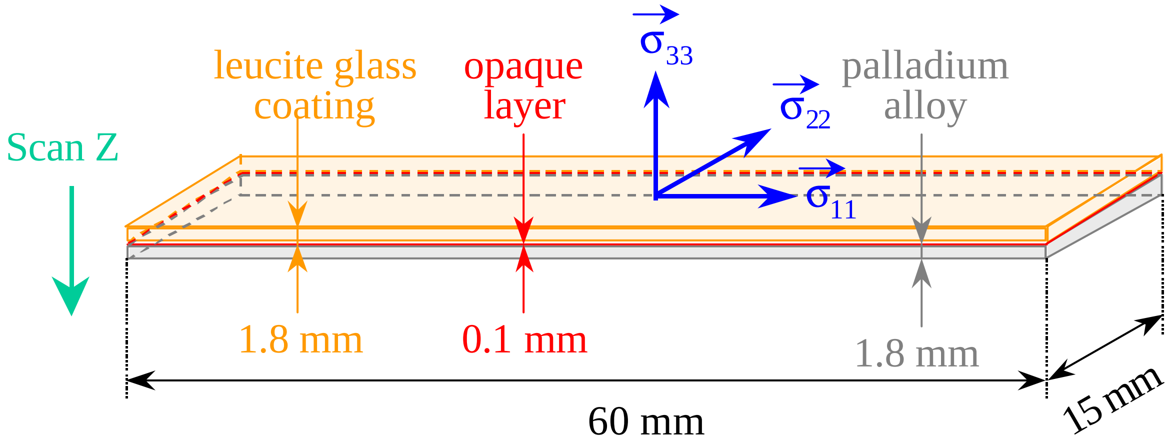

Figure 5.4: Schema of residual stress distribution in sample S1.

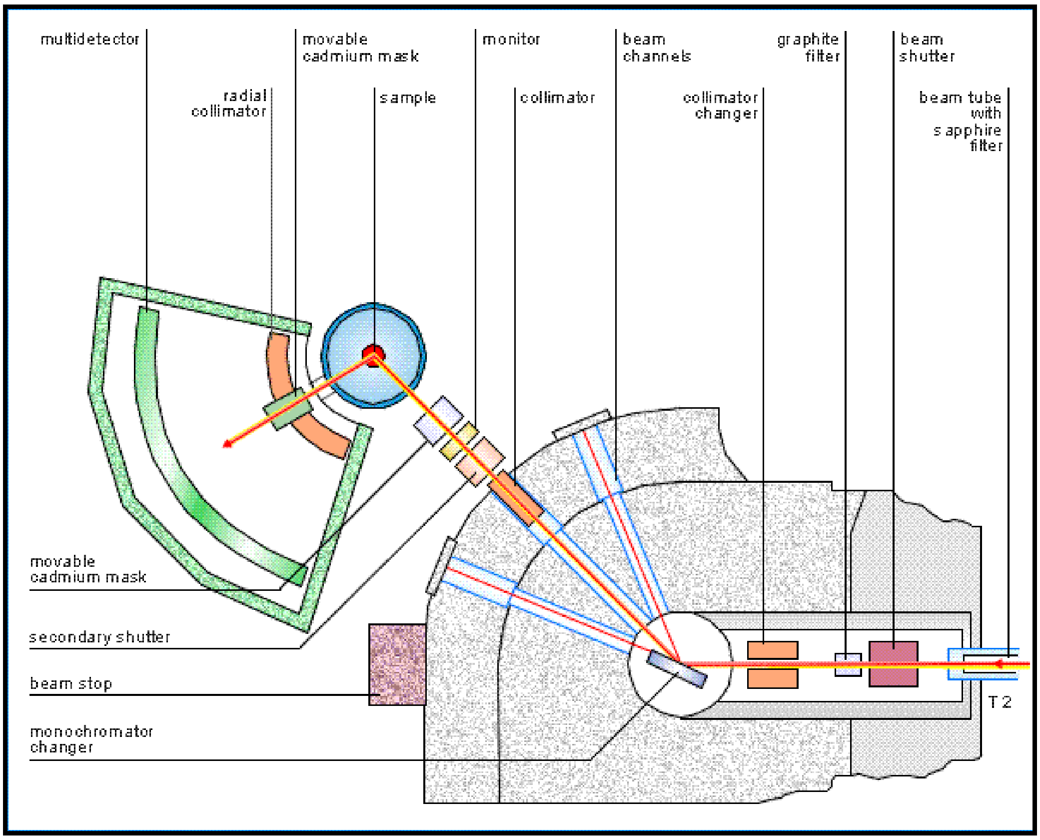

Figure 5.5: Layout of the E3 diffractometer at HMI-BENSC.

The depth affected by the stresses remains low in comparison to the size of the neutron beam. It is therefore necessary to localise very precisely the true position of the neutron gauge inside the sample. This is obtained through a strain scanning across the studied interface. The true position of the neutron gauge volume is then derived from the evolution of the diffracted intensity versus the scanned depth. Such a curve can be defined experimentally or theoretically through the Monte Carlo simulation program. The results obtained for Ψ= 90° in transverse direction, are presented in Figure 5.6.

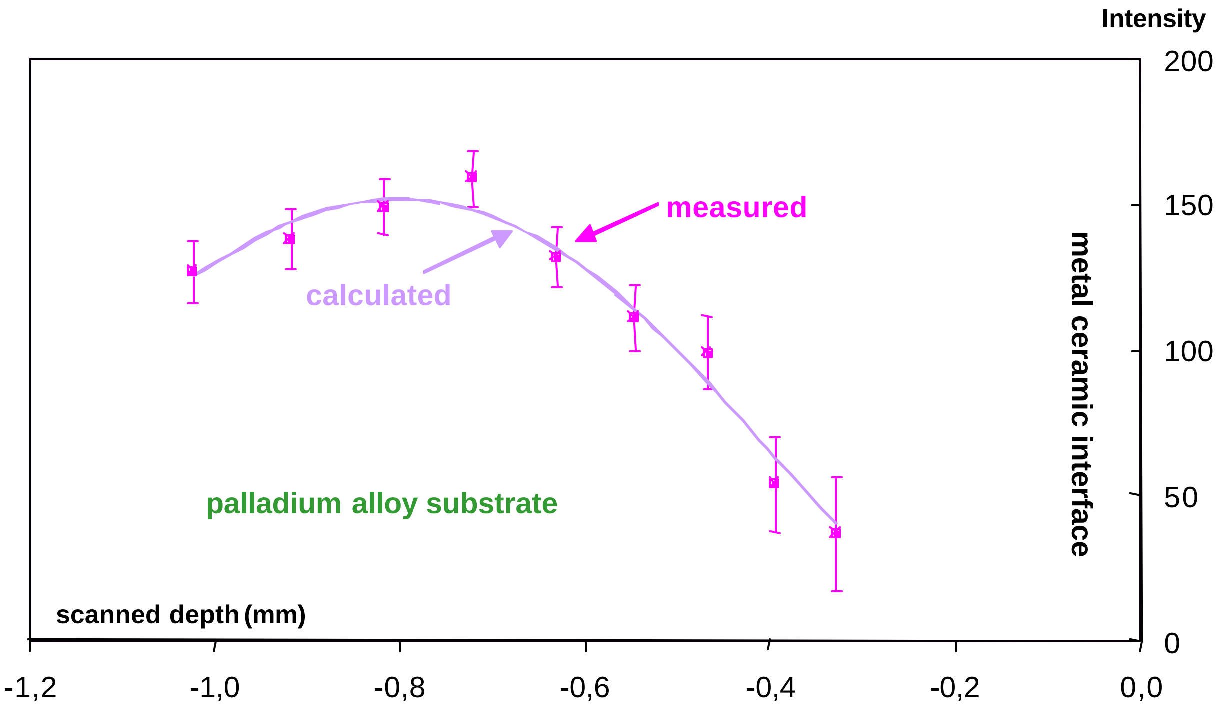

Figure 5.6: Distribution of the diffracted intensity versus the scanned depth (see §3.3).

The intensity increases when the neutron probe enters into the sample and finally decreases due to the absorption of the neutrons by the material. For these curves, the depth z of each scan is defined by the position of the centre of the neutron probe. The position z = 0 is thus obtained when half the neutron probe is immersed in the sample. The intensity obtained at this point is then usually assumed to be half the maximum intensity. Our numerical simulations question this. In fact, the theoretical results show that half the maximum intensity is obtained for a depth of about 0.5 mm. This depth slightly varies with Ψ. For that reason, the true position of the neutron probe has been defined for each Ψ direction by an adjustment of these theoretical curves to the experimental results. This allows defining the position of the neutron probe with an accuracy of about 50 µm.

The in-depth stress profiles of the first layer of Palladium are derived from the diffraction-peak positions obtained for the different Ψ incidences.

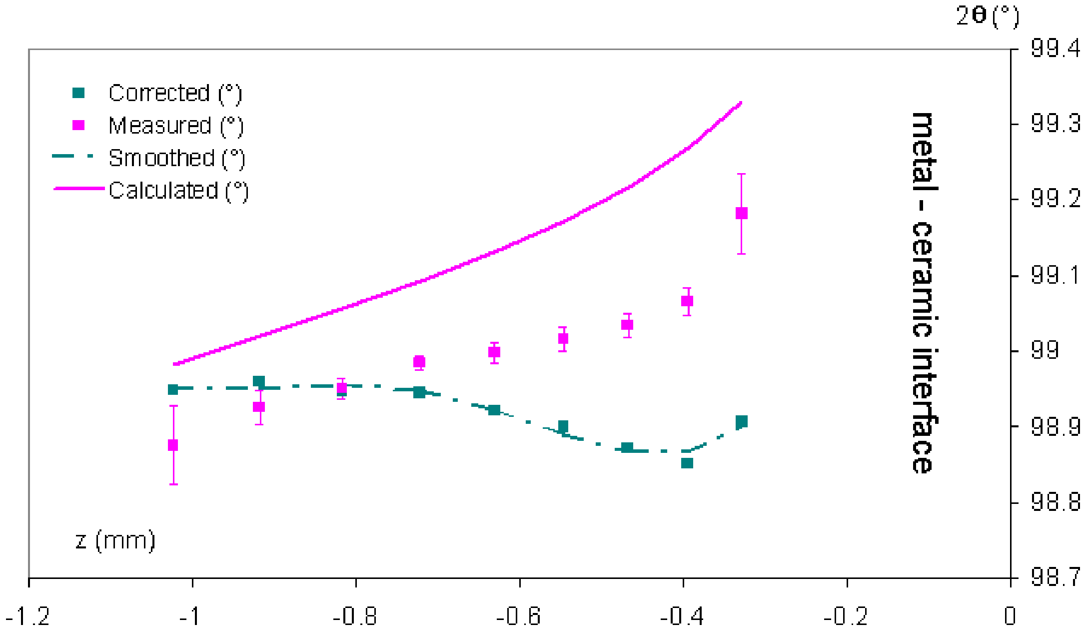

Figure 5.7: Distribution of the diffraction peak position versus the scanned depth. These curves show that a great part of the peak shifts observed experimentally is due to the geometrical errors.

Figure 5.7 shows the distribution of the peak position versus the scanned depth obtained for ψ= 0° direction. The calculated values correspond to the parasitic peak shifts that are obtained with an unstressed specimen when the neutron probe is not entirely immersed in the sample. The measured values are the results obtained experimentally on the true surface layer. These curves show clearly that a great part of the peak shifts observed experimentally is due to the geometrical errors and has to be corrected. This has been done for the stress evaluation. Moreover, the true depth analysed by the neutrons has to be computed. It corresponds to the centre of the diffracting volume (the intersection between the neutron probe and the sample).

For each ψ inclination, the Monte Carlo simulation program has defined the relation between this last distance and the scanned depth (which is defined by the centre of the neutron probe). These curves account for the absorption of the neutrons by the material and for the local conditions of diffraction.

Reliable stress results could be obtained finally for both the bulk of the Palladium substrate and for the superficial layers located at depths between 350 µm (which is ten times smaller than the width of the neutron probe) and 900 µm from the interface. The stresses are very low (Figure 5.8).

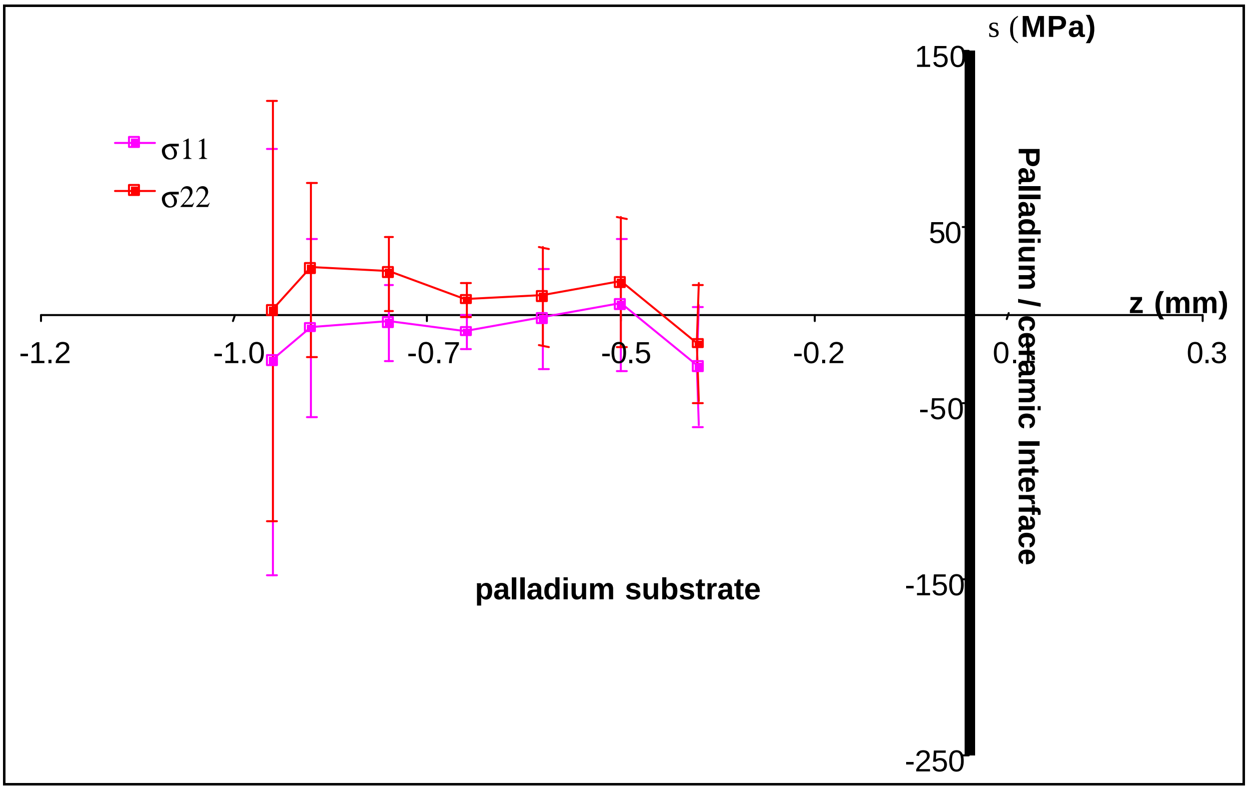

Figure 5.8: In-depth distribution of residual stresses versus the z scanned depth.

5.3.2 Neutron diffraction measurements on ILL

On palladium substrate some measurements have been performed at the D1A diffractometer of the ILL. Neutrons coming from the 40 MW ILL reactor are monochromised by a Germanium crystal, and the diffraction peak is recorded in a position sensitive detector (PSD) (Figure 5.9). On this facility the neutrons flux is much greater than at HMI. In Table 5.4 are reported the experimental conditions.

A small neutron gauge volume was selected. With such a condition, the stresses could be characterised until 60 µm from the interface. The triaxial method has been used to evaluate the stresses in the longitudinal and transverse directions of the sample. HMI results have been confirmed. The stresses are mainly tensile, but very low (Figure 5.13).

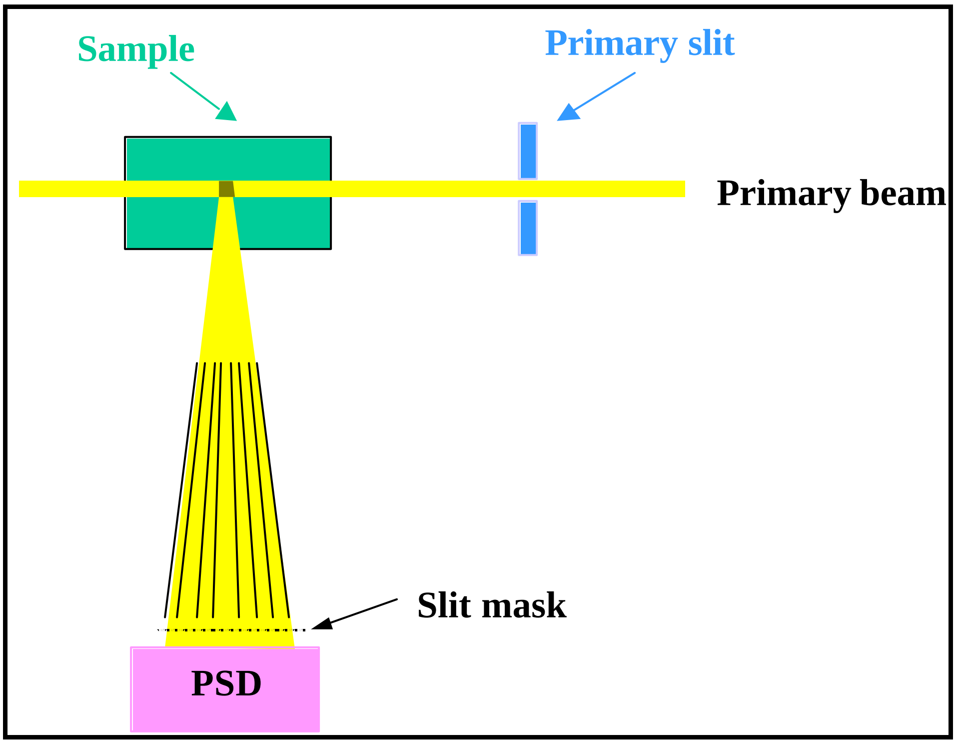

Figure 5.9: Layout of the D1A diffractometer at the ILL, Grenoble.

Set-up	Equipment Monochromator Detector Primary slit (mm^2) soller Secondary slit (mm^2) soller	D1A two-axis diffractometer {115} Ge PSD 0.5 x 10 0.5 x 10
Parameters	Wavelength (nm) Diffracting plane Unstressed Diffraction angle (°) Data processing	0.19114 {311} 105.85 triaxial
Angles	ϕ Angles (°) ψ Angles (°)	0, 90 90
Stress	Longitudinal and transverse	σ_{11}, σ_{22}

Table 5.4: Experimental parameters ILL.

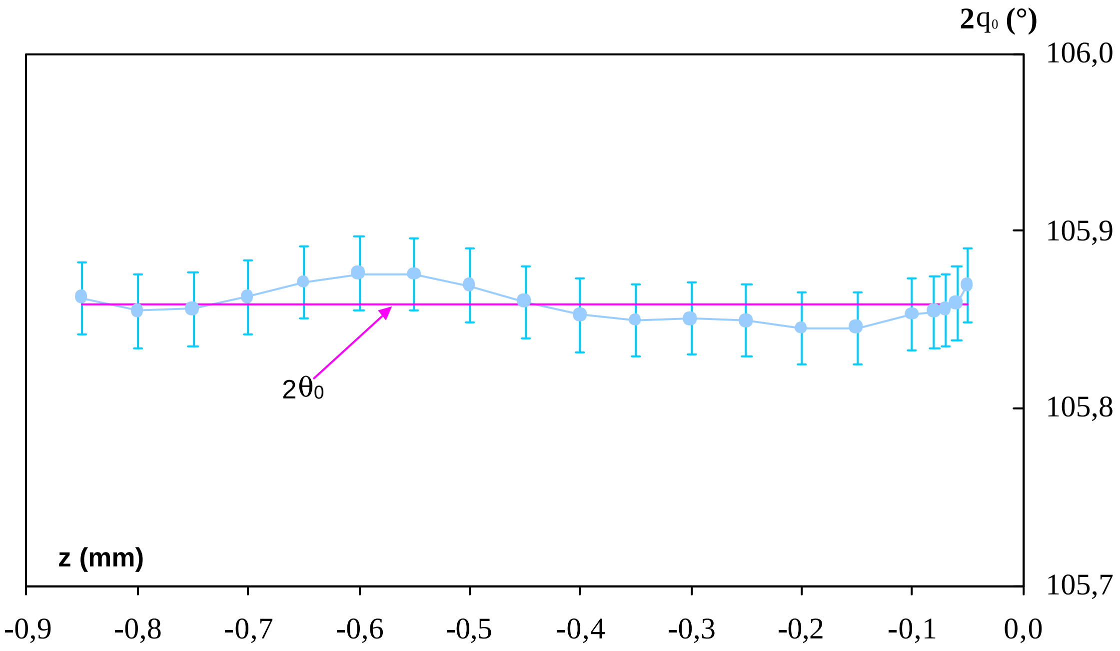

Figure 5.10: Distribution of the diffraction peak position versus the z scanned depth.

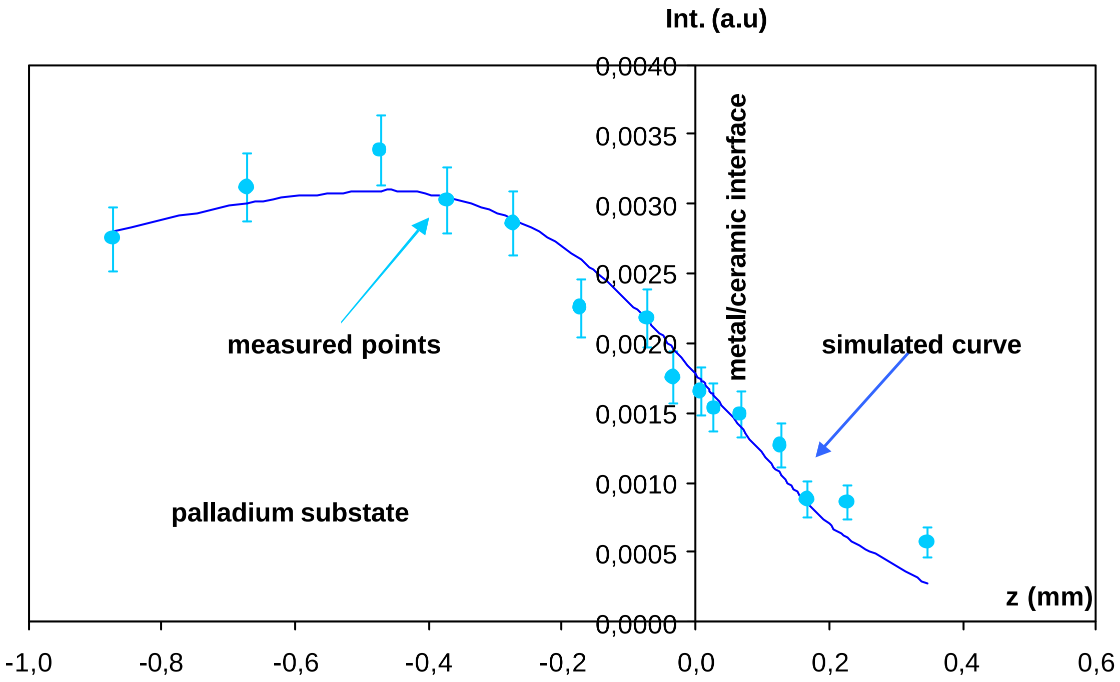

Figure 5.11: Distribution of the diffracted intensity versus the z scanned depth.

As explained in chapter 2, the stresses were calculated assuming a biaxial stress state (σ_{33}=0). This condition allows estimating the Bragg angle for the unstressed material. This parameter was found constant in the whole analysed depth (Figure 5.10). This confirms the plane stress assumption.

In the Figure 5.11 is shown the distribution of diffracted intensity versus scanned depth. The experimental points match very well the simulated (Monte Carlo) curves. As it has been pointed out the true position of neutron gauge volume has obtained by the evolution of diffracted intensity in function of scanning depth (Figure 5.12).

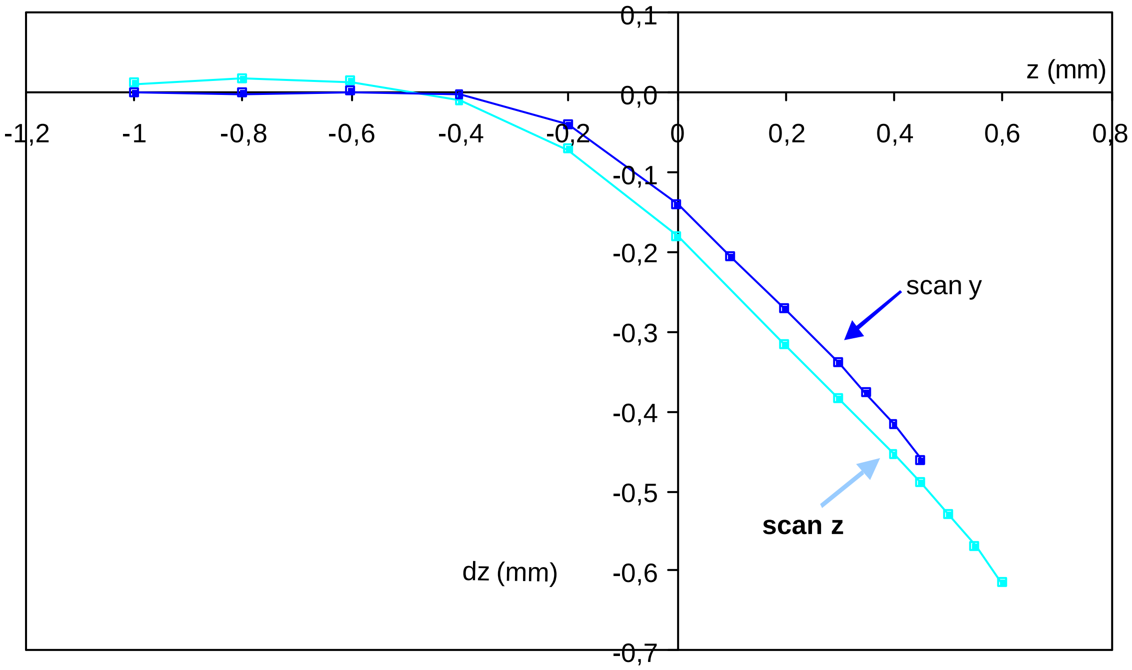

Figure 5.12: Relation between z and dz[XX].

[XX] In our method we distinguish different Z:

- Z_{true}: position of the barycentre of the diffracting volume, which takes into account of physical phenomena (dispersion of wavelength) and geometrical problems.
- $Z_{goniometre}$: position of the " geometrical " barycentre of volume probes, such as it is defined by the coder of the goniometer,
- dZ: distance between Z_{true} and $Z_{goniometre}$.

We are interested in the barycentre of diffracting volume i.e. of the part of the volume probes which penetrates inside the sample.

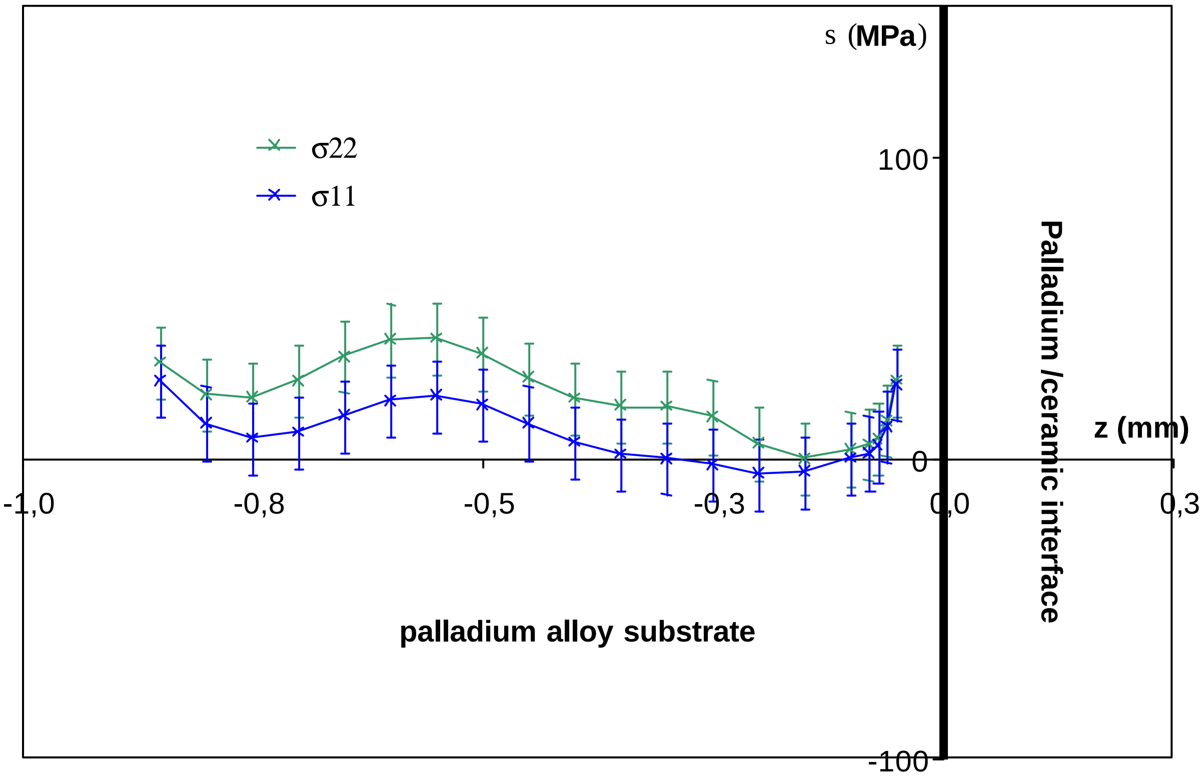

Figure 5.13: In-depth distribution of residual stresses as characterised by neutron diffraction.

5.3.3 Neutron diffraction measurements at LLB G5.2 on WilliamsÒ leucite coating.

The basic goal of this experiment was to obtain essential information of the stresses in PMF-leucite coated on palladium alloy sample.

Due to the great lattice parameters of the leucite, cold neutrons have been used to study this constituent. The experiments have been carried out at the research reactor Orphée of Laboratoire Léon Brillouin (LLB - CEA Saclay) on G5.2, the two axis diffractometer dedicated to the evaluation of residual stresses and equipped with a position-sensitive detector (Figure 5.14). The $\sin^2\psi$ method has been used to evaluate the stresses. These measurements have been carried out in ω mode with four independent ψ incidences 0°, 30°, -40°, -15°. In Table 5.5 are reported the experimental conditions.

Set-up	Equipment	G52 two-axis diffractometer
	Monochromator	{002} graphite
	Detector	PSD
	Primary slit (mm^2)	1 x 35
	Secondary slit (mm^2)	0.8 x 35
Parameters	Wavelength (nm)	0.4506
	Diffracting plane	{004}
	Unstressed Diffraction angle (°)	82
	Data processing	$\sin^2\psi$
Angles	ϕ Angles (°)	90
	ψ Angles (°)	0, 30, -40, -15
Stress	Transverse	σ_{22}-σ_{33}

Table 5.5: Experimental parameters LLB.

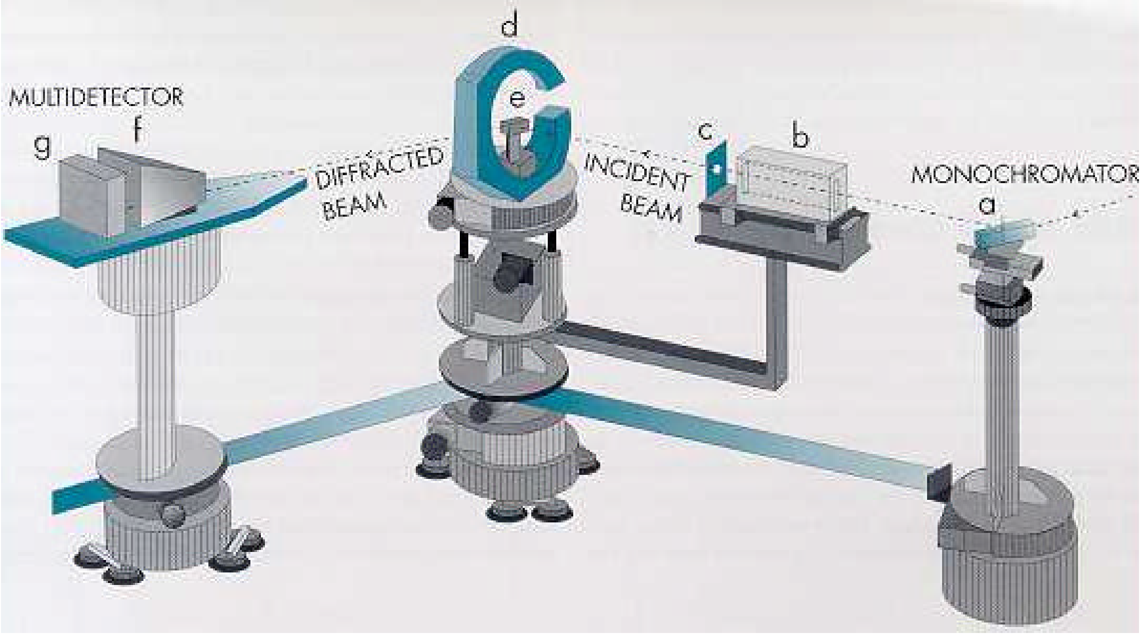

Figure 5.14: Layout of the G5.2 diffractometer at the LLB, Saclay.

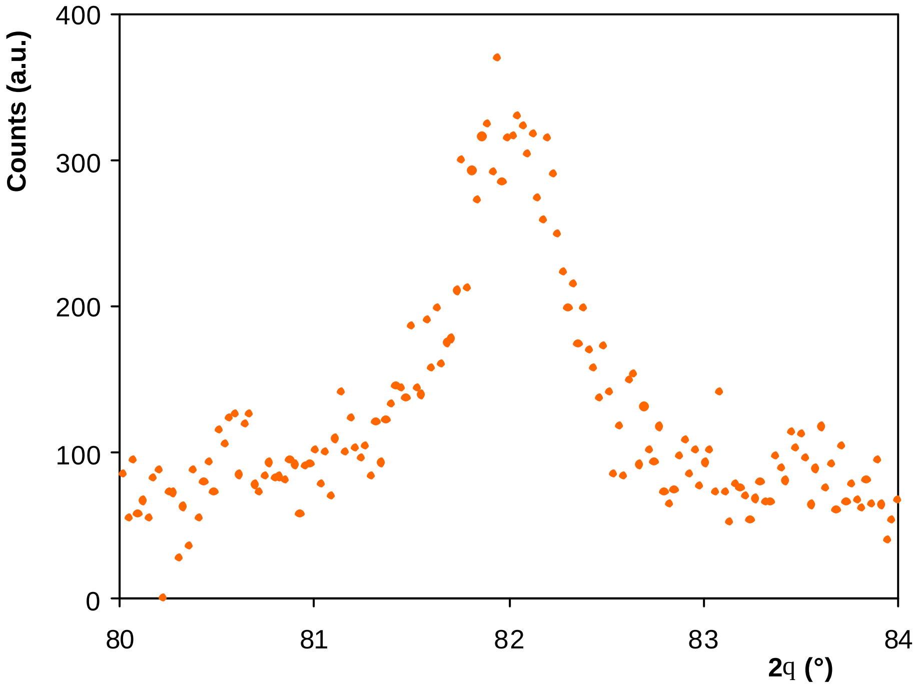

Figure 5.15: An example of experimental diffraction peak.

Residual stress profile was determined with help of the simulation Program.

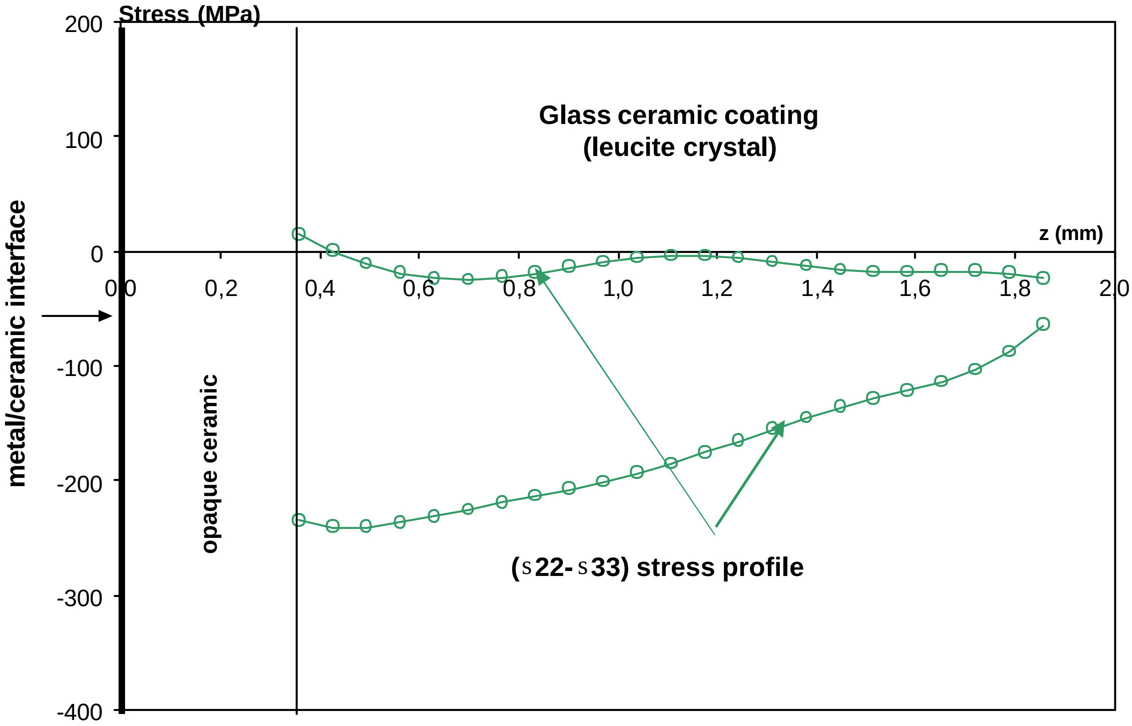

Figure 5.16: In-depth distribution of residual stresses versus scanned depth. These two curves σ22-σ33 represent the maximum and minimum value between the residual stress can found.

The in-depth stress profiles of the leucite coating are derived from the diffraction-peak positions obtained for the different ψ incidences.

5.3.4 Evaluation of the absorption coefficient of leucite

The data simulation and analysis requires knowledge of the attenuation coefficient of leucite. Two different tests were realised for evaluating this coefficient.

- **Evaluation of leucite absorption coefficient on G5.2 LLB**

The absorption coefficient of a leucite powder (P2) was first measured at G5.2 LLB by a powder diffraction method. It was realised in the same measurement condition than for the stress evaluations, performing a scan with a step of 0.500 mm in eight different positions. The absorption coefficient found is $\mu = -0.308$ (for $\lambda = 0.4506$ nm) (Figure 5.17).

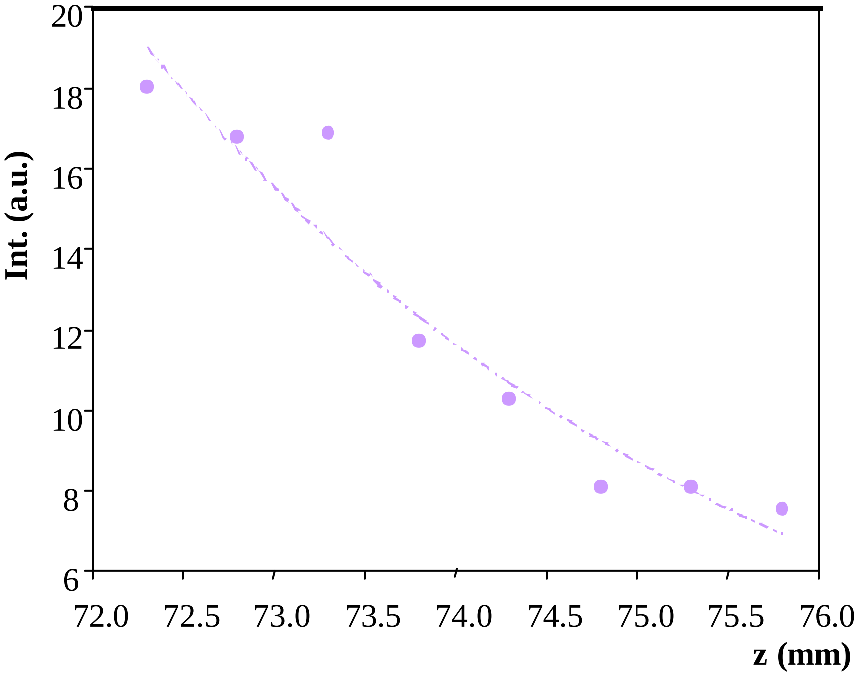

Figure 5.17: Distribution of the diffracted intensity versus the scanned depth (goniometer positions) of leucite powder (for l = 0.4506 nm).

- **Evaluation of leucite absorption coefficient on SAND**

SAND is a time-of-flight Small-Angle Neutron Diffractometer (Figure 5.18) at the IPNS facility at Argonne National Laboratory. This instrument is equipped with a Linear Position-Sensitive Detector bank. This enables SAND to obtain data in wide Q range (0.035 to 20 nm^{-1}) in a single measurement. Measurements on leucite massive sample in transmission dispersive energy measurements (Figure 5.19). The transmission coefficient of the samples has been measured on SAND which is a time-of-flight instrument that uses a wavelength range of 0.1 to 1.4 nm.

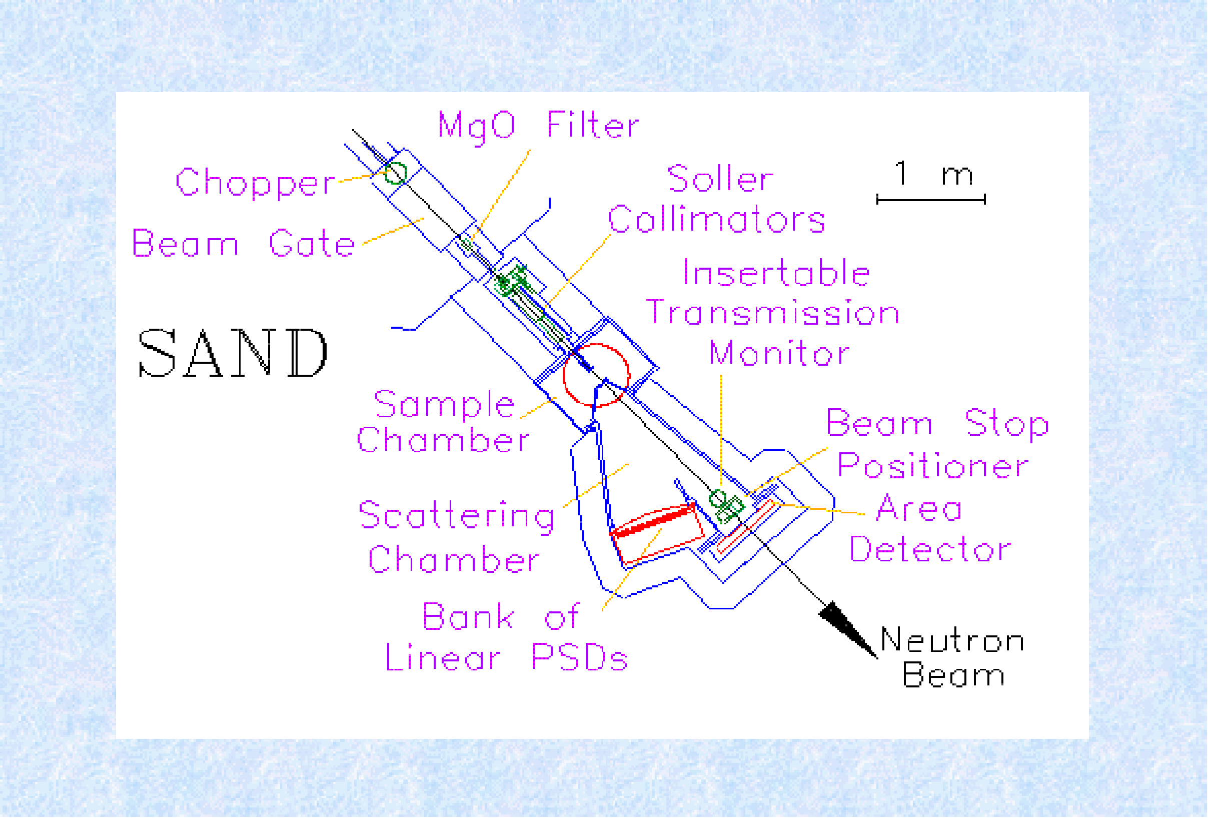

Figure 5.18: Measurement set-up of SAND time-of-flight instrument in Argonne Laboratory.

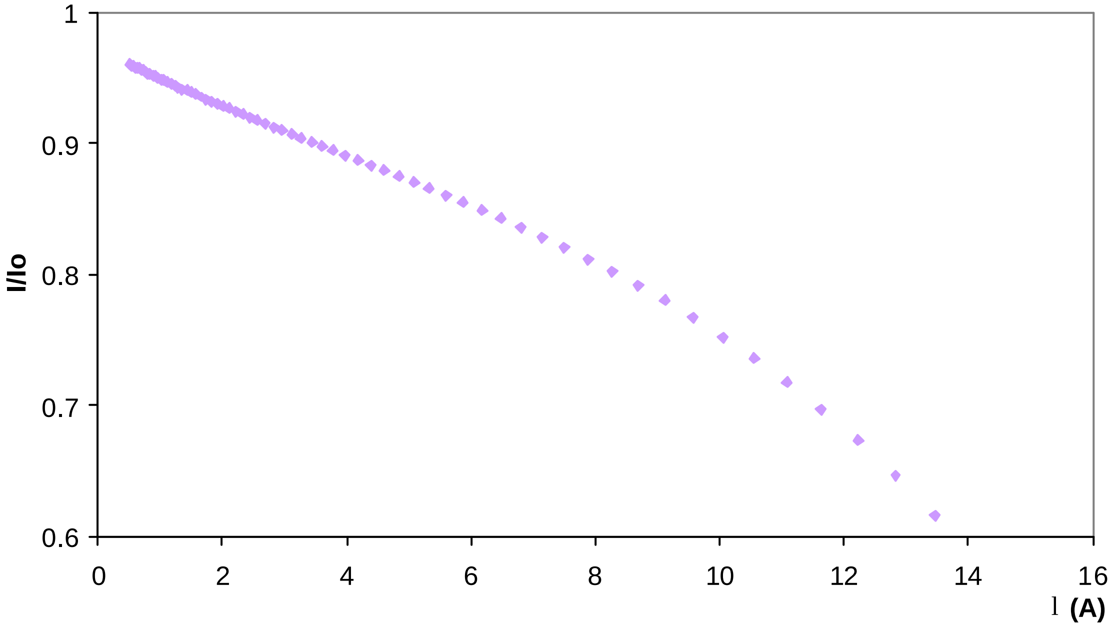

Figure 5.19: Absorption coefficients of leucite sample (for 0.1< l <1.4 nm).

The stress state of sample has been characterised by neutron diffraction (Figure 5.20).

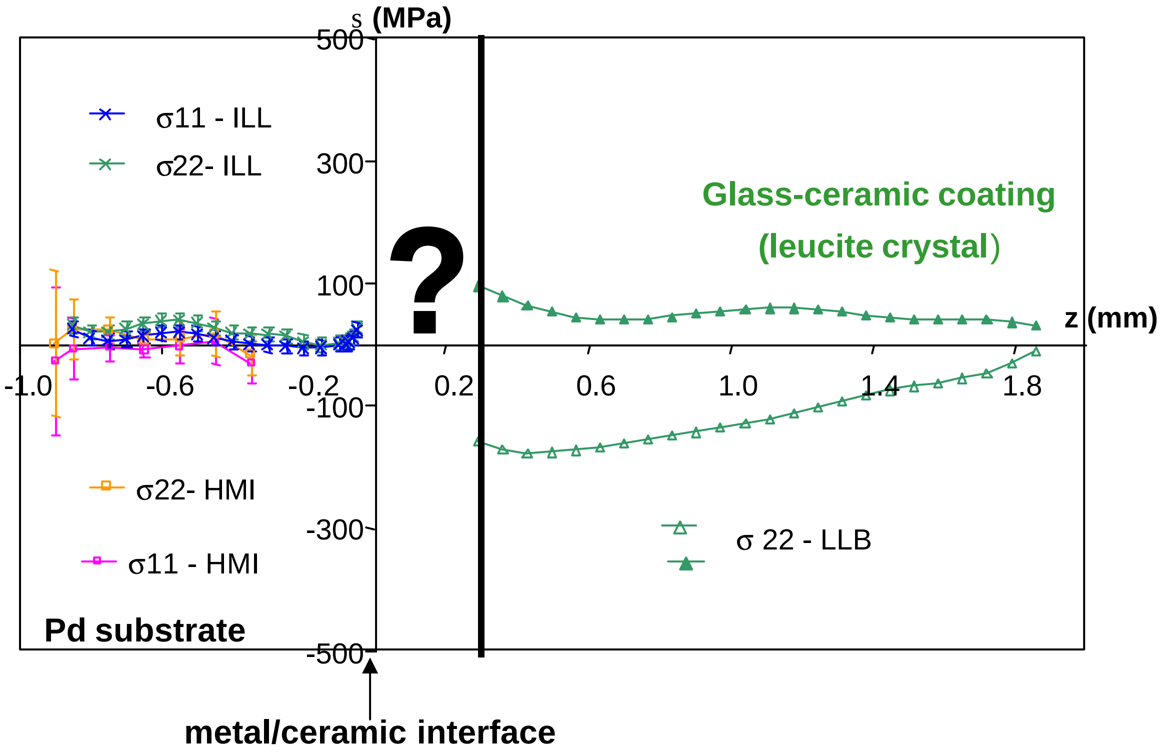

Figure 5.20: Synthesis of residual stresses distribution obtained by neutron diffraction.

5.4 High-Energy Synchrotron measurements: an introduction

Residual stresses today are well known to influence the mechanical properties of technical parts significantly. Conventional X-ray residual stress analysis, however, only yields information about a small surface layer. Stress analysis in the bulk of the material may be performed by neutron diffraction, but due to the large gauge volume, the spatial resolution often remains low. With the development of modern synchrotron sources, high-energy x-ray diffraction is starting to play an important role in the bulk analysis of materials.

Synchrotron strain scanning has evolved out of the neutron strain scanning technique. Synchrotron X-ray radiation with high flux and high photon energy (5 -150 keV) is typically 2 or 3 order of magnitude more penetrating than conventional CuK$_\alpha$ radiation [5.5]. Using the crystal lattice as an internal gauge, the high penetration of SR allow stress measurements throughout the bulk and interface sample by means of Bragg diffraction [5.6].

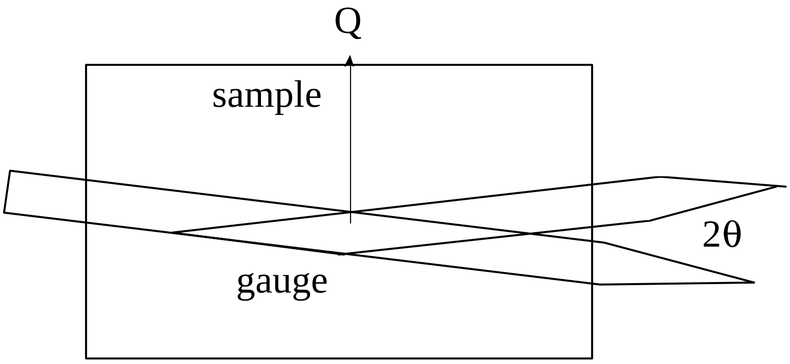

Figure 5.21: Schematic of incident and diffracted synchrotron X-radiation at a sample. The scattering vector is marked Q, the scattering angle 2q and the gauge volume.

Figure 5.22 shows a schematic of the incident and diffracted beams penetrating the sample. The incident beam size is defined by slits so that only a small illuminated volume can diffract. Collimating slits and analyser crystal in diffracted beam path, prior to the detector, means that only a certain volume of sample is within the detector’s field of view, which defines the gauge volume. Due to short wavelengths of the synchrotron radiation, hence low Bragg angles, the gauge volume usually has an aspect ratio of about 10:1; this gives a spatial resolution typically 10 times better in one direction than the other. However, with slits heights of ~ 100 µm and diffraction angle 2θ ~ 10°, making the gauge ~ 700 µm x 60 µm, the resolution remains still better than for neutron diffraction.

In energy dispersive spectra have been recorded at a fixed scattering angle 2θ. The reflections at different energy values have been measured in the same time. The lattice spacings d^{hkl} have been calculated by Bragg's law:

$$d^{hkl} = \frac{hc}{2\sin\theta} \cdot \frac{1}{E^{hkl}} \qquad \text{Eq. 5.1}$$

where h = Planck's constant, c= velocity of light and $E = \frac{hc}{\lambda}$.

5.5 High Energy X-Ray diffraction measurements on BM16

For analysing the residual stress in both the materials high-energy synchrotron measurements were performed. An experimental test was carried out first on the beamline BM16 at the European Synchrotron Radiation Facility (ESRF). Beamline BM16 is designed for powder-diffraction studies with very high angular and energy resolution. The specimen was S1. The incident beam has an energy of about 39 keV (λ = 0.03197 nm). It was focussed in two dimensions to 6x10 µm (height x width). Thus, the gauge volume was small enough to investigate several volume elements across the sample.

To evaluate the stress free lattice spacing d_{0hkl} a measurement was carried out in the bulk of the palladium alloy (where the sample is unstressed, as demonstrated by the neutron measurements). For the leucite, d_{0hkl} was defined from the mean of all the peak positions measured in the bulk of the coating.

Using the Bragg's law the shifts of 2θ were transformed into the lattice strain: $\varepsilon_{hkl} = \frac{d_{hkl} - d_{0hkl}}{d_{0hkl}}$.

Finally, assuming a plane stress state ($\sigma_{33} = 0$) and applying Hooke's law the residual stress state was determined.

In table 5.6 the experimental parameters are resumed.

Set-up	Equipment	BM16 powder-diffraction spectrometer
	Monochromator	{220} Cu
	Detector	Ge <111> analyser
	Primary slit (mm)	$0.05 \times 0.05 \times 15$
	Secondary slit (mm)	$0.05 \times 0.05 \times 15$
	Detector slit (mm) (height x width)	1x1
Parameters	Wavelength (nm)	0.03197
	Diffracting planes	{322} Leucite, {111} Pd
	Unstressed Diffraction angle (°)	10
	Data processing	strain scanning
Angles	χ Angles	0
	ψ Angles	0
Stress	Mean value of Longitudinal and Transverse components	$\frac{\sigma_{11} + \sigma_{22}}{2}$

Table 5.6: Experimental parameters BM16.

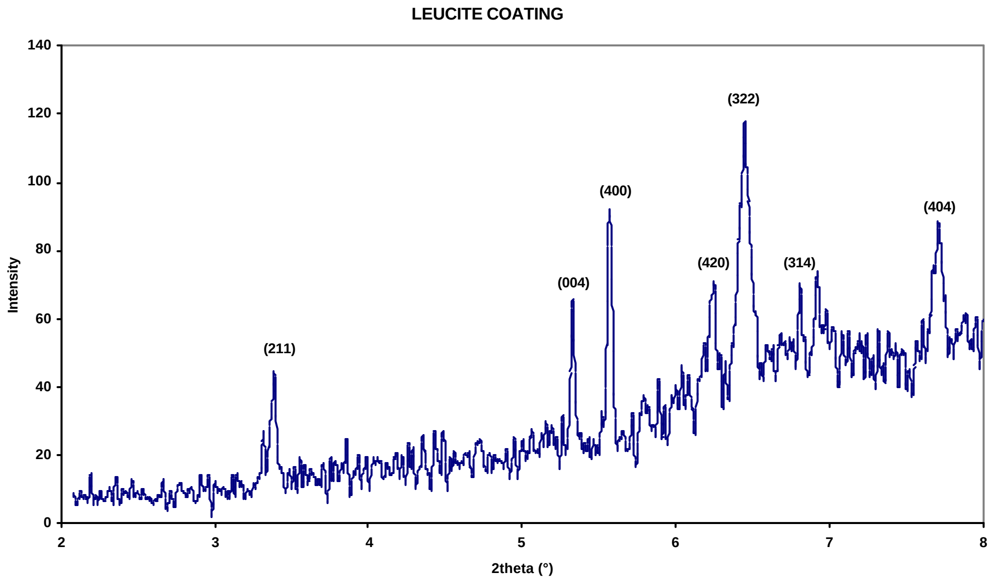

Figure 5.22: High energy X-ray diffraction diagram of the leucite coating.

In Figure 5.22 diffraction pattern of glassy ceramic coating based on leucite crystal is shown. The diffracting peak {322} was chosen for residual stress analysis in the ceramic.

The results in Figure 5.23 reveal that the stresses are very low in the leucite and are tensile in the Palladium alloy [5.10].

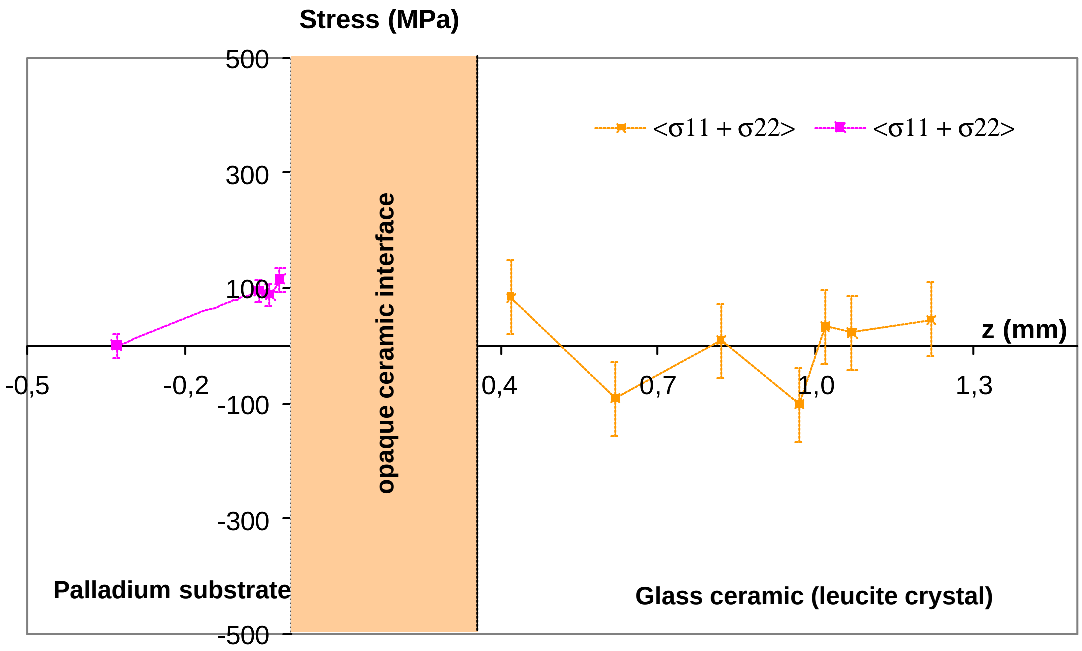

Figure 5.23: High-energy synchrotron measurements on palladium substrate, where $<s_{11}+s_{22}>$ is the average of two values.

5.6 High-Energy X-Ray experiments on ID15A beamline – experimental procedures

As shown in Figure 5.20, the neutron diffraction measurements did not succeed to characterise the interface, since there is a band of about 300 µm (opaque ceramic interface) where the stress state on sample S1 remains undefined. By high-energy synchrotron radiation, this zone will be characterised.

Palladium alloy substrate

The space resolution of this method requires however to be improved. For that reason, we have decided first to test the method on a sample without coating (sample S). This sample is machined, thus leading to high stresses in the surface layers. Such stress field has been evaluated accurately by X-rays using chemical etching (§5.1.1). This one gives a reference available to check the synchrotron measurement technique (data acquisition and treatment methods).

The high-energy X-ray experiments have been performed on ID15A beamline at ESRF (Grenoble), using a white-beam energy range from 50 to 150 keV. This set-up is a 3-axes diffractometer which allows a precise positioning of the samples in relation to the incident beam. The instrument was equipped with Eulerian cradle to adjust the χ and ϕ angles. The gauge volume was limited to 60 × 700 × 100 μm^3 by slits in the primary as well as in the diffracted beam (Figure 5.21).

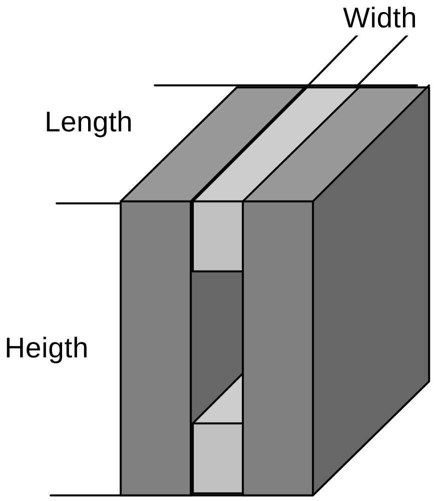

Figure 5.24: Slits.

The triaxial method has been used to evaluate the stresses in the longitudinal and transverse directions of the sample (σ_{11} and σ_{22}). These measurements have been carried out in χ mode with four incidences. The main experimental conditions are listed in Table 5.7.

Set-Up	equipment	ID15A 3-axes diffractometer
	energy range (keV)	30 - 150
	detector	high-resolution energy dispersive Ge
	obturator (mm) (height x width)	0.1 x 0.6
	secondary 1 slit (mm) (height x length x width)	10 x 10 x 0.6
	secondary 2 slit (mm) (height x length x width)	15 x 12 x 0.6
	detector slit (mm) (height x width)	1x1
Parameters	diffracting plane	{222}, {331}, {420}, {422}, {333}, {440}, {620}, {642}, {731}
	diffraction angle (°)	10
	data processing	triaxial
Angles	χ angles ψ angles	0, 90 0, -30, -45, 37

Stress	longitudinal and transverse	σ_{11}, σ_{22}

Table 5.7: Experimental parameters ID15A experimental conditions for palladium alloy substrate

The stresses were derived from the positions of 11 peaks of the energy dispersive spectrum (Figure 5.25). These peaks were adjusted to a split Gaussian using a least squares fitting.

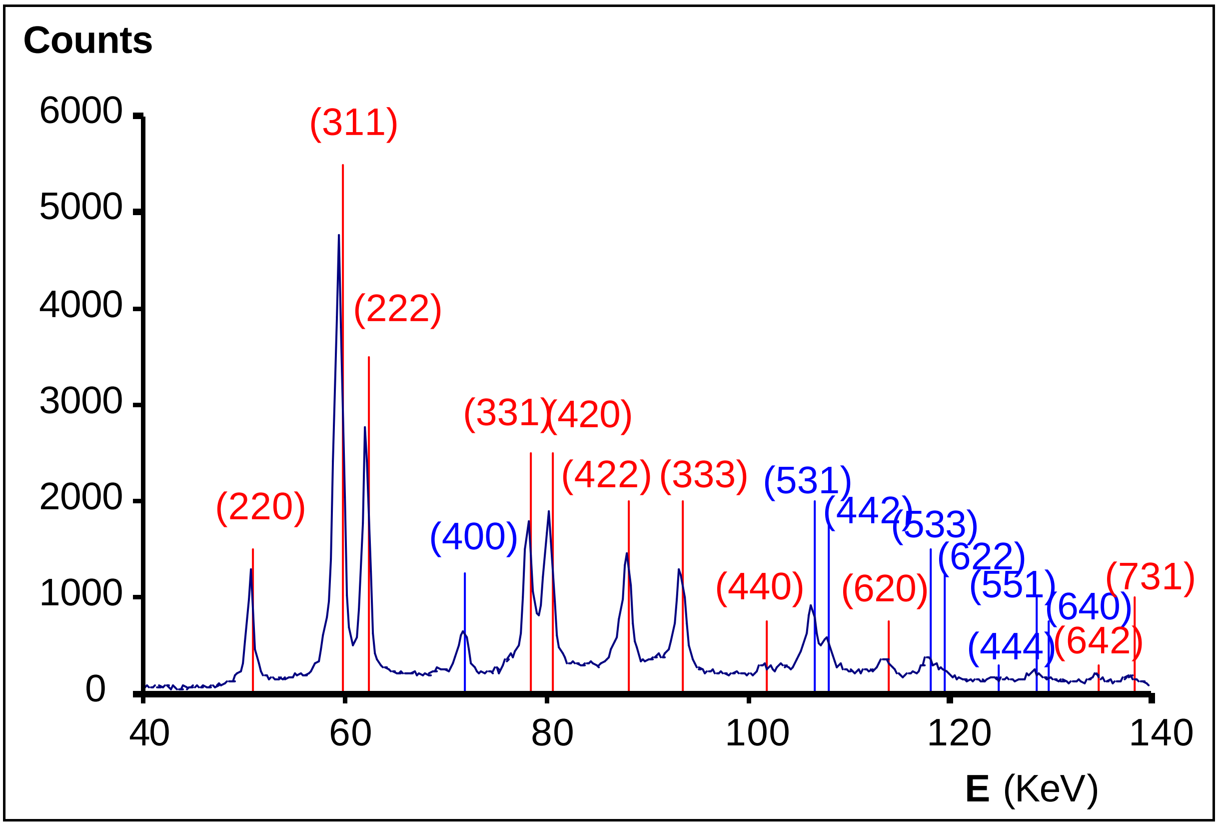

Figure 5.25: Palladium alloy substrate (sample S) synchrotron radiation pattern.

It is necessary to localise very precisely the true position of the diffracting volume inside the sample because the depth affected by the stresses is of the same order of magnitude than the size of the X-ray beam. This is obtained through a strain scanning across the studied interface, as for the neutrons.

The results show very strong absorption effects. For this reason, the experiment was modellised through a Monte Carlo simulation method which allows to predict the evolution of diffracted intensity versus adjusted depth Z_0 Figure 5.26. These theoretical curves are then fitted to the experimental ones to define the precise position Z_0 of the gauge volume. The reliability of this method is better than 2 µm.

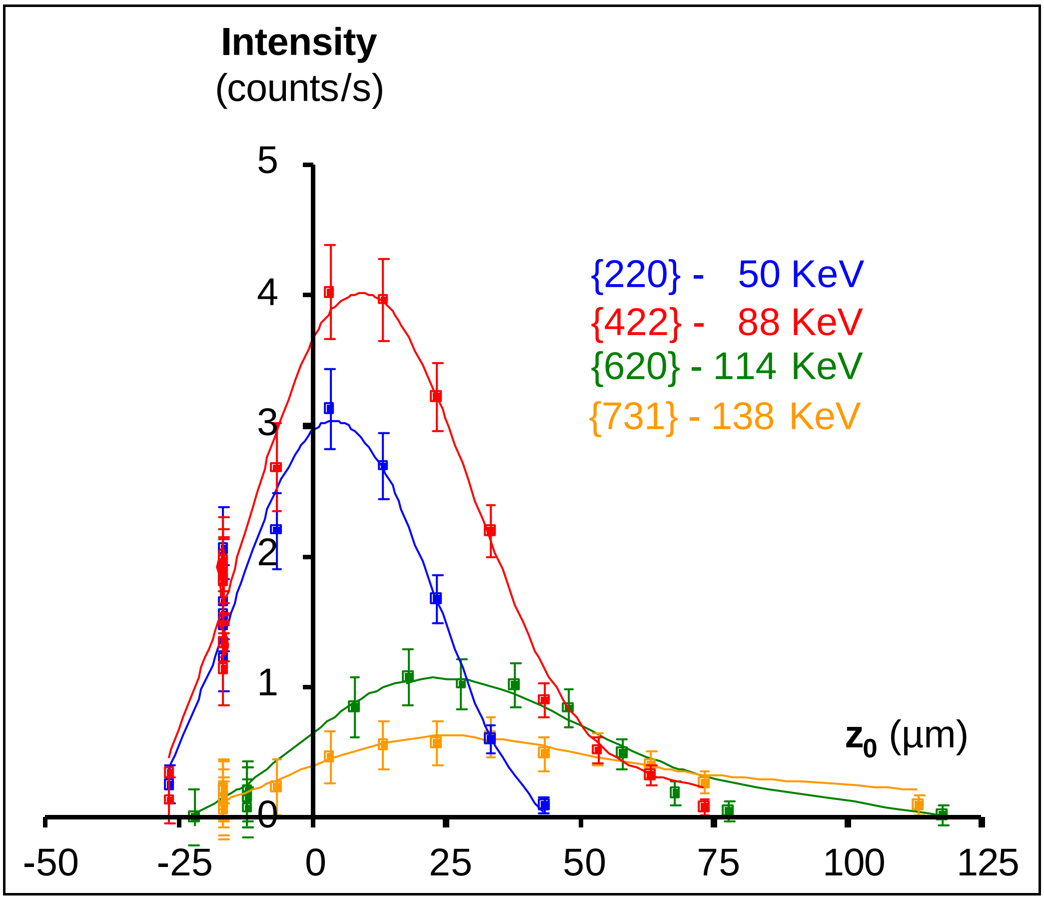

Figure 5.26: Evolution of diffracted intensity versus adjusted depth Z_0.

The simulation program allows also defining, for each reflection and position of the sample the true mean depth <Z> analysed by the X-rays. This depth varies greatly with the selected reflection (energy of the X-ray photons) and sample orientation (χ angle) Figure 5.27.

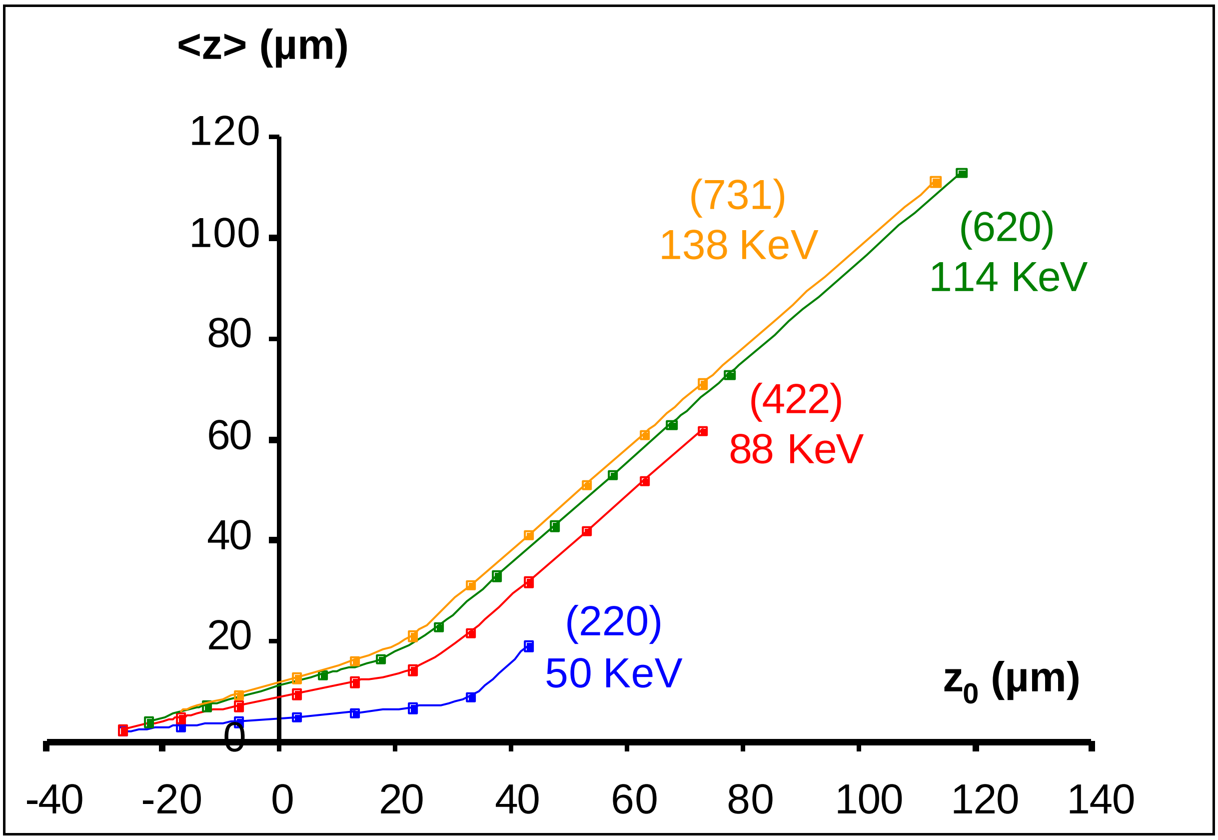

Figure 5.27: Variation of depth versus energy of the X-ray photons.

The in-depth profile of the longitudinal and transverse stresses is finally derived from the whole peak positions (more than 500 peaks). These stress profiles are therefore approximated by a mathematical function which is adjusted to the experimental data through a non-linear least squares fitting method. <u>In those calculation we account for the elastic anisotropy of the palladium crystal which leads to X-ray elastic constants depending on the analysed reflection</u>. The results are presented in Figure 5.28.

After these calibration measurements, the coated sample was also analysed to define the stress state at the interface between the palladium substrate and the opaque ceramic (sample S1). The same acquisition and data treatment method was used for that purpose. The experimental conditions are summarised in Table 5.8. The results are shown in figure 5.29.

Set-up	Equipment	ID15A 3-axes diffractometer
	Energy range (keV)	30 - 150
	Detector	high-resolution energy dispersive Ge
	Obturator (mm) (height x width)	0.1 x 0.6
	Secondary 1 slit (mm) (height x length x width)	10 x 10 x 0.6
	Secondary 2 slit (mm) (height x length x width)	15 x 12 x 0.6
	Detector slit (mm) (height x width)	1x1
Parameters	Diffracting plane	{220}, {311}, {222}, {331}, {420}, {422}, {333}, {440}, {620}, {642}, {731}
	Diffraction angle (°)	10
	Data processing	triaxial
Angles	χ Angles (°)	0, 90
	ψ Angles (°)	0, -30, -45, 37
Stress	Longitudinal and Transverse	σ_{11}, σ_{22}

Table 5.8: Experimental parameters ID15A experimental conditions for palladium alloy substrate.

Set-up	equipment	ID15A 3-axes diffractometer
	energy range (keV)	30 - 150
	detector	high-resolution energy dispersive Ge
	obturator (mm) (height x width)	0.1 x 0.6
	secondary 1 slit (mm) (height x length x width)	10 x 10 x 0.6
	secondary 2 slit (mm) (height x length x width)	15 x 12 x 0.6
	detector slit (mm) (height x width)	1x1
Parameters	diffracting plane	{161}, {144}, {252}, {136}
	diffraction angle (°)	10
	data processing	triaxial
Angles	χ angles (°) ψ angles (°)	0, 90 0, -30, -45, 37
Stress	longitudinal and transverse components	σ_{11}- σ_{33}, σ_{22} -σ_{33}

Table 5.9: Experimental parameters ID15A experimental conditions for glassy ceramic coating.

5.7 Discussion and result

The stress results obtain for the superficial layers of the uncoated sample are shown in Figure 5.28. These stress profiles are compared to the values obtained by classical X-rays after chemical etching.

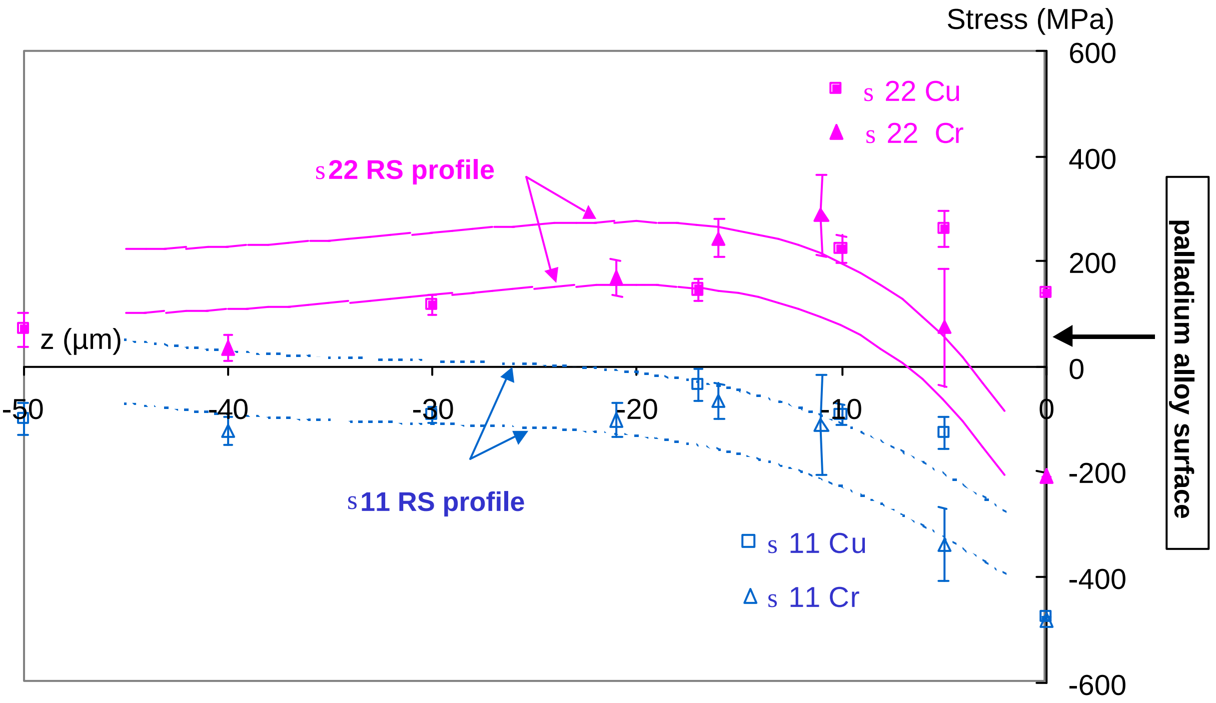

Figure 5.28: Residual stresses distribution for the superficial layers versus scanned depth.

The results of the classical X-ray measurements and the synchrotron radiation experiments are in good agreement. The sample has been machined by milling. As it could be expected for such kind of manufacturing process, the stress in the direction perpendicular to the cutting direction (σ_{11}) is compressive. In the machining direction (σ_{22}), the stresses are mainly tensile due to the shearing of the metal during the cutting. The near surface stresses are however compressive in both directions due to the friction of the tool onto the sample surface.

For the stress results obtained on the coated sample (S1) are presented in Figure 5.29 (interface layers of the palladium substrate) and (leucite phase of the coating).

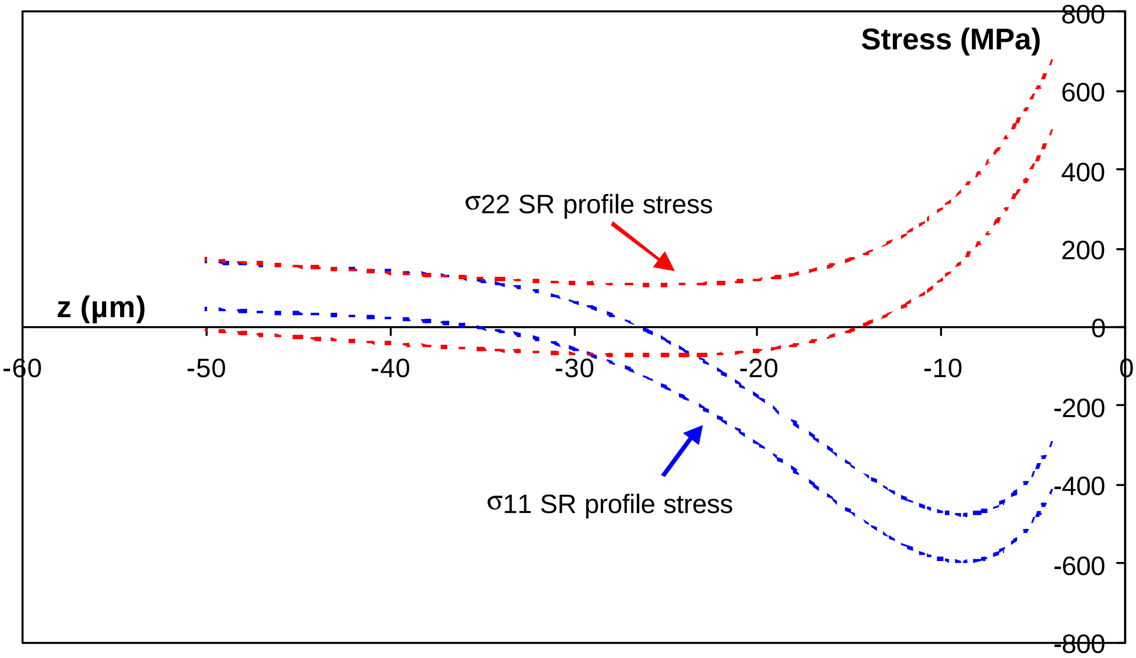

Figure 5.29: In-depth residual stress for palladium alloy substrate of sample S1.

As already found in the neutron measurements, the stresses in the core of the palladium substrate are very low. However, significant stresses are observed in a layer of about 20 µm near the interface. This depth is of the same order of magnitude as the thermal affected depth. As shown by the TEM observations, this zone is completely recrystallised. The thermal expansion mismatch (difference in the expansion coefficients) between the ceramic and the substrate remains small and should lead to very low equibiaxial stresses. This means that the high tensile stresses observed in the transverse direction are not due to pure thermal effects but may be induced by other chemical and metallurgical mechanisms.

The residual stress in the crystallised K_2AlSiO_6 glassy ceramic was also determined using four crystallographic planes. The mean CTE of this crystalline phase is greater than that of the glassy matrix. For that reason, the diffraction method does not allow to determine the true stress components by only the differences σ_{11}-σ_{33} and σ_{22}-σ_{33}.

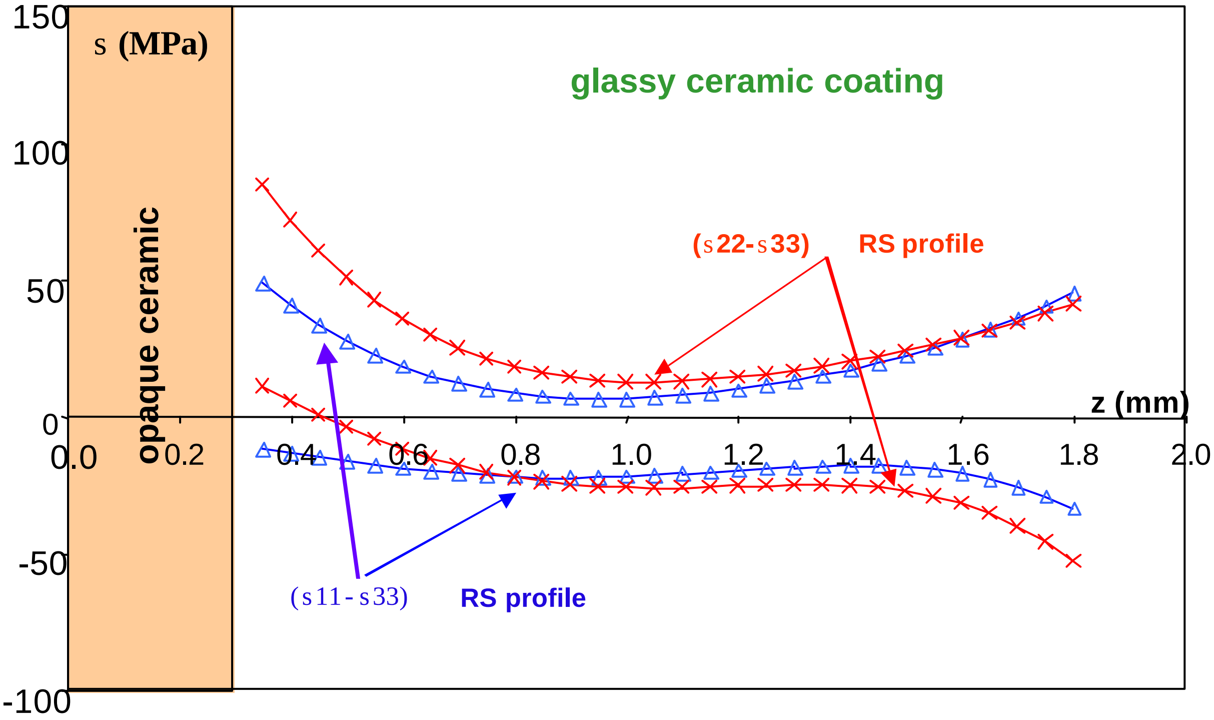

Figure 5.30: Residual stress for glassy ceramic coating (leucite crystal) of sample S1.

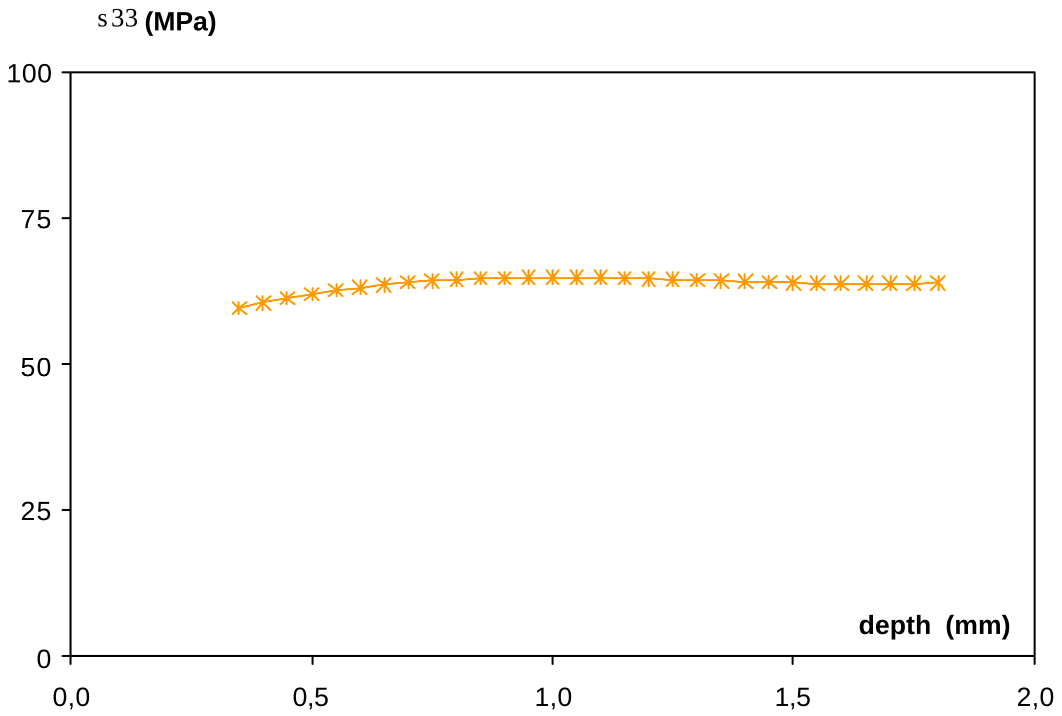

Figure 5.31: Theoretical value of the stress component s_{33}.

A theoretical value of the stress component σ_{33} has however already been calculated through the isotropic self–consistent mechanical model. Moreover, as demonstrated in chapter 2. This data is proportional to the macro-stress components $<\sigma_{11}>$ and $<\sigma_{22}>$.

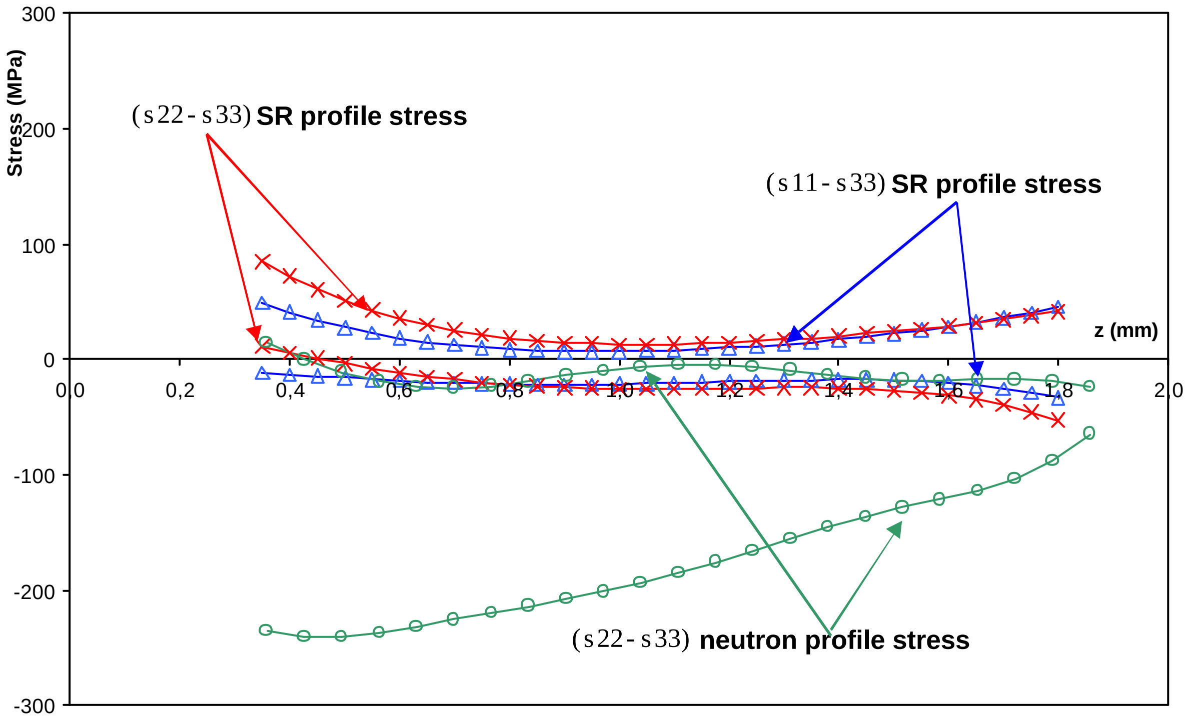

Figure 5.32: ID15A and LLB plot of residual stress for glassy ceramic coating of sample S1.

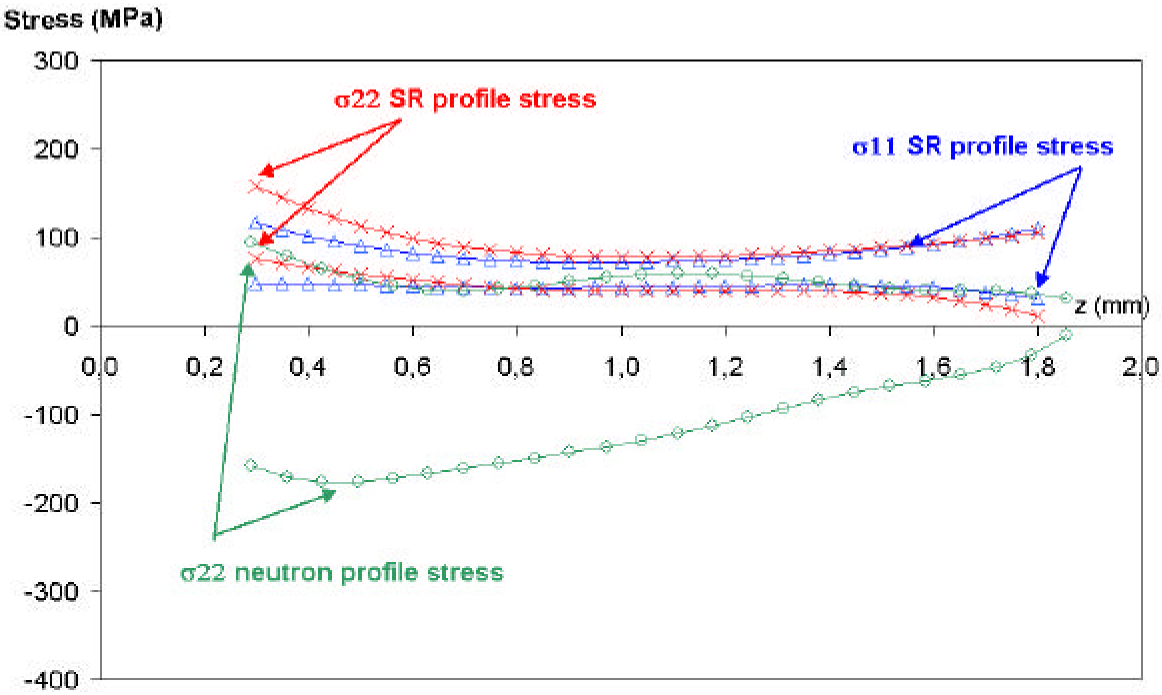

Figure 5.33: ID15A and LLB plot of <u>CORRECTED</u> residual stress for glassy ceramic coating of sample S1.

5.8 Synthesis of results obtained inside the sample

At this stage of the study, we can now put together the results obtained in our work. Let us first analyse the stress profiles obtained in the palladium substrate. The results obtained on D1A (ILL) and E3 (HMI) in the zone between 350 and 900 µm presents globally the same tendencies. The residual stresses in the bulk of material are lightly in traction and the values are close to zero Figure 5.34. Between 350 and 70 µm the values of residual stress do not grow up.

In the zone between 70 µm and the interface, only high-energy synchrotron radiation measurements were possible as already pointed out in detail. The longitudinal component presents a high value in compression while the transverse component is in traction.

The stress in this region is due to mechanical and thermal treatments. Thermal stresses could be originated from the difference of thermal expansion coefficients between the opaque ceramic and the metallic substrate. These stresses should however remain low. A quick calculus has already been reported about this in chapter 2.

As concerning the stresses profiles in opaque ceramic, data exploitation are more difficult than for the substrate because of the presence of four phases in the material. Another serious problem is linked to the difficult understanding of the interaction among the different phases. In addition, this zone is too close from the metal/ceramic interface to be studied by neutron diffraction. No reliable result could be obtained by high-energy synchrotron radiation for two causes:

- First, this diffracting angle was well adapted for the characterisation of the palladium alloy but not for the crystalline phases of the opaque ceramic;
- Second, the crystallite size in this zone is large compared to the dimension of the gauge volume. This leads to spotty diffraction diagrams.

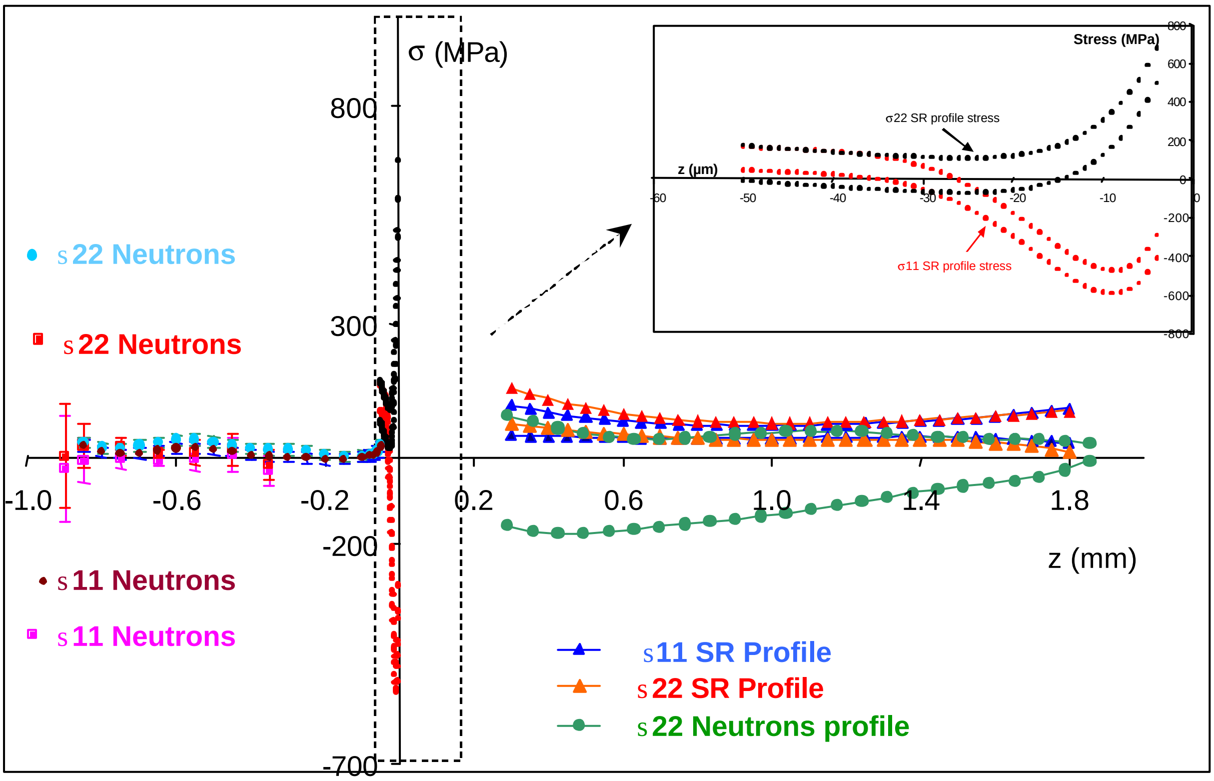

Figure 5.34: Residual stress profile in the sample S1 by neutron diffraction and synchrotron radiation

References

[5.1] Impediments to efficient through surface scanning, Webster P.J., Mills G., Wang W.P., Holden T.M., Journal of neutron research, 3, (1996), p. 223-240

[5.2] Interactive effect of stress and temperature on creep of PMF alloys, Anusavice K.J., et al. J. Dent. Res. 64: pp1094-1099, 1985.

[5.3] Residual stresses evaluation near interfaces by means of neutron diffraction: modelling a spectrometer, Pluyette E., Sprauel J.M., Lodini A., Perrin M., Todeschini P. ECRS4, Cluny: pp.153-163, 1996.

[5.4] Stress evaluation by neutron diffraction: Modelling of a two axis spectrometer, Sprauel J.M, MecaSens Reims 13/14-12/ 2000.

[5.5] Residual Stress. Measurement by Diffraction and Interpretation (Materials Research and Engineering), Noyan I.C., Cohen J.B., 1987.

[5.6] Withers PJ, synchrotron radiation as a probe for high resolution sub surface residual stress measurement, invited lecture at the 6th MATTEC conference on analysis of Residual stress, Reims, 1997

[5.7] B. D. Cullity, Elements of X-ray diffraction (second edition) 1978, Addison-Wesley Publishing Company. Chapters 10 and 11.

[5.8] Eschelby J.D., Proc. Roy. Soc. A241 (1957) 376

[5.9] High-energy synchrotron radiation, a new tool for residual stresses analyses, A. Pyzalla, A. Royer, L.D. Liss, W. Reimers, ESRF Workshop 12/2/1999.

[5.10] A. Carradó, J.M. Sprauel, A. Lodini " High Energy Synchrotron Radiation investigation for residual stress evaluation in ceramic/metal interface "abstract by poster presentation at V National School on Synchrotron Radiation, Santa Margherita di Pula (Cagliari) 27 September - 8 October 1999.

[5.11] A. Carradó, J.M Sprauel, L. Barrallier, A. Lodini, " Neutron and Synchrotron evaluation of residual stresses in coatings " oral presentation, Journal-article, Journal of Neutron research, in press MECA-SENS 2000, Reims, 14-15 December 2000.

CONCLUSION

We have studied in this work the residual stress at the interfaces of a glassy ceramic coated onto a palladium alloy substrate. Measurements by diffraction techniques have been realised in different zones of the sample. We have used neutron diffraction, classical X-rays and high-energy synchrotron radiation. These techniques, largely employed, lead to very good results. They have permitted us to obtain a precise and non-destructive evaluation of the residual stress in the core and at the interface of the materials.

In particularly, we have employed the neutron diffraction to analyse the surface and the bulk of glassy ceramic and the core of the metallic substrate. In addition, high-energy synchrotron radiation has been used to study the metal/ceramic interface. Therefore, we found that the used techniques are complementary, because they allow analysing different zones of the sample.

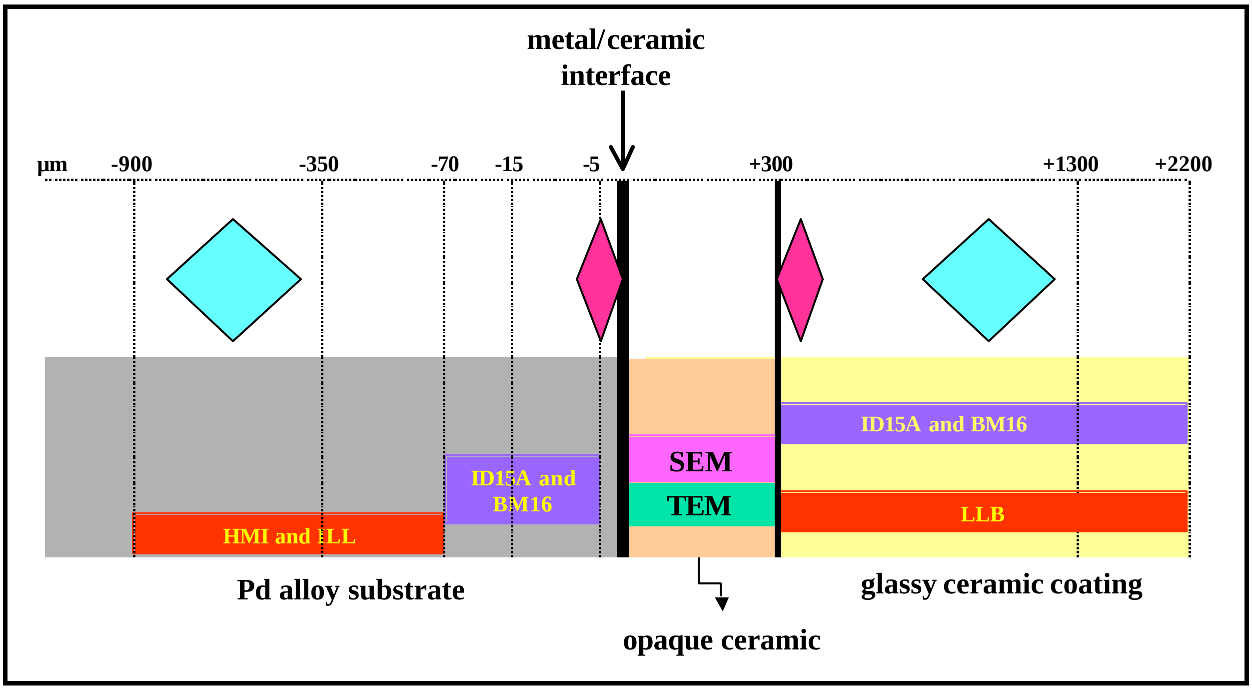

Schema of performed measurements on analysed sample S1.

The principal objective of this work was to evaluate the residual stress in a glassy ceramic coated on a cast palladium alloy substrate.

Residual stress is present in the two materials. They depend principally on the thermal treatments imposed to the sample. They could have a very strong influence on the mechanical behaviour in the sample and in particular on the existing bounding at the metal/ceramic interface.

We have also improved the experimental techniques dedicated to the determination of residual stress. This has required a precise and refined data processing, which accounts for different physical phenomena and for geometrical aberrations which appear in the measurements.

Concerning the residual stresses analysis we have focused our study to the metal/ceramic interface; this is the region where the stresses are generated.

Some measurements have been realised by diffraction techniques in the different zones of the sample. In particularly, we have employed the neutron diffraction to analyse the surface and the depth of the glassy ceramic, and the bulk of the metal. The metal/ceramic interface has been analysed by high-energy synchrotron radiation.

We have also improved the data acquisition and treatment procedures. This increases the precision at which the position of diffracting volume is localised in the sample. The residual stress profile induced by the machining of the sample has been evaluated by classical X-ray diffraction measurements, using chemical etching. This technique is, in fact, well adapted for this kind of problem. We have thus obtained reference values which allowed testing a new experimental approach used for high-energy synchrotron measurements. Since the results obtained by both techniques were in good agreement, synchrotron measurements could be used with a good confidence to characterise the residual stress at the metal/ceramic interface.

Finally, we have determined the residual stress in the coating using neutron diffraction and high-energy synchrotron radiation (ID15A and BM16). The stress profile in the ceramic shows low values. However, it is possible to find significant stress near the interface.

As we have also underlined in the chapter 5, the stress profile in the opaque ceramic is of difficult exploitation. This is due to the presence of four phases in the material. For that reason the understanding of the interaction between the different phases is more difficult. On the other side, this region is too close from the metal/ceramic interface to be analysed by neutron diffraction (big size of neutron gauge volume).

No reliable result could be obtained by high-energy synchrotron radiation for two reasons. *First*, this diffracting angle was well adapted for the characterisation of the palladium alloy but not for the crystalline phases of the opaque ceramic. *Second*, the crystallite size in this zone is large compared to the dimension of the gauge volume. This leads to spotty diffraction diagrams.

To have a general idea of the opaque ceramic region of the sample, this zone has however been studied from a morphological point of view by scanning and transmission electron microscopy. The presence of mechanical anchorage means that stress should exist in this zone but could not be quantified today. This leaves open future prospective that we will develop during our future research activities.

In the glassy ceramic, the residual stresses have been evaluated by neutron diffraction and high-energy synchrotron radiation. Obviously, the study has been focalised in the major crystallised part of the glassy ceramic: the leucite crystals. In this coating a great quantity of amorphous matter has been detected. The precise volume fractions of amorphous and crystallised parts are not possible to quantify. This is due to the difficulty to obtain reference powders from the manufacturer, which are required for quantitative phase analysis. One solution would be to determine the crystalline and amorphous part of the ceramic layers by Rietveld refinement, but such method requires a calibration. In any case some measurements have been carried out either by cold neutron diffraction (studying crystallised leucite) and high-energy synchrotron radiation.

Classical X-ray measurements were not successful due to a low diffracting angle (great lattice parameter), thus leading to poor accuracy.

The residual stress evaluated in the crystalline phase of the glassy ceramic by high-energy synchrotron radiation exhibit the same profile as the results obtained at LLB by Neutron diffraction. The gap between the two profiles may be due to the difference of area and volume (gauge volume) investigated by each diffraction technique. In fact, neutron diffraction involves large volumes (a few mm^3) and leads thus to average values over a great number of crystallites. High-energy synchrotron radiation techniques, on the contrary, only characterise local properties of the material. In this layer, X-ray texture measurements showed no evidence for texture. The isotropic self-consistent method can therefore be used to evaluate the macroscopic stresses of the ceramic coating from the measurements obtained experimentally on the single leucite phase. Consequentially, it would be very interesting to evaluate the stress profile starting from the metal/ceramic interface and going inside the first 300 µm of the ceramic (opaque ceramic interface). In fact, just the microstructure of the material has been characterised in this zone, using SEM and TEM techniques.

Appendix

A.1 Talk and article in press on Journal of Neutron Research (2001).

NEUTRON AND SYNCHROTRON EVALUATION OF RESIDUAL STRESSES IN COATINGS

Adele Carradó[1,2], Jean-Michel Sprauel[3], Laurent Barrallier[4] and Alain Lodini[1,2]

[1]L.A.C.M., Université de Reims Champagne Ardenne, France
[2]L.L.B., Laboratoire Leon Brillouin, CEA- Saclay, France
[3]LM3, E.N.S.A.M., Paris, France
[4]E.N.S.A.M., Laboratoire MécaSurf, Aix-en-Provence, France

ABSTRACT

The present study is dedicated to the evaluation of residual stresses at surfaces, in the bulk of materials and at interfaces, by classical X-ray and neutron diffraction and high-energy synchrotron measurements. It is mainly focused on the improvement of these experimental techniques. The new developed methods have been applied to a coating which consists of leucite moulded on a palladium alloy substrate. These materials are employed in dental applications.

INTRODUCTION

Generally, ceramic materials exhibit lower thermal expansion than metals. If ceramic on metallic substrate is produced at high temperatures, stresses are generated due to thermal expansion mismatch between the two components. This results in a deflection or fracture [1]. Ceramic on metallic substrates has been accepted as one of the most promising implant materials in orthopaedics and in dental applications because of its favourable biocompatibility and mechanical properties. Various coating techniques, such as plasma spraying or Porcelain-Fused-to-Metal (PFM), have been developed for that purpose. Among these, PFM appears to be the most favourable one in terms of mechanical properties, biocorrosion resistance, coating-substrate bonding strength and process feasibility.

The results obtained by neutron diffraction have shown that to analyse near surface measurements or data obtained at the metal/ceramic interface it is necessary to account for some optical aberrations related to the instrumentation. In fact, reliable results cannot be obtained by usual experimental procedures, because the neutron probe is not completely immersed in the analysed sample [2]. Therefore, it is important to correct the parasitic peak shifts which appear in these cases and which are not linked to the stress state of the scanned volume. This effect can be much greater than the peak shifts induced by the stresses.

A complete modelling of 2-axis spectrometers, based on Monte Carlo calculations, has been developed to solve this problem [3]. It accounts for the whole elements of the neutron or synchrotron instrument: the guide, the monochromator (if necessary), the primary and secondary slits and the sample. It allows also to optimise the experimental conditions and to define precisely the true volume of the neutron gauge.

SAMPLES

In this work two different specimens have been analysed (Table I):

Sample A consists of a substrate of palladium alloy and a leucite coating. It has been analysed by neutron diffraction.

Sample B is a palladium alloy plate without coating. It has been used to test the synchrotron measurement technique.

THE METHOD

Some problems arise when measurements are performed at interfaces. It is therefore necessary to localise very precisely the neutron (or synchrotron radiation) gauge and its diffracting part inside the sample. This is obtained through a strain scanning across the studied interface. The true position of the neutron (or synchrotron radiation) gauge volume is then derived from the evolution of the diffracted intensity versus the scanned depth. Such a curve can be defined experimentally or through the Monte Carlo simulation program.

The evolution of the diffracted intensity can be plotted versus the position Z of the geometric centre of the neutron probe. The intensity increases when the gauge volume enters the material. For the X-rays, it then decreases quickly. Its evolution is very slow for the neutrons. Classically, it is considered that at half maximum of this curve, exactly half the neutron probe is immersed. In our case, due to the strong absorption of the palladium, this assumption is valid neither for the neutrons nor for the X-rays. The precise position Z has been defined therefore through the adjustment of the experimental data to the theoretical curve. The accuracy of this method is a few tens of micrometers for neutron strain scanning and a few microns for synchrotron measurements.

Usually it is assumed that each measurement is carried out at the position Z defined by the geometric centre of the neutron (or synchrotron radiation) probe. This approximation is valid only when the gauge volume is entirely immersed in the sample and the material is weakly absorbent. For the palladium, that is strongly absorbent, the true centre of gravity Z_{true} of the diffracting volume (that is the immersed part of neutron probe) has to be considered. This position has to account for the absorption phenomena (which is stronger for X-rays than for the neutrons, as shown in the figure 1) and for the evolution of the local conditions of diffraction in the diffracting volume [4]. The relation between Z and Z_{true} has been defined by the simulation program.

EXPERIMENTAL PROCEDURE

Due to the great difference of the lattice parameters of the palladium and the leucite (Table I), these two constituents could not be characterised on one single neutron instrument. For the ceramic a longer wavelength is required (> 0.4 nm). The experiments have been carried out therefore on G5.2 at LLB (Saclay, F), using cold neutrons. For the palladium substrate, the measurement conditions are more classical. The experiments have been carried out on D1A at ILL (Grenoble, F) and on E3 at HMI (Berlin, D).

NEUTRON DIFFRACTION MEASUREMENTS ON PALLADIUM SUBSTRATE AND LEUCITE COATING

The stress state of sample A has been characterised by neutron diffraction (figure 2).

Palladium substrate

The bulk of the metallic substrate was studied at HMI Berlin on the E3 instrument. The {331} reflection of the FCC phase of Palladium was analysed for that purpose with a wavelength of about 0.137 nm (diffraction angle $2\theta = 99°$). The neutron gauge was set to $1.5 \times 1.5 \times 10$ mm^3. Due to low diffracted intensity, it has not been possible in a reasonable time to obtain valid results for positions nearer the interface than 300 µm. A triaxial method has been used to evaluate the stresses in the longitudinal (σ_{11}) and transverse (σ_{22}) directions of the sample [5]. These measurements were carried out in ω mode with four ψ incidences (0°, 30°, 60° and 90°). At ILL Grenoble on D1A, the {311} reflection of the FCC phase of Palladium has been analysed with a wavelength of about 0.19114 nm (diffraction angle $2\theta = 106°$). On this facility the neutron flux is much greater than at HMI. A small neutron gauge volume ($0.5 \times 0.5 \times 10$ mm^3) could therefore be selected. With these conditions, the stresses could be characterised to within 60 µm from the interface. A triaxial method has been used to evaluate the stresses in the longitudinal and transverse directions of the sample. HMI results have been confirmed. The stresses are mainly tensile, but very low.

Leucite coating

Due to the large lattice parameters of the leucite, cold neutrons were used to study this constituent. The experiments have been carried out at LLB Saclay on G5.2, the two axis diffractometer dedicated to the evaluation of residual stresses and equipped with a position-sensitive detector. The {002} reflection of the graphite monochromator was used, giving a neutron wavelength of 0.4506 nm. The stress measurements used the leucite {004} diffraction peak at approximately 82° 2θ. For the strain scanning, the size of the gauge volume was defined by a primary slit of 1 x 35 mm^2 and a detector slit of 0.8 x 35 mm^2. This set defines a parallelepiped probe volume. The $\sin^2\psi$ method has been used to evaluate the stresses. These measurements have been carried out in ω mode with four independent ψ incidences 0°, 30°, -40°, -15. Due to the low diffracted intensity, linked to a high amount of amorphous phase, only the stress component σ_{22} in the transverse direction of sample has been determined. The stresses are mainly compressive.

HIGH-ENERGY SYNCHROTRON AND CLASSICAL X RAY MEASUREMENTS ON PALLADIUM SUBSTRATE

As shown in figure 2, the neutron diffraction measurements did not succeed to characterise the interface, since there is a band of width about 150 µm where the stress state remains undefined. We expect to characterise this zone by high-energy synchrotron radiation. The space resolution of this method requires however to be improved. For that reason, we decided to test the method on a sample without coating (sample B). This sample is machined, thus leading to high compressive stresses in the surface layers. Such stress field can be characterised accurately by classical X-rays. This gives a reference available to check the synchrotron measurement technique.

The high-energy X-ray experiments have been performed on ID15A beamline at ESRF (Grenoble), using a white-beam energy range from 50 to 150 keV. The gauge volume was limited to $60 \times 700 \times 100$ µm^3 by slits in the primary as well as in the diffracted beam. The diffracted intensities were recorded by means of a high-resolution energy dispersive germanium detector. The measurements were focused on the evaluation of the stresses in the first layers of the base metal. The {220}, {311}, {222}, {331}, {420}, {422}, {333}, {440}, {620}, {642} and {731} reflections of the FCC phase of Palladium have been analysed for that purpose with a diffraction angle 2θ of 5°. The $\sin^2\psi$ method was used to evaluate the stresses in the longitudinal direction of the sample (σ_{11}). These measurements were carried out in ω mode with four incidences (0°, -30°, -45° and 37°).

The size of the X-ray beam is very small. The true position of the diffracting volume inside the sample has therefore to be localised very precisely. As for neutrons, this is obtained by strain scanning across the studied interface, with a step of 10µm. About 500 diffraction peaks were thus been acquired. The results show very strong absorption effects (figure 1). For this reason, this phenomenon has been completely modellised through a Monte Carlo simulation. This allows the in–depth evolution of the diffracted intensity to be predicted and the true centre of gravity of the diffracting volume to be defined. As for the neutron experiments, the precise position of the diffracting volume was defined through the adjustment of the experimental data to the theoretical curves. The reliability of this method is better than 2 µm. The in-depth stress profile of the analysed sample is then deduced from the positions of the 500 acquired diffraction peaks, using a least squares optimisation method. This profile is defined for that purpose by a mathematical function. The least squares refinement account also for the elastic anisotropy of the palladium crystallites. The results are presented in figure 3.

Classical X-ray measurements have also been carried out at E.N.S.A.M Mécasurf Laboratory. These experiments were conducted on a mobile equipment (SETX, *y* -mounting diffractometer manufactured by Physique Industries under ENSAM license), using the chromium K_α radiation and the {311} reflection of palladium (2θ = 148°). The stresses have been characterised by the $\sin^2\psi$ method, in the longitudinal and transverse directions of the surface. The normal stresses are compressive (σ_{11}= -467 ± 75 MPa and σ_{22} = -127 ± 64 MPa). No shear stresses have been observed. The results of the classical X-ray measurements and the synchrotron radiation experiments are in a good agreement.

Conclusion

The experimental techniques, dedicated to the residual stresses evaluation at the interfaces and in the bulk of materials (Classical X-rays, neutrons and synchrotron radiation) have been improved. New data treatment procedures, based on a numerical simulation of the instruments, have also been developed. These methods allow accurate and non-destructive evaluations of the in-depth residual stress profiles of surface or interface layers.

References

[1] Interactive effect of stress and temperature on creep of PMF alloys, Anusavice K.J., et al. J. Dent. Res. 64: pp1094-1099, 1985

[2] Impediments to efficient through surface scanning, Webster P.J., Mills G., Wang W.P., Holden T.M., Journal of neutron research, 3, (1996), p. 223-240.

[3] Residual stresses evaluation near interfaces by means of neutron diffraction: modelling a spectrometer, Pluyette E., Sprauel J.M., Lodini A., Perrin M., Todeschini P. ECRS4, Cluny: pp.153-163, 1996.

[4] Stress evaluation by neutron diffraction: Modelling of a two axis spectrometer, Sprauel J.M, MecaSens Reims 13/14-12/ 2000.

[5] Residual Stress. Measurement by Diffraction and Interpretation (Materials Research and Engineering), Noyan I.C., Cohen J.B., 1987.

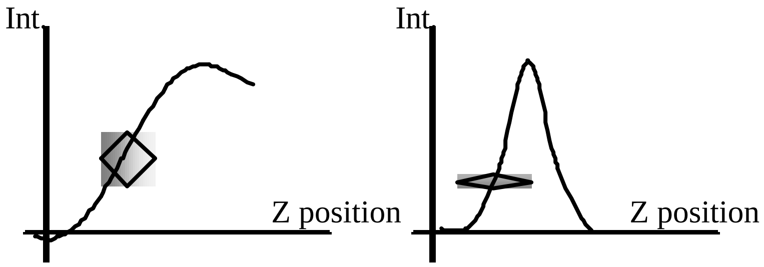

Neutrons Synchrotron

Figure 1: In-depth intensity curves considering the absorption

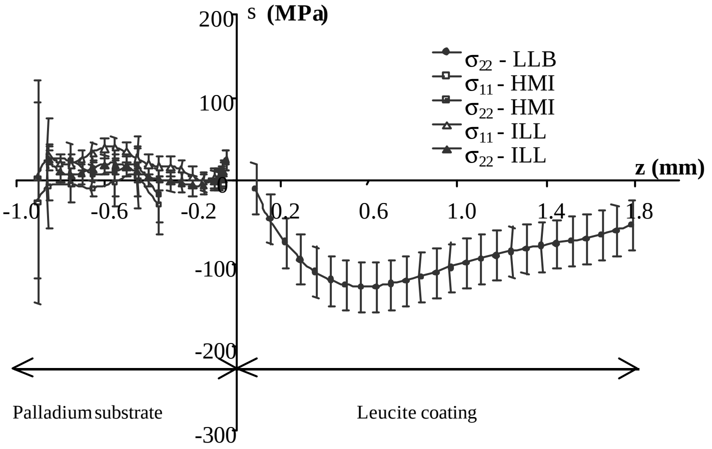

Figure 2: In-depth distribution of residual stresses as characterised by neutron diffraction.

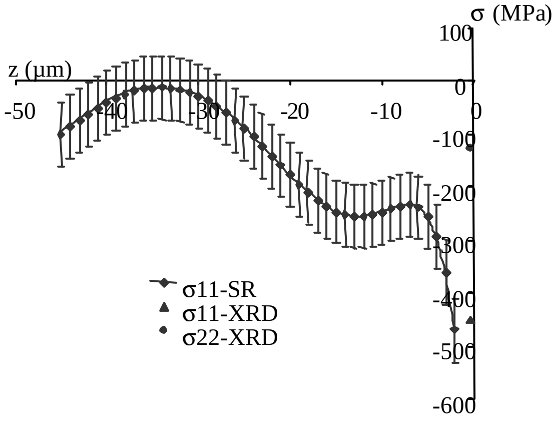

Figure 3: In-depth stress profile of the palladium substrate as evaluated by X-rays and synchrotron radiation

SAMPLE	Definition	Composition (wt%)	Lattice parameter (nm)	Dimensions (mm^3)
A	Palladium alloy substrate	Pd = 75.5%, Ag = 8.1%, Sn = 11.6%, Ga = 3.0%,Ru <1%	FCC a = 0.395	70 × 20 × 1.8
	Leucite coating	$KAlSi_2O_6$, potassium aluminium silicate	Tetragonal a = b = 1.309 c = 1.375	70 × 20 ×1.9
B	Palladium alloy substrate	Pd = 75.5%, Ag = 8.1%, Sn = 11.6%, Ga = 3.0%, Ru<1%	FCC a = 0.395	70 × 20 × 2.3

Table I: Description of the sample

RESUME

The utility of dental porcelain, as a restorative, can be extended in the PFM technique, as a strengthening mechanism for porcelain**.** Several layers of dental porcelain are fused to a metal casting. The coefficient of thermal expansion of these porcelains must be suitably matched with that of the alloy and the melting range of the alloy must be raised sufficiently above the fusion temperature of the porcelain for a successful operation.

This study deals with the evaluation of the mechanical behaviour at the interface of a glassy-ceramic coated onto palladium alloy substrate. Microstructural characterisations and residual stresses evaluations are carried out in the different layers of the sample. Residual stress measurements have been realised by neutron diffraction and high-energy synchrotron radiation to characterise the mechanical state of the sample.

The mechanical properties of metallic layers greatly depend on the residual stresses induced by the manufacturing of the coating. It is therefore very important to characterise these stresses. Some general aspects of the evaluation of residual stress are reported. A micro-mechanical model used in the study and a quick theoretical calculus are also presented.

Diffraction measurements have been performed in different zones in the sample, in particular, neutron diffraction to analyse both the glassy ceramic surface and the bulk of the leucite and of the palladium alloy; high energy synchrotron radiation for the metal/ceramic interfaces. In this way, they have allowed to obtain the best information in different regions of the analysed sample. For these experimental techniques, measurements carried out at the interface between two different materials are difficult to analyse due to great parasitic peak shifts which are obtained in such condition.

Therefore, it is important to correct the parasitic peak shifts which appear in these cases and which are not linked to the stress state of the scanned volume. This effect can be much greater than the peak shifts induced by the stresses. To solve this problem a complete modelling of 2-axis spectrometers, based on Monte Carlo calculations, has been developed either for neutrons or for synchrotron radiation. It allows also to optimise the experimental conditions and to define precisely the true volume of the neutron gauge.

The microstructure of a leucite dental glass-ceramic and of the palladium alloy substrate were finally investigated using X-ray diffraction (XRD), scanning electron microscopy (SEM) and energy dispersive spectrometry (EDS). The Transmission Electron Microscope technique (TEM) was also employed to study the structural properties of both materials.

RESUME

L'importance des porcelaines dentaires (pour les méthodes de reconstruction) est liée à l'utilisation de la technique de la Porcelaine Fondue sur Métal (PFM) pour améliorer la résistance des dépôts de céramique. Plusieurs couches de porcelaine sont déposées sur un métal élaboré par moulage. Le coefficient de dilatation thermique de ces porcelaines doit être le plus proche possible de celui de l'alliage. La température de fusion de l 'alliage doit, de plus, être supérieure à celle de la céramique pour réussir l'opération.

Cette étude porte sur l'évaluation du comportement mécanique à l'interface d'une céramique déposée sur un substrat d'alliage de palladium. Une caractérisation microstructurale et l'évaluation des contraintes résiduelles ont été menées sur différentes couches de l'échantillon. Des évaluations de contraintes ont été réalisées par diffraction neutronique et par rayonnement synchrotron à haute énergie pour caractériser l'état mécanique de l'échantillon. En effet, les propriétés mécaniques des couches métalliques dépendent grandement des contraintes résiduelles induites par l'application du revêtement. Il est alors essentiel de caractériser ces contraintes. Nous présentons ici les aspects généraux de l'évaluation des contraintes résiduelles, un modèle micro-mécanique appliqué dans notre étude et un bref calcul théorique.

Des mesures par diffraction ont été réalisées dans différentes zones de l'échantillon. En particulier, nous avons employé la diffraction neutronique pour analyser la surface et l'épaisseur de la céramique vitreuse et le cœur du substrat métallique, et le rayonnement synchrotron à haute énergie pour étudier l'interface céramique - métal. De cette façon, nous avons obtenu les meilleures informations sur les différentes régions de l'échantillon analysé.

Pour ces techniques expérimentales, les mesures conduites aux interfaces entre deux différents matériaux sont très difficiles à analyser à cause des déplacements parasites importants du pic de diffraction qui existent dans ces conditions. Ces déplacements ne sont pas liés à l'état de contraintes du volume balayé et peuvent être plus importants que les effets induits par les contraintes. Nous avons développé, pour résoudre ce problème, une modélisation complète des spectromètres 2-axes, basée sur une simulation de type Monte Carlo. Cette modélisation est effectuée à la fois pour les spectromètres de neutrons, et pour les installations utilisant le rayonnement de synchrotron. Elle permet d'optimiser les conditions expérimentales et de définir précisément la taille et la position du volume sonde.

La microstructure de la céramique dentaire et de l'alliage de palladium a été enfin étudiée en utilisant la diffraction des rayons X (DXR), la Microscopie Electronique à Balayage (MEB) et la Spectrométrie à Dispersion d'Energie (EDS). La Microscopie Electronique à Transmission (TEM) à été aussi employée pour étudier les propriétés structurales des matériaux.